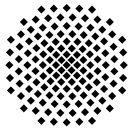

University of Stuttgart
Germany

Institute of
Robust Power
Semiconductor Systems

Master's Thesis

Design of an E-band radar frontend for a novel, self-mixing radar principle

Sven Ebeling

Supervisor: M.Sc. Janis Wörmann
Prof. Dr.-Ing. Ingmar Kallfass

Period: 06.04.2021 – 06.10.2021

Stuttgart, 06.10.2021

Postal address: Institut für Robuste Leistungshalbleitersysteme
Pfaffenwaldring 47

D-70569 Stuttgart

Tel.: +49 (0) 711 685 68700
Fax.: +49 (0) 711 685 58700
E-Mail: sekretariat@ilh.uni-stuttgart.de
Web: www.ilh.uni-stuttgart.de

Declaration

I hereby declare that this thesis is my own work and effort and follows the regulations related to good scientific practice of the University of Stuttgart in its latest form. All sources cited or quoted are indicated and acknowledged by means of a comprehensive list of references.

Stuttgart, 06.10.2021

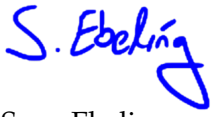

Sven Ebeling

Executive Abstract

This thesis deals with the design of a frontend to demonstrate a novel self-mixing radio detection and ranging (radar) method as part of the MIRADOR research project of ILH. In contrast to conventional principles where there is a common time or frequency basis between the transmitter and receiver, in self-mixing radar these two are electrically independent of each other. Instead, the determination of distance is based on the reflection of two or more objects and is thus a relative quantity. The necessary mixer in the receiver differs in the respect that at least one RF as well as the "LO" are supplied at one port, both of which originate from at least two spatially separated reflection objects, which is why the mixer is not a three-port in the proper sense. The components used were a frequency multiplier, two amplifiers and a mixer, each from the ELiPSe project, which were also designed at the ILH for a communication system. The frontend consists of a PCB with Rogers 3003 substrate on which not only the MMICs were placed and bonded, but also two on-PCB horn antennas were sited.

The transmitter consists of a frequency multiplier-by-eight, which produces an output power of 8.8 dBm for an input signal of −7 dBm. Via a direct chip-to-chip bond connection, the its output signal is fed to an amplifier, which increases the signal with a gain of 14.1 dB. The frequency range of the X8 extends from 70 GHz to 86.7 GHz and is not limited by the wideband amplifier. Another 17.5 µm bond wire connects the output of the amplifier to the feed structure, which excites a wave in the substrate-integrated waveguide and transmits it via a subsequent on-PCB horn antenna. On the receiver side there is an identical horn antenna. Following this, the input signals are amplified by an amplifier which has a simulated small-signal gain of 24.4 dB and a bandwidth of 60 GHz to 90 GHz. The saturated output power is 22 dBm. A MMIC formerly designed as a resistive mixer is biased as a transconductance mixer, which not only allows LO and RF to be applied at one input, the gate, but also minimizes the conversion loss to −12.8 dB. Its linear range extends up to a "LO" input power of −2.5 dBm, with the frequency range going from 66.5 GHz to 76.5 GHz. The realization of the circuit on a high-frequency printed circuit board follows the theoretical consideration and shows promising results during commissioning.

Zusammenfassung

Die vorliegende Arbeit beschäftigt sich mit dem Aufbau eines Frontends zur Demonstration eines neuartigen, selbst-mischenden Radarverfahrens im Rahmen des Forschungsprojekts MIRADOR des ILH. Im Gegensatz zu üblichen Prinzipien, bei denen es eine gemeinsame Zeit- oder Frequenzbasis zwischen Sender und Empfänger gibt, sind beim selbstmischenden Radar beide elektrisch unabhängig voneinander. Stattdessen beruht die Bestimmung der Distanz auf der Reflexion von zwei oder mehr Objekten und ist damit eine relative Größe. Der notwendige Mischer im Empfänger unterscheidet sich in der Hinsicht, dass an einem Port sowohl mindestens ein RF als auch das LO zugeführt wird, welche beide von mindestens zwei räumlich getrennten Reflexionsobjekten stammen, weshalb der Mischer kein Dreitor im eigentlichen Sinne mehr ist. Als Komponenten wurden ein Frequenzmultiplizier, zwei Verstärker und ein Mischer, jeweils aus dem Projekt ELiPSe verwendet, welche ebenso am ILH für ein Kommunikationssystem entworfen wurden. Das Frontend besteht aus einem PCB mit Rogers 3003 Substrat auf welchem nicht nur die MMICs platziert und gebondet wurden, sondern auch zwei on-PCB-Hornantennen platziert sind.

Der Sender besteht aus einem Frequenz-Verachtfacher, der bei einem Eingangssignal mit $-7\,\mathrm{dBm}$ eine Ausgangsleistung von $8{,}8\,\mathrm{dBm}$ erzeugt. Über eine direkte Chip-to-Chip-Bond-Verbindung wird sein Ausgangssignal zu einem Verstärker geleitet, der das Signal um $14{,}1\,\mathrm{dB}$ verstärkt. Der Frequenzbereich des X8 reicht von $70\,\mathrm{GHz}$ bis $86{,}7\,\mathrm{GHz}$ und ist nicht durch den Breitbandverstärker begrenzt. Ein weiterer Bonddraht mit $17{,}5\,\mu\mathrm{m}$ Durchmesser verbindet den Ausgang des Verstärkers mit der Speisestruktur, die eine Welle im substratintegrierten Wellenleiter anregt und diese über eine, in der Leiterplatte integrierte, Hornantenne aussendet. Auf der Empfängerseite befindet sich eine identische Hornantenne. Anschließend werden die Eingangssignale durch einen Verstärker verstärkt, der eine simulierte Kleinsignalverstärkung von $24{,}2\,\mathrm{dB}$ hat und eine Bandbreite von $60\,\mathrm{GHz}$ bis $90\,\mathrm{GHz}$ aufweist. Die Sättigungs-Ausgangsleistung beträgt $22\,\mathrm{dBm}$. Ein als resistiver Mischer konzipierter MMIC wird als Transkonduktanzmischer betrieben, wodurch nicht nur LO und RF an einem Eingang, dem Gate, angelegt werden können, sondern auch der Wandlungsgewinn auf $-12{,}8\,\mathrm{dB}$ erhöht wird. Sein linearer Bereich reicht bis zu einer "LO"-Eingangsleistung von $-2{,}5\,\mathrm{dBm}$, wobei der Frequenzbereich von $66{,}5\,\mathrm{GHz}$ bis $76{,}5\,\mathrm{GHz}$ reicht. Die Realisierung der Schaltung auf einer Hochfrequenz-Leiterplatte folgt auf die theoretischen Überlegungen und zeigt bei der Inbetriebnahme vielversprechende Ergebnisse.

Contents

List of Abbreviations

ADC	analog-to-digital converter
ADS	Advanced Design System
BaTiO3	barium titanate
BiCMOS	bipolar CMOS
CG	conversion gain
CMOS	complementary metal-oxide-semiconductor
CPW	coplanar waveguide
CS	common source
CST	CST Studio Suite
CW	continuous wave
DC	direct current
EIRP	effective isotropic radiated power
ELiPSe	E-Band link platform and test for satellite communication
ENIG	electroless nickel/immersion gold
EPIG	electroless palladium/immersion gold
ESD	electrostatic discharge
FFT	fast Fourier transform
FMCW	frequency modulated continuous wave
FSPL	free-space path loss
GaAs	gallium arsenide
GCPW	grounded coplanar waveguide
HB	harmonic balance
HEMT	high electron mobility transistor
IC	integrated circuit
IF	intermediate frequency
ILH	Institute of Robust Power Semiconductor Systems
InGaAs	indium gallium arsenide
LO	local oscillator
mHEMT	metamorphic HEMT
MIRADOR	self-mixing millimeter-wave radar based on multiple surface reflections
MMIC	monolithic microwave integrated circuit
Ni	nickel
PCB	printed circuit board
PEC	perfect electric conductor
PLL	phase-locked loop
PTFE	polytetrafluoroethylene
radar	radio detection and ranging
Rx	receiver
RCS	radar cross section
RF	radio frequency
S-parameter	scattering parameter

SiGe	silicon–germanium
SIW	substrate-integrated waveguide
SMD	surface-mounted device
SMU	source measure unit
SNR	signal-to-noise ratio
TE	transverse electric
TM	transverse magnetic
TVS	transient voltage suppressor
Tx	transmitter
via	vertical interconnect access

List of Figures

List of Tables

List of Symbols

Latin symbols

A_{Rx}	effective antenna aperture of the Rx antenna	dB(m^2)
A_{v}	voltage gain	1
a	wall-to-wall distance of a rectangular waveguide	m
a_{horn}	width of the horn antenna	m
a_{SIW}	via-via-distance of an SIWs	m
a_{TE10}	effective via-via-distance of a SIWs with TE10	m
a_{TE20}	effective via-via-distance of a SIWs with TE20	m
B	bandwidth	Hz
b	height of a rectangular waveguide	m
C	capacitance	F
C_{G}	conversion gain	dB
c	speed of light in a medium	m/s
c_0	speed of light in vacuum $\approx 3 \cdot 10^8\,\mathrm{m/s}$	m/s
D	directivity	dBi
d	distance between the first and second reflecting object	m
d_{via}	via diameter	m
d_{w}	bond wire diameter	m
$\vec{E}$	electric field vector	V/m
E_{i0}	electrical field amplitude	V/m
$EIRP$	equivalent isotropically radiated power	dBm
F	noise factor	1
$FSPL$	free-space path loss	dB
f	frequency	Hz
$f_{\Delta\mathrm{R}}$	frequency difference due to two objects spaced by Δr	Hz
f_0	fundamental frequency	Hz
f_{c}	cut-off frequency	Hz
f_{d}	Doppler frequency	Hz
f_{IF}	frequency of the IF signal	Hz
f_{in}	frequency of the input signal	Hz
f_{LO}	frequency of the LO signal	Hz
f_{res}	resonant frequency	Hz
f_{RF}	frequency of the RF signal	Hz

f_{source}	frequency at the moving object	Hz
G	power gain	dB
G_C	conversion gain	dB
G_{Rx}	gain of the receiving antenna	dB
G_{Tx}	gain of the transmitting antenna	dB
h	substrate height	m
ICP	input referred 1 dB compression point	dBm
$IIP3$	input referred third-order intercept point	dBm
k	propagation constant	rad/m
k_B	Boltzmann-Konstante, $k_B \approx 8.617 \cdot 10^{-5}$ eV/K	eV/K
L	inductance	H
L	length of the resonator	m
L_{eq}	equivalent length of the resonator	m
L_{total}	total losses	1
l	length of a trnsmission line	m
MDS	minimum detectable signal	dBm
N	number of chirps	1
NF	noise figure	dB
n	multiplication factor of the frequency multiplier	1
OCP	output referred compression 1 dB point	dBm
$OIP3$	output referred third-order intercept point	dBm
P	power of an arbitrary signal	dBm
$\vec{P}$	polarization	As/m^2
P_{in}	input power	dBm
P_{LO}	LO power	dBm
P_{out}	output power	dBm
$P_{r,min}$	minimum required power at receiver	dBm
P_{RF}	RF power	dBm
P_{target}	power at the target	dBm
P_{Tx}	transmitted power	dBm
p	via-via-distance of an SIWs	m
R	distance to the first reflecting object	m
R	resistance	Ω
S	slope of the chirp	Hz/s
SF	split factor of a power splitter	dB
$S_{i,j}$	scattering parameter	1
SNR_{min}	minimum required signal-to-noise ratio	1
S_{Rx}	power density at receiving place	W/(m)^2
S_{Tx}	power density of the transmitted signal	W/(m)^2
s	distance of a signal travelled	m

s_{horn}	distance between horn antenna and resonator	m
T_{chirp}	chirp duration	s
T	transmission coefficient	1
T	temperatur	K
T_{window}	observation time	s
V_{ds}	drain source voltage	V
V_{gs}	gate source voltage	V
V_{max}	maximum detectable velocity	m/s
Z_{C}	impedance of a capacitor	Ω
Z_{i}	characteristic impedance of a material i	Ω
Z_{L}	impedance of an inductor	Ω
Z_{line}	line impedance	Ω
Z_{load}	load impedance	Ω

Greek symbols

α	damping constanct	Np/m
β	phase constant	rad/m
Γ	reflection coefficient	1
Δd	distance difference	m
Δf_{BB}	bandwidth of the baseband signal	Hz
Δf_{BP}	bandwidth of the passband signal	Hz
Δf_{chirp}	bandwidth of the chirp	Hz
Δt_{2R}	propagation time for distance $2R$	s
ΔV	velocity resolution	m/s
Δx	deviation in x direction	m
Δy	deviation in y direction	m
ϵ_0	vacuum permittivity $\approx 8.854 \cdot 10^{-12}$ As/(Vm)	As/(Vm)
ϵ_{eff}	effective permittivity	1
ϵ_{r}	relative permittivity	1
η	efficiency	1
λ	wavelength	m
λ_{g}	guided wavelength	m
μ_0	magnetic constant $\approx 4\pi \cdot 10^{-7}$N/A^2	N/A^2
μ_{r}	relative permeability	1
ρ	length of the horn antenna	m
σ	conductivity	Sm
σ	radar cross section	m^2
θ	vertical angle	°
ϕ	horizontal angle	°
ω	angular frequency	1/s

1 Introduction

In today's world, radar systems are indispensable. Partly obvious, as on ships or at airports, or hidden, as behind the bumper of a car or in motion detectors, they enable the detection of objects. The origin of radar dates back more than a hundred years. In 1904, the German physicist Christian Hülsmeyer applied for a patent for his "Telemobiloskop". In it, he described a process that uses the reflection of electrical waves from metallic objects to detect them. As in today's monostatic system, a transmitter emitted a wave which, after reflection, influenced the sensitive receiver located at the same place. However, he was ahead of his time and the range to detect ships, which was the application he envisioned, was less than the sight and hearing range to them. [40]

A few decades later, during World War II, the military recognized the advantages for detecting enemy aircraft, further developed the system, and used what was now called radar. It was many years before it was adopted for civilian use. Today, four frequency bands are available in Germany for road traffic applications, with the range from 76 GHz to 77 GHz being the most widely used, as this is specifically intended for the automotive sector and can be used worldwide. The radar system developed in this work also covers this range with its 13 GHz bandwidth. [59, p.260]

Implementing the system in higher frequency ranges offers numerous advantages, such as the aforementioned bandwidth, which positively affects the range resolution of the system. Also, the package size, the power consumption and, depending on the selected frequency range, the attenuation in air decreases. With increasing frequency, the directivity of antennas and thus also the gain increases, which brings further advantages. The determinability of smaller distances extends the use of radar systems to vital sign detection and material analysis. For example, organs, the alignment of material fibers, but also production and packaging defects can be detected [45, p.9]. [30, pp.3-6]

In many of the cases mentioned, not only does a reflection corresponding to the desired distance occur, but many due to various, at first glance uninteresting material transitions. The desire to protect the sensitive electronics from environmental influences and to integrate them as inconspicuously as possible requires the use of radomes and the implementation of the radar, for example, behind the body paneling of a car. For this reason, several works deal with keeping this first reflection low [34][36][61]. Another approach is to use the strong reflection to mix down the further received signals into the analyzable range. This idea is based on a patent submitted by members of the Institute of Robust Power Semiconductor Systems (ILH) of the University of Stuttgart [45]. Due to this industrial property right, no comparable systems and resulting measurements are available, which is why common frequency modulated continuous wave (FMCW) radar systems in the same frequency range will be considered instead. As already mentioned, these are often radar systems

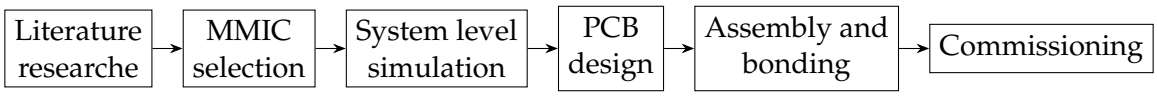

Figure 1.1: The flow chart shows the design procedure of the master's thesis.

developed for the automotive sector. The frequency range covers a part of the E-band from 60 GHz to 90 GHz.

In the automotive sector, range resolution plays only a secondary role for most radar systems as they are currently used for long and medium distances. With a maximum bandwidth of 700 MHz and thus a range resolution of 0.21 m, it is sufficient to detect road users and other obstacles. An angular resolution of up to 0.1° allows to determine dimensions of them. A high transmission power of 34 dBm (effective isotropic radiated power (EIRP)), which is necessary to allow measurement over long distances up to 250 m and thus to be able to warn the driver and intervene at an early stage, is of primary importance. [59, pp.300-315]

In addition to these sensors, there are single chip solutions, which are sold by Texas Instruments, for example. The *IWR1443* covers a frequency range from 76 GHz to 81 GHz and thus has a continuous bandwidth of 4 GHz [17]. The power of the transmitter (Tx) is 12 dBm, to which an antenna must be connected. Also integrated circuits (ICs) with built-in antenna are offered, which have a transmit power of 16 dBm (EIRP) with the same characteristics as above [3].

Irrespective of the two fields of application and the associated regulations, there is a large body of scientific work that also investigates integrated radar systems. Since a high bandwidth is desired, two publications are mentioned at this point. On the one hand, a dual-receiver FMCW SiGe radar system fabricated in BiCMOS, which has a bandwidth of 26 GHz in the range of 83 GHz to 109 GHz and an output power of 14.8 dBm, and on the other hand a system fabricated in an InGaAs mHEMT technology [58]. This monolithic microwave integrated circuit (MMIC) includes a frequency multiplier by six, a variable gain amplifier, and on the receiver (Rx) side a low-noise amplifier and a quadrature mixer. At the input of the Tx, a 15.6 GHz signal with at least 4 dBm power is expected. The maximum output power is 8 dBm. The total bandwidth of the system is 16 GHz. [63]

The structure of the work is based on the individual steps performed, as shown in the flow chart in Fig. 1.1. The theoretical basics are clarified in chapter 2. Thereby, different radar principles and especially the distinction and similarities with the self-mixing radar principle to be designed are discussed. In addition, the origin of reflections of waves from objects is explained. The following chapter deals with the selection of the individual components for the radar system. In particular, the self-mixing mixer is addressed. Furthermore, not only the MMICs are discussed, but also the structure of the used antennas is described. Before the chapter concludes with the simulation results of the overall system, the modeling of the wave propagation is presented. Chapter 4 is dedicated to the realization of the RF PCBs. In addition, commissioning and initial verification measurements will be covered. The last chapter draws the conclusion and provides an outlook.

2 Basics

Before going into the design of the radar system, their main fundamentals will be discussed. For this purpose, the first subchapter deals with the basic principle of a radar. In addition, the FMCW radar is differentiated from other radar principles. Another subchapter is dedicated to the self-mixing radar principle and wave propagation.

2.1 Fundamental radar principle and radar types

The acronym radar stands for radio detection and ranging and describes a system which, from the reception of radio waves, attempts, depending on the system, to detect the distance, speed, solid angle of movement and from this the position and/or contour of the object. There are different types of radars on the market, which are explained in a rudimentary way only to differentiate them from the implemented self-mixing radar.

Perhaps the most intuitive radar is the monostatic pulse radar. Here, monostatic describes that the transmitter and receiver are in one place. The term for separate locations would be bistatic. In pulse radar, according to the name, a single powerful pulse is transmitted, reflected at the object, received again and thus propagation time Δt_{2R} of this distance is determined. Since the travelled distance s is the product of the propagation velocity in the medium c and the elapsed time, $s = 2R = c\Delta t_{2R}$ is valid where R is the distance between the antenna and the object and for example air has a propagation velocity of $c \approx c_0 = 3 \cdot 10^8\,\mathrm{m/s}$. When the reflecting object moves, there is a frequency shift called Doppler shift. The difference frequency is formed from the received and transmitted signal, which is related to the velocity difference of the object. It must be noted that the pulse is first received again before a new one is sent out, otherwise errors can occur e.g. in the distance determination. [60]

Another type of radar is the continuous wave (CW) radar, which emits a continuous electromagnetic wave. This eliminates more or less the possibility of a distance measurement, since neither the amplitude nor the frequency can be used to draw conclusions about the time of transmission. Only in a small range the phase difference can be evaluated unambiguously, so that distance changes in the range of half a wavelength can be measured. The CW radar, unlike pulse radar, requires a second antenna because it transmits and receives continuously. Since the transmit frequency for stationary targets corresponds to the receive frequency, care must be taken to decouple the transmitter and receiver, otherwise they may appear directly as ghost targets. There are two obvious possibilities: the spatial separation of the two antennas, where already the placement of

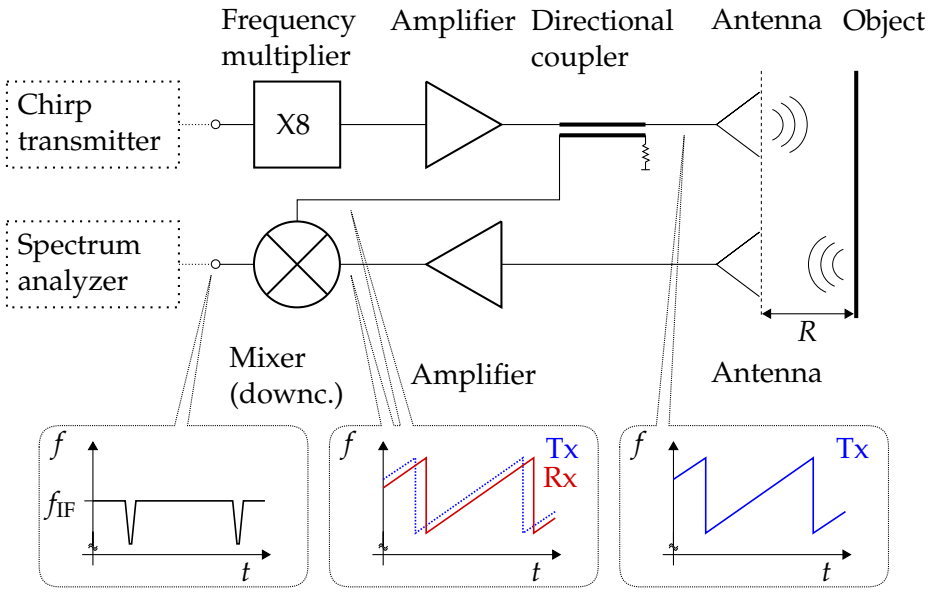

Figure 2.1: Schematic representation of the frequency modulated continuous wave (FMCW) radar.

the transmitting antenna in front of the receiving antenna can be sufficient, and the frequency separation. The second suggestion can only be used for moving objects, because the movement of the reflecting object causes a frequency shift, as described above. Now the transmitting and receiving antennas can have different frequency ranges. By mixing the received signal with a part of the transmitted signal, an intermediate frequency can be determined, which is related to the velocity difference of the object. Accordingly, various application possibilities result from the above description. On the one hand, the pure motion detection or the combination with the evaluation of the speed, as it is applied in traffic monitoring. Or on the other hand, the monitoring of small movements, such as in medicine that of organs. It is obvious to add a variable component to the CW signal to provide a range measurement that significantly exceeds that of the CW radar. Typically, the frequency change is used here, resulting in the FMCW radar. [60]

2.2 Frequency modulated continuous wave radar

The FMCW radar uses a frequency modulated CW signal, which is called chirp. The idea behind it is that modulation adds a kind of identification to the signal so that measurement of the propagation time becomes possible. While mainly frequency modulation is used, amplitude or phase modulation is also possible. The system consists of a chirp generator, the RF frontend with Tx and Rx, and a signal acquisition and processing unit. It is shown in Fig. 2.1. For the description and comparison of such a system there are different parameters, which find varying weighting depending on the place of use. The most obvious values are on the one hand, the maximum distance with which an object of a certain size can be detected (also depending on the application) and, on the other hand, the measurement resolution. The latter can be related to the various physical quantities, such as distance, speed or angle. In real-world applications unwanted multiple reflections, interference,

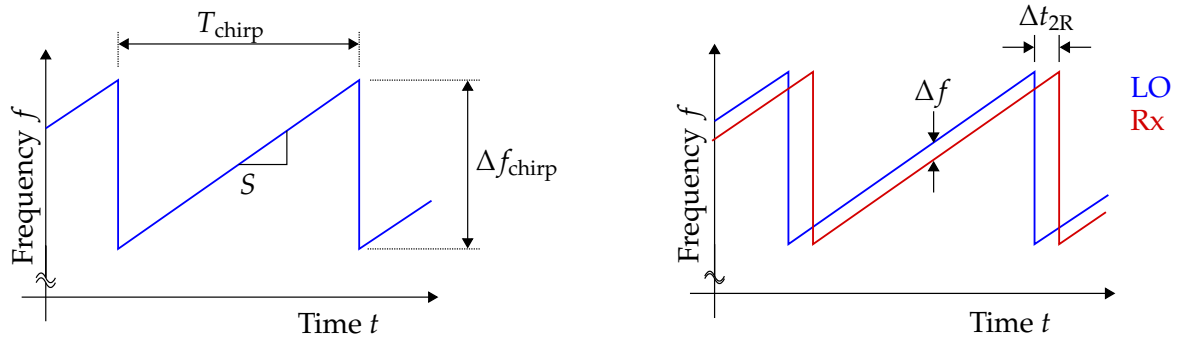

(a) Chirp signal

(b) Received signals

Figure 2.2: The transmitted chirp signal is shown in a). The time-frequency dependencies for two input signals at the mixer are plotted in b).

and jammer signals occur, which can greatly affect the radar. The system must be robust in this respect. General reliability and maintainability also play a role. [59, pp.275-277]

Various signal shapes can be used as a chirp signal. A common one is the triangular shape and the saw tooth shown in Fig. 2.2. However, the use of a linear frequency rise or fall simplifies the subsequent signal processing. The slope, i.e. the frequency change per time, is denoted as S. The bandwidth as Δf_{chirp} and the period as T_{chirp}. The signal must be sufficiently long so that both local oscillator (LO) and RF components are available for downmixing. In general, the chirp sequence repeats periodically. It must also be taken into account that the shorter T_{chirp} is selected, the less time remains for the evaluation, since the assignment must be unique for this. The transmitted signal arrives at the receiver after a certain time $T_{2R} = 2R/c$, as shown in the same figure. Typically, $\Delta t_{2R} \ll T_{chirp}$ holds. As explained for the pulse radar, the distance can be determined from this time offset. The corresponding formula can be derived from the calculation of the expected differential frequency

$$f_{IF} = S\Delta t_{2R} = \frac{\Delta f_{chirp}}{T_{chirp}} \frac{2R}{c}. \tag{2.1}$$

This results from the slope multiplied by the round trip time. A linear frequency ramp is necessary for this. It is obvious that the formula for the distance

$$R = \frac{f_{IF}}{\Delta f_{chirp}} \frac{T_{chirp} c}{2} \tag{2.2}$$

can be obtained by transforming equation 2.1. Accordingly, the duration of the frequency rise determines the maximum possible measuring range from a time point of view. [52, pp.7-12]

To determine the maximum detectable distance from a power-based point of view, the radar equation

$$R_{max} = \sqrt[4]{\frac{P_{Tx} G_{Tx} G_{Rx} \lambda^2 \sigma}{(4\pi)^3 P_{r,min}}} \tag{2.3}$$

is used. The derivation assumes a monostatic system, where the distance to the object is denoted as R. For a non-istropic radiating Tx antenna,

$$S_{\mathrm{Tx}} = P_{\mathrm{Tx}} \frac{G_{\mathrm{Tx}}}{4\pi(\Delta d)^2} \tag{2.4}$$

applies to the directional power density in mainlobe direction. Here P_{Tx} describes the supplied power and $\Delta d = R$ the distance at which the power is measured. Since the object is not a point but a surface, $P_{\mathrm{target}} = S_{\mathrm{Tx}}\sigma$ applies, where σ represents the effective area of the object, that is also called the RCS. The reflecting object and its property to reflect waves are described by this value. Decisive for this are the permittivity, permeability and conductivity [27, p.2]. More on this topic can be found in subchapter 3.6.2. Similarly, the equation assumes that the object radiates not only in one direction, but isotropically in all directions. The object is thus a kind of antenna, for which again the above equation 2.4 can be used. Also the receiver antenna has an effective area A_{Rx}, so the received power is

$$P_{\mathrm{Rx}} = S_{\mathrm{Rx}} \cdot A_{\mathrm{Rx}}\,, \tag{2.5}$$

with the power density

$$S_{\mathrm{Rx}} = P_{\mathrm{target}} \frac{1}{4\pi R^2} = S_{\mathrm{Tx}}\sigma \frac{1}{4\pi R^2} = P_{\mathrm{Tx}} \frac{G_{\mathrm{Tx}}}{4\pi R^2} \frac{\sigma}{4\pi R^2} \tag{2.6}$$

at the Rx antenna. The equation 2.5 requires knowledge about the effective antenna area of the receiving antenna. As an alternative, this value can be calculated from the antenna gain

$$A_{\mathrm{Rx}} = \frac{G_{\mathrm{Rx}}\lambda^2}{4\pi} \tag{2.7}$$

if the antenna is lossless. This ratio is independent of the antenna shape. [27, p.171]

All in all, by substituting the equations 2.6 and 2.7 in 2.5, the power at the receiver can thus be determined by

$$\begin{aligned} P_{\mathrm{Rx}} &= S_{\mathrm{Rx}} A_{\mathrm{Rx}} \\ &= P_{\mathrm{Tx}} \frac{G_{\mathrm{Tx}}}{4\pi R^2} \frac{\sigma}{4\pi R^2} \frac{G_{\mathrm{Rx}}\lambda^2}{4\pi} \\ &= P_{\mathrm{Tx}} \frac{G_{\mathrm{Tx}} G_{\mathrm{Rx}} \lambda^2 \sigma}{(4\pi)^3 R^4}\,. \end{aligned} \tag{2.8}$$

Transforming the equation and inserting the minimum power necessary to detect a signal $P_{\mathrm{r,min}}$ yields the equation according to 2.3. The equation can be simplified to

$$R = \sqrt[4]{\frac{P_{\mathrm{Tx}} G^2 \lambda^2 \sigma}{(4\pi)^3 P_{\mathrm{r,min}}}} \tag{2.9}$$

if the two antennas used are identical and thus have the same gain $G = G_{\mathrm{Tx}} = G_{\mathrm{Rx}}$. This is the case

in the designed system.

The minimum power

$$P_{\mathrm{r,min}} = -174\,\mathrm{dBm} + NF + 10 \cdot \log(B) + SNR_{\mathrm{min}} \tag{2.10}$$

can be calculated from the noise figure of the receiver NF, the bandwidth of its B and the minimum signal-to-noise ratio (SNR) necessary to evaluate the received signal (defined by analog-to-digital converter (ADC)) SNR_{min}. [29, p.14]

The range resolution of a radar

$$\Delta R = \frac{c}{2\Delta f_{\mathrm{chirp}}} \tag{2.11}$$

describes the distance two objects must have from each other to be distinguished. For the calculation only the bandwidth of the chirp signal $\Delta f_{\mathrm{chirp}}$ and the propagation speed c are necessary. The equation results from simple signal processing considerations. The evaluation takes place in the frequency domain. For this purpose, for example, a sinusoidal signal is considered in the time domain over a certain duration and transformed into the frequency domain by means of a Fourier transformation. The result is ideally a single peak at the corresponding frequency. The minimum detectable frequency is given by the time duration, whereby only frequencies can be represented which have a period time below the duration of the time window $T_{\mathrm{window}} > 1/\Delta f$. If one wants to distinguish between two signals from two reflecting objects, then the frequency difference is $\Delta f_{\Delta \mathrm{R}}$. The frequency shift is a result due to the limited propagation speed c of the wave. The distance between the two objects through which the frequency difference arises is ΔR. This allows to determine the frequency difference to $\Delta f_{\Delta \mathrm{R}} = St_{\Delta \mathrm{R}} = \Delta f_{\mathrm{chirp}} 2\Delta R/(T_{\mathrm{chirp}} c)$. The minimum spacing between both objects is therefore $\Delta R = T_{\mathrm{chirp}} c/(2\Delta f_{\mathrm{chirp}} T_{\mathrm{window}})$. Consequently, the longer T_{window}, the more frequencies are passed through, corresponding to a larger bandwidth $\Delta f_{\Delta \mathrm{R}}$. Since the maximum observation time is equal to the duration of the chirp $T_{\mathrm{window}} = T_{\mathrm{chirp}}$, the equation of the range resolution 2.11 is obtained. The longer the fast Fourier transform can be applied, the more accurate the result. High bandwidth is achieved primarily by using higher frequencies. These also make it possible to reduce the geometric dimensions of a radar system, especially the antenna. [52, pp.7-12]

There are two ways to determine the speed of the reflecting object. The best known is the calculation based on the Doppler shift that occurs when the object moves in relation to the radar system. For a constant velocity difference, this results in a frequency shift $f_{\mathrm{d}} = (1 + \Delta v/c) f_{\mathrm{source}}$ as shown in Fig. 2.3, where f_{source} is the frequency directly at the moving object. From this, the relative velocity Δv can be calculated. The red dashed line shows the course of the Rx signal without frequency difference. A movement towards the radar system results in a frequency shift by a positive value and thus it is shifted upwards compared to the transmitted signal as shown in Fig. 2.3. [29, p.13]

But now it is necessary to distinguish between a frequency shift due to the time of flight and due to the velocity difference. This is facilitated by using a triangular chirp signal instead of a sawtooth one. The absolute velocity can be calculated by $f_{\mathrm{d}} = (f_2 - f_1)/2 = 2 f_{\mathrm{center}} \Delta v/c$.

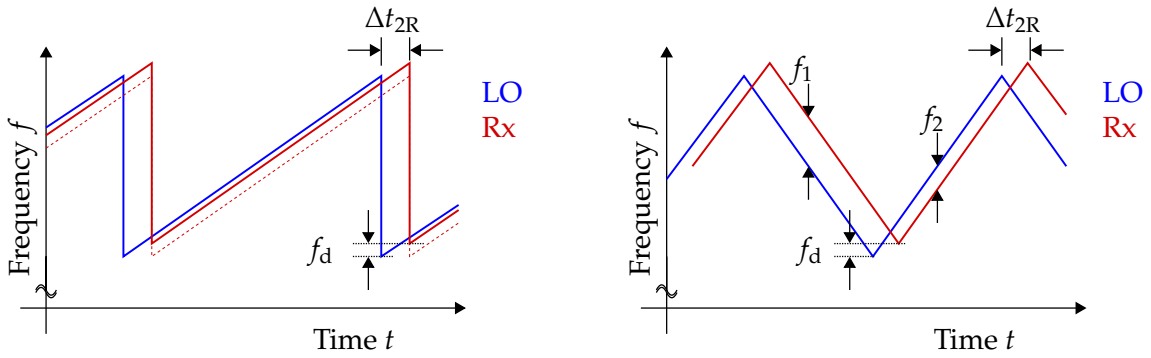

(a) Saw tooth chirp

(b) Triangular chirp

Figure 2.3: The time-frequency dependencies for two input signals at the mixer are shown for the case of a velocity difference. In a) a saw tooth chirp is used while in b) the shape changed to a triangular one.

In addition, the maximum detectable velocity

$$V_{\max} = \frac{c}{4fT_{\text{chirp}}} \tag{2.12}$$

can also be determined by a radar system. The related velocity resolution

$$\Delta V = \frac{c}{2fT_{\text{chirp}}N} \tag{2.13}$$

consists of the transmission frequency f, the propagation velocity of the wave c and the time interval $T_{\text{chirp}}N$, where N stands for the number of chirps which are used for the evaluation. The use of a higher frequency range enables the improvement of the velocity resolution according to the formula shown. [29, p.17]

The easiest way to determine the angle to an object is to rotate the antennas accordingly and observe the signal strength. This is possible when the main lobe is clearly shaped. Since mechanical systems are error-prone, maintenance-intensive and mostly more complex to build, the angle can be determined via triangulation. For this purpose, the signal of one antenna is received after reflection e.g. from two antennas with known distance. The phase difference now allows the angle of incidence to be determined. Together with the distance measurement, three-dimensional structures can also be calculated by software.

2.3 Self-mixing radar principle

So far, it has always been assumed that there is only one reflection. In reality, however, two or more reflections occur very often. For example, the first reflection of a distance radar installed in a car shows up through the bumper. Compared to the car in front, the bumper is geometrically very close to the antenna, which results in a low intermediate frequency at the mixer. Due to

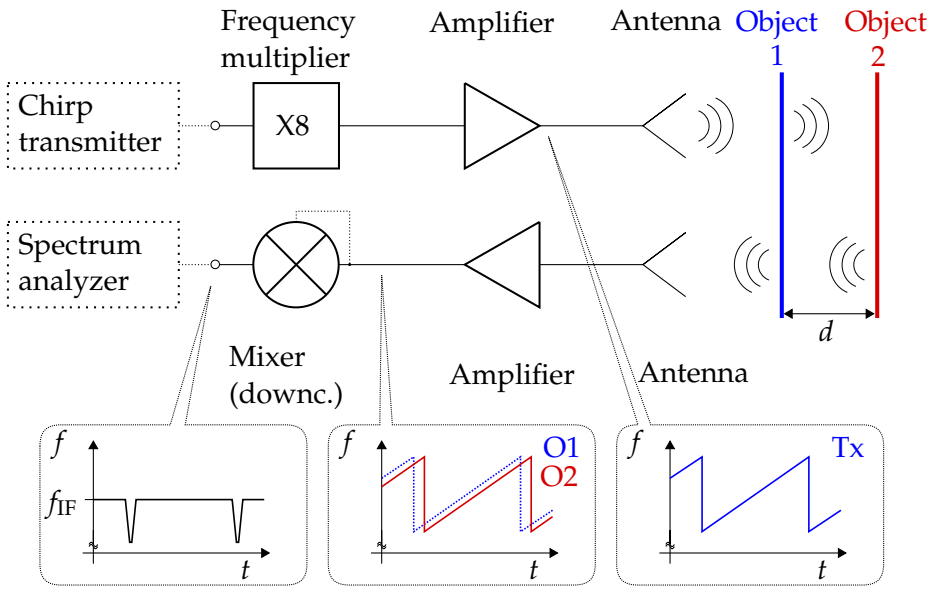

Figure 2.4: Schematic representation of the self-mixing frequency modulated continuous wave radar.

the low propagation loss, the received power can be very high. There are now three ways to deal with such situations, firstly the transmission through the bumper can be reduced. For this purpose, special materials are used and the thickness of the bumper is adjusted so that cancellation of the reflected wave occurs [34, pp.7]. This is not only more expensive but also more complex to manufacture. Second, the intermediate frequency (IF) caused by the bumper is so far away from the desired IF frequency that the corresponding signal component can be filtered out by a high-pass filter. Since the frequency of the new LO signal is close to the RF frequency and also changes over frequency, no filtering can take place infront of the receiver. However, the mixer must be designed for such strong RF powers in order not to get into compression and thus generate further frequency components. For this the LO power must be higher than the highest power of the received RF signal. The third option, which is investigated in this work, takes advantage of the strong RF signal component by using it as a new LO component. As a result, the mixer is no longer a three-port component, instead it requires only two ports (both RF&LO and IF). The system is shown in Fig. 2.4. On the transmitter side, the system is composed of the chirp generation, the frequency multiplier and an amplifier. The directional coupler, as used in the FMCW radar, can be omitted. On the receiver side, after the amplifier, there is the aforementioned mixer in a self-mixing configuration. Represented by the dashed line to the former LO port. The downmixed signal is finally evaluated. Chapter 3 describes the individual components in more detail.

It is important to note that only the relative distance d between the two reflection objects can be determined. However, in most cases this is also the relevant one. Since this is a modified version of the presented FMCW radar, associated formulas can still be used. Care should be taken, because the first reflection object now serves as the reference. This means that the relative distance and also the relative velocity between the two reflection objects must be used. However, this is again

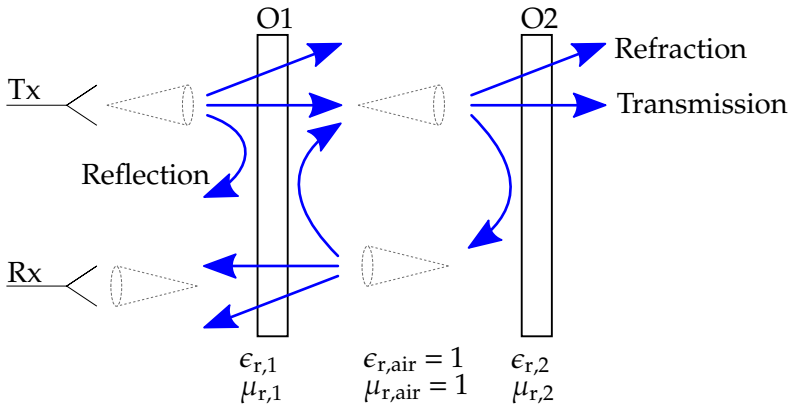

Figure 2.5: Illustration of wave propagation for two objects separated by air. Cones represent the free-space path loss (FSPL).

advantageous, since the distance to the first reflection object plays only a secondary role and can thus be neglected in most considerations, at least as long as the required power values at the receiver are reached. If the distance is known, individual properties of the intervening propagation medium can also be investigated. For example, the relative permittivity ϵ_r can be considered when checking an actually homogeneous medium for contained impurities. Thus, the radar principle enables a non-destructive investigation. [45]

2.4 Wave propagation

On the one hand, the propagation of the wave is an important, but also complex topic, which can therefore only be analyzed rudimentarily using formulas. The propagation can be described as quasi-optical. However, the effects of diffraction and refraction known from optics play only a minor role in an initial consideration and are therefore not considered in detail.

As mentioned in the example at the beginning of the subchapter 2.3, the wave is not exclusively reflected at the bumper, but also a part of it is transmitted. At a second object, for example a car driving ahead, there is another reflection of the emitted electromagnetic wave. This wave then partially propagates again through the first object, the bumper, and is finally received by the antenna. Reflections can also occur between the two objects, which then appear at a lower power due to propagation through the first object at the receiving antenna. This is shown in Fig. 2.5 and leads to ghost objects. The consideration of the wave propagation shall be limited to two reflection objects to reduce the complexity. However, the radar system to be investigated can in principle enhance more than two reflections, as long as a dominant received signal is available, which acts as LO signal and the signal processing can handle this situation.

If the characteristic impedance of a material changes, partial reflection and scattering occur. If one considers the emitted wave in the far field as a plane wave, then, for example, with propagation in

the z-direction and a electric field vector oriented along the x-axis, it can be written

$$\vec{\boldsymbol{E}}_{\mathrm{i}}(z) = \vec{a_{\mathrm{x}}} E_{\mathrm{i}0} \exp(-jkz)\,, \tag{2.14}$$

where $E_{\mathrm{i}0}$ is an arbitrary amplitude and k prepresents the propagation constant. Now, if this wave meets a material change, the energy splits at least into reflected and transmitted energy

$$\vec{\boldsymbol{E}}_{\mathrm{i}}(z) = \vec{\boldsymbol{E}}_{\mathrm{r}}(z) + \vec{\boldsymbol{E}}_{\mathrm{t}}(z)\,. \tag{2.15}$$

If we now want to determine the fraction of reflected/transmitted energy, we consider the characteristic impedance

$$Z_{\mathrm{i}} = \sqrt{\frac{\mu_{\mathrm{r},i}\mu_0}{\epsilon_{\mathrm{r},i}\epsilon_0}} \tag{2.16}$$

where μ_{r} is the relative permeability, μ_0 is the magnetic permeability of free space, ϵ_{r} is the relative permittivity and ϵ_0 is the vacuum permittivity. If $\mu_{\mathrm{r}} \approx 1$, the following applies to the reflection coefficient

$$\Gamma = \frac{E_{\mathrm{r}0}}{E_{\mathrm{i}0}} = \frac{Z_2 - Z_1}{Z_2 + Z_1} \approx \frac{\sqrt{\epsilon_{\mathrm{r},1}} - \sqrt{\epsilon_{\mathrm{r},2}}}{\sqrt{\epsilon_{\mathrm{r},1}} + \sqrt{\epsilon_{\mathrm{r},2}}} \tag{2.17}$$

and for the transmission coefficient

$$T = \frac{E_{\mathrm{t}0}}{E_{\mathrm{i}0}} = \frac{2Z_2}{Z_2 + Z_1} = \frac{2\sqrt{\epsilon_{\mathrm{r},1}}}{\sqrt{\epsilon_{\mathrm{r},1}} + \sqrt{\epsilon_{\mathrm{r},2}}}\,. \tag{2.18}$$

It holds $1 + \Gamma = T$. [34, pp.4-7][51, pp.28-33]

In addition to the effects at material transitions, there are also losses in the material during propagation. The attenuation within a medium can be determined by

$$P(z) = P_{\mathrm{Tx}} \exp(-2\alpha z)\,, \tag{2.19}$$

where z is the distance traveled and α is the real part of the propagation constant $\gamma = \alpha + \mathrm{j}\beta$. Moreover, this can also be calculated accordingly as follows

$$\gamma = \alpha + \mathrm{j}\beta = \sqrt{\mathrm{j}\omega\mu(\sigma + \mathrm{j}\omega\epsilon)} \tag{2.20}$$

where α is also known as the damping constant, β is the phase constant, ω is the frequency, σ is the conductivity, $\epsilon = \epsilon' - \mathrm{j}\epsilon''$ is the complex permittivity, and $\mu = \mu' - \mathrm{j}\mu''$ is the complex permeability. [51, pp.18,82]

Damping by air does not have to be considered in the case of the system to be designed. This frequency range was chosen deliberately and lies within an atmospheric window. Even small frequency changes lead to different absorption rates by occurring molecules in the atmosphere. This window is limited by the absorption lines of O_2 at 60 GHz (with an attenuation of 20 dB/km) and 118 GHz. At 94 GHz, in contrast, the attenuation is only (0.6 dB/km). Fog, rain, snow or dust also have an influence.[43, Ch.2, p.9]

If the atmospheric losses, together with intra-device attenuation losses and fluctuation losses on target reflection are to be included in the radar equation, then equation 2.3 can be written as

$$R_{\max} = \sqrt[4]{\frac{P_{\mathrm{Tx}} G_{\mathrm{Tx}} G_{\mathrm{Rx}} \lambda^2 \sigma}{(4\pi)^3 P_{\mathrm{r,min}} L_{\mathrm{total}}}}, \tag{2.21}$$

where L_{total} covers all losses that occur. [59, p.261]

Up to now, it was assumed in this subsection that the wave propagates as a plane wave. In reality, the wave originates from a radiating antenna. This radiation can be decomposed into two elements: An isotropically radiating antenna that radiates spherically around it and a focusing effect called directivity. Both are also covered by the radar equation, see equation 2.3. First behavior is described by the free space path loss

$$FSPL = 20 \log\left(\frac{c}{4\pi R f}\right). \tag{2.22}$$

The emitted energy of the antenna is distributed evenly in space by a so-called omnidirectional radiator. The propagation takes place as spherical areas, whereby the power density is constant within these. With increasing distance, the power density decreases, as shown by the equation 2.6. For example, if the wave travels a distance of 50 cm, the attenuation is approximately −64.5 dB at a frequency of 80 GHz. In the far field, a section of the sphere's surface can be considered as a plane wave, which is why the above equations apply. The second point, directivity of an antenna, is covered separately by the gain. The antenna gain $G = \eta D$ is composed of the efficiency of the antenna η and the directional gain D. The latter describes the ratio between the intensity $P(\phi, \vartheta)_{\max}$ in the solid angle of the strongest radiation and the value $P_{\mathrm{total}}/(4\pi)$ of a homogeneous omnidirectional radiator of the same total output power $P_{\mathrm{total}} = \int\int P(\phi, \vartheta) d\phi d\vartheta$. Where the azimuth angle in the horizontal plane is denoted by ϕ and ϑ is the vertical elevation angle. The narrower the main lobe, the larger the directional gain. The effective isotropic radiated power (EIRP) can be determined from the transmitted power and the antenna gain. Without considering additional losses, $EIRP = P_{\mathrm{Tx,dBm}} + G_{\mathrm{Tx,dB}}$ is obtained. This allows the maximum range of the radar to be determined, but is also relevant for the approval of the system as a commercial product. [51, p.674]

On the one hand, attenuation occurs over distance, through the medium and due to scattering in and at objects. In addition, there is a time shift. This also plays a fundamental role in the radar principle used: Starting from a transmitted signal with increasing frequency, the component with higher frequency first reappears at the receiver antenna. The signal component of the second reflection are only visible with a delay and thus have a lower frequency. Depending on whether the first object reflects much of the transmitted power or the second, $f_{\mathrm{LO}} > f_{\mathrm{RF}}$ or $f_{\mathrm{LO}} < f_{\mathrm{RF}}$ applies. The mixer must thus cover both cases. At the IF output of the mixer there is the signal with the downmixed frequency difference, which can be assigned to the relative distance as shown above. Depending on the application, one of the two cases occurs. In order to increase the received LO power, a layer of suitable material, which leads to greater reflection, can be applied by gluing, painting, or other methods, if necessary. However, especially in the case of the first reflection

object, care must be taken to ensure that the transmission is sufficiently large so that the second reflection can still be detected. [45, pp.16-17]

Finally, it should be mentioned that transmission through an object is not mandatory. For example, a corner reflector can be used, which sits at the edge of the main lobe and does not impair the view to the object to be detected. Due to its structure, most of the transmitted energy is returned. Likewise, a spherical object, for example made of metal, can be used as a reference, because it radiates isotropically. A metallic base, e.g. as part of a conveyor belt, can also be used as a second reflection object, although it is not completely covered by the object to be examined.

3 System-Level Simulation

This chapter deals with the selection of components for the radar frontend. First, the basic parameters of a radar system are clarified for this purpose. This is followed by the subchapters for the frequency multiplier, the amplifiers and the mixer, which analyze the individual components of the overall system on the basis of simulation results. After that, the on-PCB antennas used are explained as well as the modeling of the wave propagation and the related RCS is discussed. The chapter concludes with a discussion of the simulation results of the overall system.

3.1 Radar system

The radar system shown in Fig. 2.4 consists of a transmitter and a receiver. Various characteristic parameters are used in the individual subsections to select the components. At this point, the most important parameters of the overall system are introduced, which must also be kept in mind when selecting the individual components.

The most obvious parameter is the frequency range. This is typically specified for the transmitted and received wave in free space. Likewise, the input and output of the system must be considered. The input frequency range must be broadband enough to handle the entire frequency range of the chirp signal. The output frequency range determines the components required for signal processing and is typically in the low frequency range for this purpose. Accordingly, this value is referred as the IF bandwidth.

An equally important parameter is the transmitting power, which must not exceed certain limits for regulatory approval. However, a high transmitting power also means that targets further away or targets with a lower reflectivity can be detected better. Especially in the case of the self-mixing radar, this plays a major role, since the strongest reflection signal is used as the LO signal for the mixer and should therefore be high. The input power, which is required at least for the detection of the second reflection object, can be determined for a receiver very easily by calculation. The formula is composed of three parts. First, the thermal noise power that can be caluclated from $10\log(k_B TB)$, where k_B is the Boltzmann constant, T is the temperature, and B is the bandwidth of the receiver. It can be described as white noise, because it has the same power over the frequency range. Second, the noise figure of the receiver NF. The last component is a buffer used to clearly distinguish the signal from the noise. A typical quantity for this is 3 dB. The minimum detectable

signal power for the amplifier infront of the mixer is

$$\begin{aligned} MDS &= 10\log(k_B TB) + NF + 3\,\mathrm{dB} && (3.1)\\ &= 10\log(1.38\cdot 10^{-23}\,\mathrm{W\,s\,K^{-1}}\cdot 298\,\mathrm{K}\cdot 15\,\mathrm{GHz}) + NF + 3\,\mathrm{dB} && (3.2)\\ &= -102.1\,\mathrm{dBW} + 30\,\mathrm{dB} + NF + 3\,\mathrm{dB} && (3.3)\\ &= -69.1\,\mathrm{dBm} + NF && (3.4) \end{aligned}$$

for an assumed bandwidth of 15 GHz. [48, p.42]

In the same way, the *MDS* can be calculated for the spectrum analyzer used to evaulate the output IF signal. For a bandwidth of 10 MHz the minimum input power is

$$\begin{aligned} MDS &= 10\log(k_B TB) + NF + 3\,\mathrm{dB} && (3.5)\\ &= 10\log(1.38\cdot 10^{-23}\,\mathrm{W\,s\,K^{-1}}\cdot 298\,\mathrm{K}\cdot 10\,\mathrm{MHz}) + NF + 3\,\mathrm{dB} && (3.6)\\ &= -133.86\,\mathrm{dBW} + 30\,\mathrm{dB} + NF + 3\,\mathrm{dB} && (3.7)\\ &= -100.86\,\mathrm{dBm} + NF\,. && (3.8) \end{aligned}$$

The evaluation by an ADC also requires a certain minimum power or a minimum voltage. This is in the nature of things, since a time and value continuous signal is converted into a time and value discrete signal. The assignment is thereby made to a finite number of quantization levels. Signals can not only be below the noise floor and thus no longer detectable, but also in the case of close neighboring signals by the occurring phase noise of the chirp phase-locked loop (PLL). This effect occurs especially in the case of a high-power signal next to a low-power one, which can be masked by the phase noise of the first one. However, since signal generation is not part of this work, it will not be discussed in more detail. [29, pp.35-40]

As seen in equation 3.5, a lower noise figure means that the required input power $P_{\mathrm{r,min}}$ can also be lower. This also increases the range. When calculating the noise factor for a chain of components, the so called Friis formula can be used

$$F_{\mathrm{total}} = F_1 + \sum_{k=2}^{n} \frac{F_{\mathrm{k}} - 1}{\prod_{j=1}^{k-1} G_{\mathrm{a,j}}} = F_1 + \frac{F_2 - 1}{G_{\mathrm{a},1}} + \ldots + \frac{F_{\mathrm{n}} - 1}{G_{\mathrm{a},1} G_{\mathrm{a},2} \ldots G_{\mathrm{a,n-1}}}\,. \tag{3.9}$$

Here, the noise factor of the individual components are denoted by F_{i} and the gains of these by G_{i}. It can be seen that the first stage has the greatest influence on the overall noise behavior of the chain. Therefore, the amplifier at the input of the receiver should have a low noise figure ($NF = 10\log(F)$) and a high gain. Nevertheless, the subsequent components should not be disregarded. [29, p.25]

When dealing with the output and input power of the radar system, the consideration of the gain is crucial. Ideally, the necessary input power of the frequency multiplier is low and the transmit power is high. This corresponds to a high gain. Especially in the receiver, a high gain plays an important role to achieve the mentioned required powers. In order to calculate the total gain of each chain, the individual logarithmically scaled gains G_{i} can be added.

The gain affects not only the noise of the chain and the output power, but also the linearity of the system. Depending on

$$\frac{1}{IIP3_{\mathrm{T}}} = \frac{1}{IIP3_1} + \frac{G_1}{IIP3_2} + \frac{G_1 G_2}{IIP3_3} + ... + \frac{\prod_1^n G_{\mathrm{n-1}}}{IIP3_{\mathrm{n}}}, \tag{3.10}$$

the last component determines most the linearity of the system. The input related third order intercept $IIP3_{\mathrm{i}}$ of each component is used as a measure. If the linearity of the receiver is poor, intermodulation will occur, resulting in false targets. However, good linearity of the frontend cannot compensate for the deviations from linearity of the chirp signal. The chirp signal should also have a linear frequency rise and fall to prevent spurs in the output signal. [29, p.29]

As described, each of the components affects the overall performance of the system and should therefore be deliberately investigated and chosen before the overall system is simulated.

3.2 Frequency multiplier

An important component that is almost always used in high frequency systems is a frequency multiplier. The main purpose is to generate an output signal, which is based on the harmonic of its input frequency. This allows a simpler signal generation for a radar in a much lower frequency range than the amplification and radiation. The main idea during designing a multiplier is to generate such a strong nonlinearity, that more or less the new signal appears mainly at the desired harmonic frequency. Additionally, the baseband bandwidth Δf_{BB} will be increased by the multiplication factor $n\Delta f_{\mathrm{BB}}$. Likewise, the frequency change in the passband is also faster by a factor of n. At this point, however, the disadvantages should also be mentioned, which are the degradation of phase noise (by $20\log(n)$) and the generation of unwanted harmonics. [43, Ch.5, pp.2-3]

Typical values to describe and compare frequency multipliers are the multiplication factor n, the maximum output power P_{out}, the conversion gain G_{C}, which is the ratio of the output power at the wanted harmonic frequency nf_{in} to the input power at the fundamental frequency f_{in}. Other parameters are the supression of the unwanted harmonics, the bandwidth and the efficieny. As with any other component, power matching to the previous circuit, or in this case the signal source and the subsequent circuit, plays an important role. The use of $50\,\Omega$ as the characteristic impedance of all circuits avoids the use of lossy matching networks and allows direct chip-to-chip interconnection. The units of measurement utilized are the input and output return loss. It describes the ratio of incident power to reflected power at each port. [43, Ch.5, p.5]

3.2.1 HMC1110

There are only a few multipliers that can be purchased of the shelf as a die and cover the desired output frequency range from 70 GHz to 90 GHz, which is part of the E-band. Moreover the multiplication factor n should be large, so that the system benefits from the use of the multiplier as

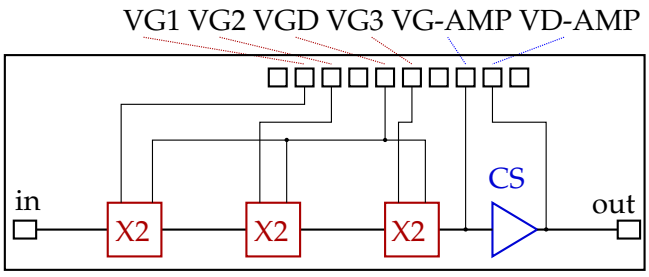

Figure 3.1: Schematic representation of the internal structure of the X08004.

described above. One possibility is the HMC1110 from Analog Devices, that is a times-six multiplier with a maximum output power of $P_{\text{out}} = 13\,\text{dBm}$, an output frequency range from 71 GHz to 86 GHz and a minimum required input power of $P_{\text{in}} = 0\,\text{dBm}$. [16]

It is also possible to connect several dies in series, like frequency doublers. However, this would not only increase the complexity, but also the number of necessary power supplies, the lossy transitions, the costs and the space requirement, which is why this is not realized. In addition, when using several individual multipliers, care must be taken that the respective desired frequency band of the subsequent stage does not overlap with the frequency bands of the harmonics of the preceding stage. Otherwise, these would generate further harmonics through the chain. Another way to suppress these harmonics is filtering, but this requires additional space and eliminates the desired chip-to-chip connection. [43, Ch.5, pp.28-29]

3.2.2 X08004MB

During the ELiPSe project (E-Band link platform and test for satellite communication (ELiPSe)) at the ILH of the University of Stuttgart multiple frequency multipliers where developed. One of them covers both frequency bands (71 GHz to 76 GHz and 81 GHz to 86 GHz) and is thus suitable in terms of frequency range.

As shown in Fig. 3.1, the frequency multiplier consists of three stages and an output buffer. Both the individual frequency doublers and the amplifier are constructed from individual transistors in common-source configuration. The MMIC was designed and fabricated in an InAlAs/ InGaAs grounded coplanar IC process on a GaAs substrate with a transistor gate length of 50 nm. The first-stage metamorphic HEMT (mHEMT) has a gate width of 30 µm and two fingers. The subsequent second and third stage transistors are 2x50 µm and 2x45 µm transistors. The amplification is done by a 4x45 µm transistor. The gain of the buffer is always above 7 dB in the relevant frequency range. The individual multiplier stages are separated by serial capacitors to allow individual biasing and the input and output of the chip are also provided with direct current (DC) blocks.

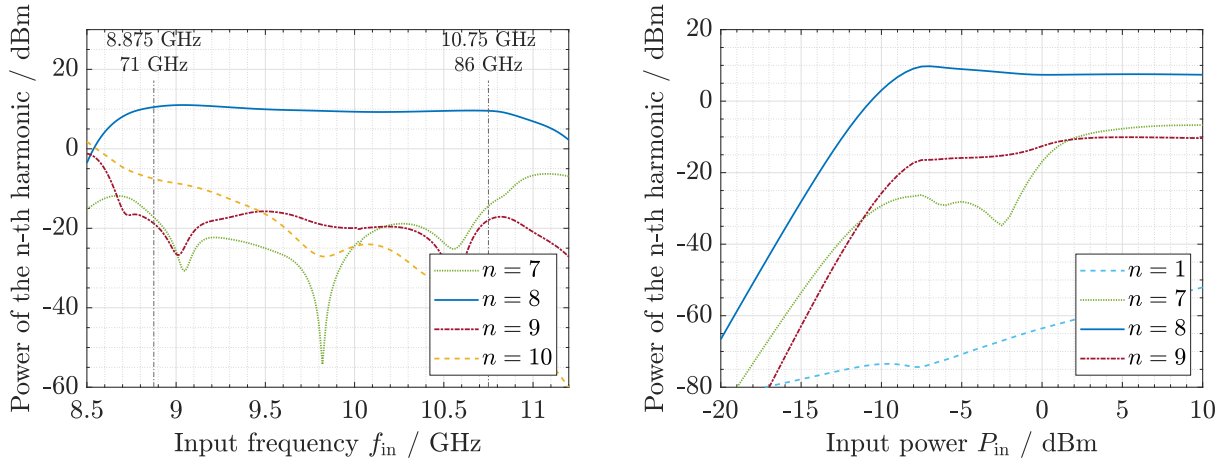

(a) Harmonics vs. input frequency

(b) Harmonics vs. input power

Figure 3.2: The generation of harmonics is plotted over the input frequency in a) for a power of $P_{in} = -7\,\text{dBm}$ and considered in b) for a frequency of $f_{in} = 77\,\text{GHz}$ over the input power.

3.2.3 Comparison of the frequency multipliers

The values in the Comparison Table 3.1 of the HMC1110 were taken from the data sheet [16]. Simulation models are available in Advanced Design System (ADS) for the X08004 since it was designed at the ILH. They were used to simulate the values. Part of the simulation results are shown in Fig. 3.2.

Table 3.1: Comparison of two possible frequency multipliers.

Value	Unit	HMC1110	X08004MB
Manufacturer		Analog Devices Inc.	ILH
Technology		GaAs	GaAs
Multiplication factor n	1	6	8
Input frequency range	GHz	11.83 – 14.33	8.75 – 10.84
Output frequency range	GHz	71 – 86	70 – 86.7
Min. input power	dBm	0	−7
Min. output power	dBm	13	8.8
Harmonic suppression $(n-1)$	dBc	23	20
Harmonic suppression $(n+1)$	dBc	34	25
Max. supply voltage	V	4	1.4
Power consumption	W	0.13	0.13
Dimensions	mm	2.44 ∗ 1.35 ∗ 0.1	3 ∗ 1.25 ∗ 0.05

The comparison of the two possible frequency multipliers shows that the X08004MB not only has a larger multiplication factor and a slightly wider frequency range, but also requires less input power. For this reason and the presence of simulation models, it is chosen for use in the transmitter. In addition, on-wafer measurement results are available for the produced MMICs. The frequency multiplier (cell 40), which is placed during this research, has a usable frequency range

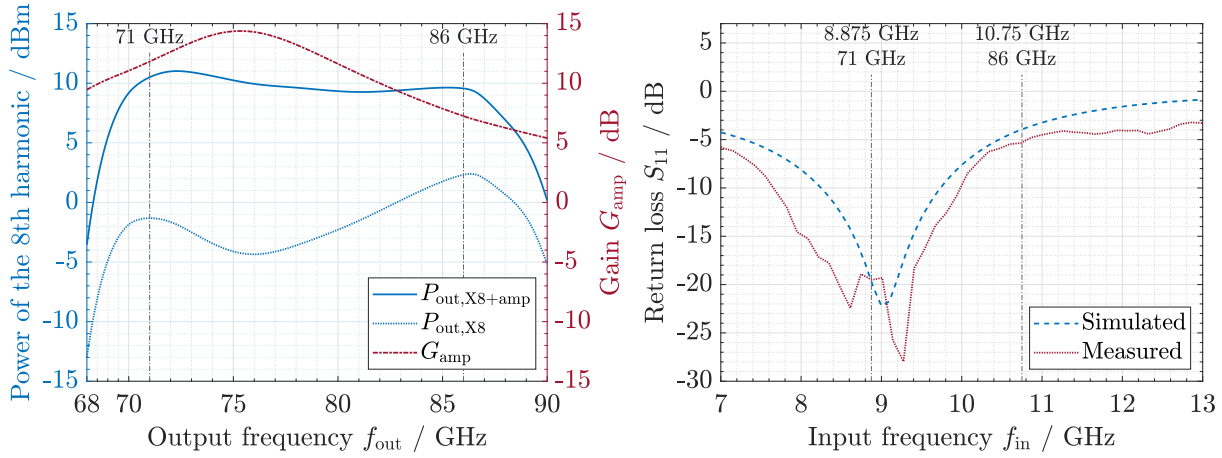

(a) Examination of X8 buffer

(b) Return loss

Figure 3.3: The gain of the output buffer is shown together with the output power after the three multiplier stages and after the buffer in a). The input power is −7 dBm. The simulated input return loss is compared to the measured one in b).

beyond 88 GHz. However, the output power turns out to be lower and is at least 4.5 dBm over the whole frequency range, with an input power of −3 dBm. Such a high input power is not necessary, but was only chosen to measure all MMICs on the wafer to account for component tolerances. For the selected MMIC, the minimum required input power is −7 dBm at a frequency of 81 GHz at the output and thus corresponds to that of the simulation. The simulated gain of the multiplier is at least 12.5 dB and is thus in the same range as that of the HMC1110. However, due to the lower achieved output power in the measurement, the gain in reality of at least 7.5 dB is also significantly lower than that of the purchasable MMICs.

Fig. 3.3a shows the output power after the multiplier stages and the output power after the buffer. The buffer has a gain of at least 7 dB and at the same time compensates for the output power of the multiplier stages. In the later course, the gain of the buffer can be adjusted if the following amplifier compresses. In Fig. 3.3b the input return loss from the simulation is compared with the measurement of the placed MMIC. Negligible deviations are shown, with the simulation being more conservative.

3.3 Power amplifiers

Amplifiers will be found in almost every communication or radar system. On the transmitter side power amplifiers are used to achieve the desired high output power to drive the Tx antenna and precompensate upcoming propagation losses. In many cases, these losses are so high that another amplifier directly connected to the Rx antenna, often a low-noise amplifier, is used to amplify the received signal in a way, that subsequent components can handle the signal. Amplifiers are also used between modules to achieve the required input powers.

When designing an amplifier or comparing different ones, there are several typical values which are considered. The most obvious value is the gain, which is the ratio of output to input power. For higher input power values the output power begins to saturate. The maximum output power which remains constant even if the input power is further increased is called saturated power P_{sat}. The point at which the difference to the ideal linear slope is 1 dB is called the 1 dB-compression point, which can be related either to the input or the output (*ICP* and *OCP*). In addition to decreasing gain, signal distortions also occur. As a result, intermodulation products and harmonics can be seen in the output spectrum. The reason therefore is signal clipping e.g. due to $V_{\text{GS}} > V_{\text{th}}$ of a common-source amplifier. The generation is not the same for each harmonic, but up to the compression they can be described by certain slopes, e.g. first harmonic with 3 dB and the second harmonic with 6 dB. After reaching the compression point, the slopes no longer represent the course, but sweet spots with lower harmonic contributions arise, which should be exploited. Another figure of merit to describe linearity is the third-order intermodulation intercept point. Therefore two sinusoidal signals are applied at the input. The theoretical intersection of the fundamental tone and the third order tone in a log-log plot is called third order intercept point, that can be referred to the input (*IIP*3) or the output (*OIP*3). If the amplifier was not designed for high power but for low noise, the noise figure (*NF*) becomes relevant. This type of amplifier is typically located at the beginning of a chain of components/amplifiers, as it is decisive in the overall noise of the chain. It is also helpful to know the noise figure for other types of amplifiers if they are situated at the beginning of the Rx, because together with the thermal noise and any further margin the minimum detectable signal can be calculated (see chapter 3.1). From the point of view of output power, the dynamic range of an amplifier covers the output-related minimum detectable signal up to the 1 dB compression point. Last but not least, the efficiency of an amplifier can also be critical if it is used in an energy critical applications, eg. battery powered. [44, Ch.7, pp. 2-8]

3.3.1 Low noise amplifier - HMC8325

In addition to the frequency multiplier, Analog Devices also offers four different amplifiers for the desired frequency range between 71 GHz and 86 GHz. Only the low-noise amplifier of type HMC8325 is recommended for the creation of a new design. Even if a mass-market radar system is not to be designed, the use of this MMICs suggests itself due to its significantly higher gain (typically 21 dB) compared to the other three products. These have gains ranging from 13 dB to 15 dB [13][14][15].

The amplifier consists of four gain stages, with the first two stages having a shared gate as well as drain bias voltage. Likewise, the bias voltages for the last two stages are interconnected. Applying different voltages to the combined gain stages allows either to achieve the highest possible gain as well as a low noise figure or to improve the third order intercept point. [1]

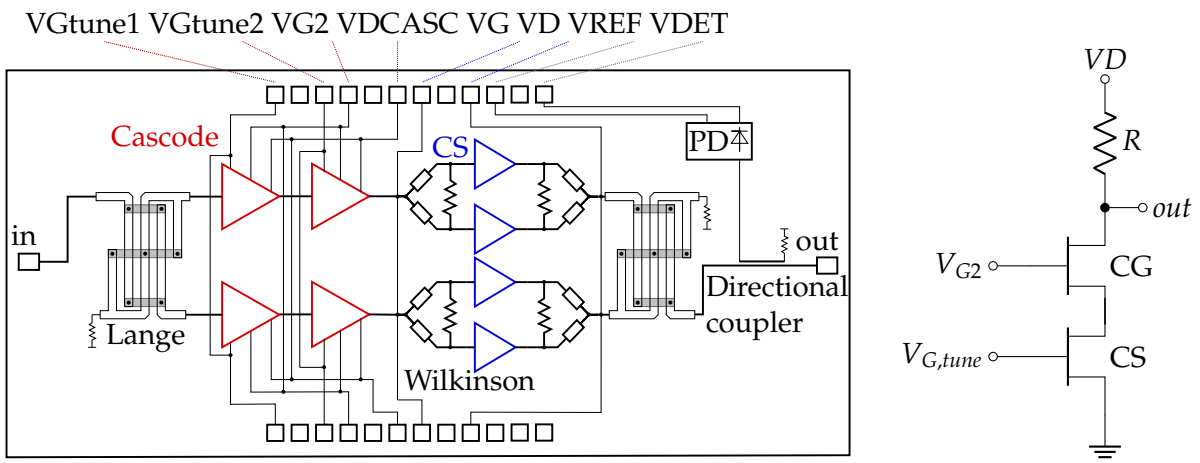

(a) Investigation **(b)** Cascode

Figure 3.4: In a) the internal structure of the AMP101 amplifier is shown. The setup of a cascode is illustrated in b).

3.3.2 Power amplifier - AMP101

At ILH, two amplifiers were designed in the same technology as the frequency multiplier, which could be considered for application in the radar system. First, the structure of the AMP101 will be described.

As shown in Fig. 3.4a, it consists of several serial and parallel gain stages. Additionally, there is an unbiased diode detector on the MMIC. Since no biasing is applied, there is no voltage across the reference diode, which is normally used to compensate for the temperature dependence of the current–voltage characteristic. A part of the transmit signal is decoupled from the output signal path via a 20 dB directional coupler and rectified by the diode. The result is a DC voltage proportional to the transmit power.

At the input of the amplifier there is a Lange coupler which divides the amplifier into two branches. This type of balanced topology offers one major advantage. Both the input and output of the amplifiers have a visible impedance of 50 Ω due to the termination of the Lange couplers, absorbing reflections and thus allowing good matching to previous and subsequent circuits. [51, p.586]

Two cascode stages follow, which are built from the same cascode. A cascode consists of a cascade of a common source (CS) transistor (4x30 µm) and a common gate transistor (4x30 µm) without an interstage matching network. A schematic representation of a cascode can be found in Fig. 3.4b. The common gate transistor is the low impedance load for the CS transistor. When an input signal is applied to the gate of the CS transistor, it starts to conduct and the gate source voltage of the common gate increases. Despite the lower efficiency, due to the current flow through both transistors and the doubled drain source voltage, which is necessary for biasing both transistors via the upper drain, the use of a cascode offers several advantages. Since the drain voltage of the CS transistor is nearly constant, and the voltage gain is thus $A_V \approx -1$, the Miller effect comes into play only slightly. This effect states that the gate-drain capacitance contributes significantly

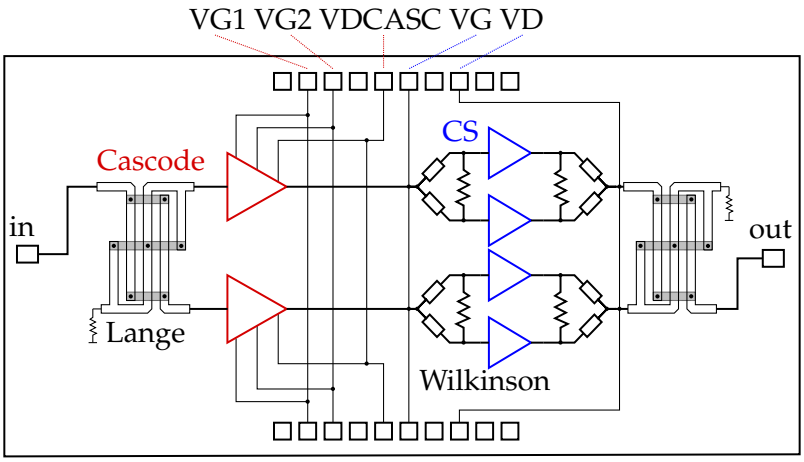

Figure 3.5: Schematic representation of the internal structure of the AMP002.

more to the input capacitance of the transistor, more precisely by a factor of $|A_V|+1$, than the gate source capacitance. An increased input capacitance would reduce the bandwidth of the amplifier. Also the drain-gate capacitance of the common gate transistor does not matter, because there is a capacitance to ground in the gate path, which forms a low impedance path for the expected frequencies to charge and discharge the stray capacitance. Since the output is not directly connected to the input, the isolation of the input is also improved. In addition, the output impedance and the gain are also larger compared to the simple CS transistor. [43, Ch.6, pp.18-26] [55]

After the second cascode the output stage follows. In order to increase the output power, a Wilkinson divider is used whose outputs each control a gate of a common-source stage. All transistors have four fingers and a gate width of 45 µm. The outputs of the CS stages are combined by another Wilkinson divider and connected to the second Lange coupler. [55, p.9]

3.3.3 Power amplifier - AMP002

The design of the AMP002 is similar to the design of the AMP101. However, there is only one cascode stage consisting of a 4x45 µm transistor per branch. Also the gate width of the transistors in the CS stage is wider width 55 µm. Furthermore, there is no possibility for power detection. The structure is shown in Fig. 3.5.

3.3.4 Comparison of the amplifiers

A simulation model and on-wafer measurement results for the AMP002 are available. For the AMP101 amplifier designed at ILH, the existing simulation models of the AMP100 were used. The simulation model has the same performance as the AMP101, which was developed due to poor measurement results of the AMP100. The former was used to determine the figures of merit of the amplifier. In contrast, the values in Table 3.2 are taken from the data sheet of the HMC8325.

The Table shows the minimum values in each case when the biasing is set for maximum gain.

Table 3.2: Comparison of the three amplifiers presented.

Value	Unit	HMC8325	AMP101 [*1]	AMP002
Manufacturer		Analog Devices Inc.	ILH	ILH
Technology		GaAs	GaAs	GaAs
Gain	dB	20	24.4	14.1
Sat. output power	dBm	15	22	20
ICP	dBm	−8	−10.2	0.5
OCP	dBm	12	17	16
Frequency range	GHz	71 − 86 [*2]	60 − 90	65 − 90
*IIP*3	dBm	1	−0.6	11.1
*OIP*3	dBm	22	27.5	27.4
Input return loss	dB	8	13.9	12.9
Output return loss	dB	11	14	13.7
Noise figure	dB	3.6	–	–
Max. supply voltage	V	4.5	2	2.4
Power consumption	W	0.22	0.58	0.81
Dimensions	mm	2.844 ∗ 0.999 ∗ 0.05	4.5 ∗ 2 ∗ 0.05	3 ∗ 1.5 ∗ 0.05

[*1] Instead of AMP101, the simulation model of AMP100 was used
[*2] Charts in data sheet are only shown in this frequency range

Exceptions to this are the power consumption and the supply voltage. In the case of the HMC8325, the diagrams are only available in the frequency range from 71 GHz to 86 GHz. As a conclusion, the values of the AMP101 and AMP002 were also evaluated only in this range. An increase of the frequency range does not play a role since the frequency multiplier only covers this range. The two-tone simulation to determine the *IIP*3 as well as the *OIP*3 were performed for a frequency difference of 1 MHz for the frequencies from $f_{LO} = 78.5$ GHz to 71 GHz and 86 GHz with a step size of 1 GHz. The gain is determined from the small signal analysis. For an input power of $P_{in} = 4$ dBm, as expected from the multiplier, the gain for the AMP101 is still at least 21.4 dB and for the AMP002 13.0 dB. The small signal gain is necessary for the amplifier after the receiving antenna because the expected signal is much smaller.

The comparison shows that AMP101 and AMP002 have a higher *OCP* than the competitor. This means that the two amplifiers can also produce higher output powers while still functioning approximately linear. Therefore, the AMP002 is a good choice as an amplifier on the Tx side. The *IIP*3 is above the expected input power and the maximum output power is only slightly below that of the AMP101. A high gain is not necessary because already the multiplier provides such a strong output signal that the AMP002 starts to compress. This can be counteracted, for example, by adjusting the bias voltage of the buffer stage of the multiplier as mentioned above. This not only improves the linearity of the system, but also increases efficiency.

An excerpt of the simulation results can be found in Fig. 3.6. Here, the output power is considered on the left side, as well as the gain for several frequencies over the input power. The small signal parameters are found on the right side. Where S_{21} corresponds to the small signal gain and S_{11} and S_{22} represent the return loss. The on-wafer measurements for AMP002 (cell 46 is used in the

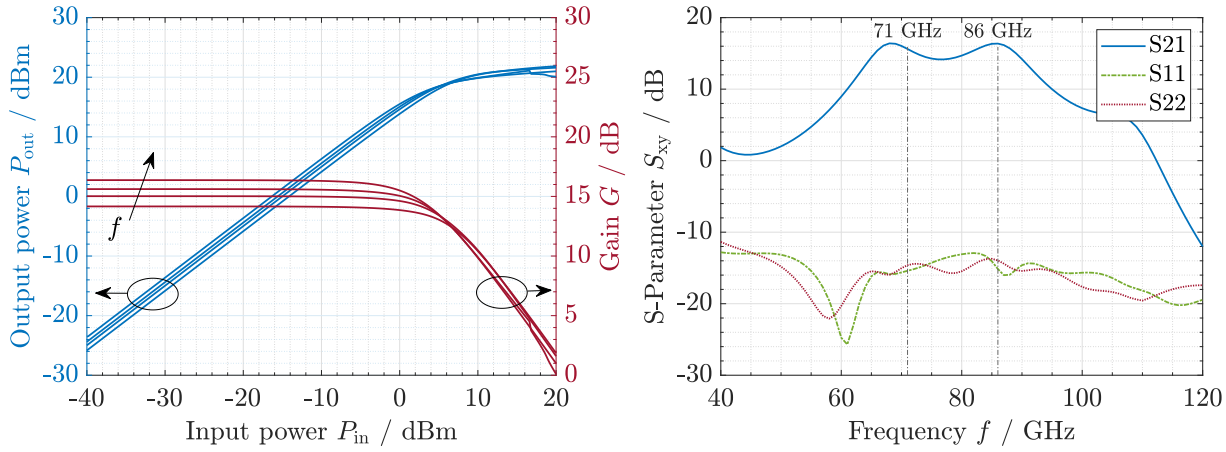

(a) Input power sweep **(b)** Frequency sweep

Figure 3.6: In a), the output power and gain for frequencies 71 GHz, 76 GHz, 81 GHz, and 86 GHz are plotted versus the input power of the amplifier AMP002. The small signal parameters are given in b).

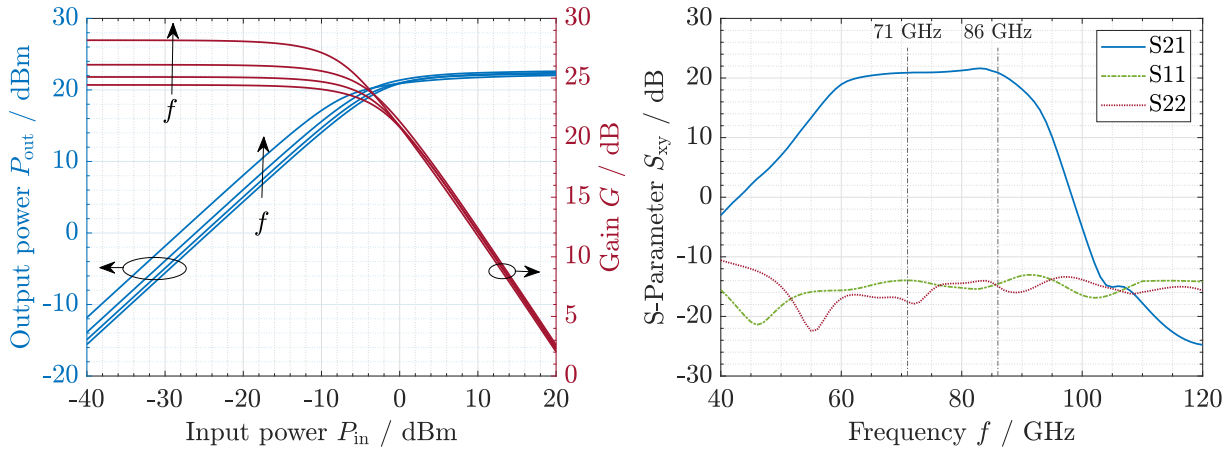

(a) Input power sweep **(b)** Frequency sweep

Figure 3.7: For different frequencies (71 GHz, 76 GHz, 81 GHz, and 86 GHz) the output power and the gain are plotted in a) versus the input power of the amplifier AMP101. The small signal parameters are given in b).

setup) show a small signal gain which is in the range between 12.7 dB and 14.0 dB, deviating only slightly from the simulated gain.

In contrast to the HMC8325, the AMP101 has a higher output power and greater gain, which makes it suitable for use in the Rx path. In addition to a lower maximum necessary voltage, which facilitates battery operation, the matching is also better. A corresponding gate voltage can be specified for each stage, but the drain current is shared between the two cascode stages in the AMP101, as can be seen in the previous Fig. 3.4a. A series resistor at the beginning and at the end of each branch prevents DC current from flowing and thus the operating point from shifting. In

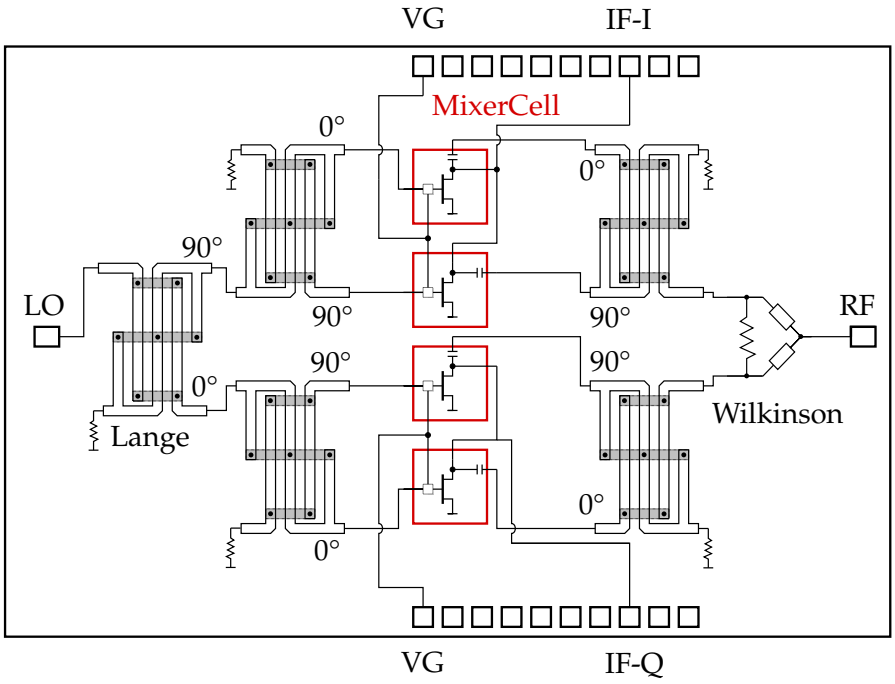

Figure 3.8: Schematic representation of the internal structure of the MFM005.

the same way as AMP002, the simulation results are shown in Fig. 3.7. Which allows a simple comparison and thus the recognition of the mentioned characterisitka.

3.4 Mixer

The main difference to the radar systems used so far is the connection between Tx and Rx. Typically, a sufficiently large portion of the transmit signal is decoupled and routed to the LO input of the mixer, that is part of the Rx. In the radar system under investigation, this path no longer exists, so both LO and RF are obtained from the received signal. Accordingly, the structure of a self-mixing mixer does not correspond to that of the familiar downconversion mixer with its three gates LO, RF and IF anymore. The MFM005MB, which was designed at the ILH by Christopher Grötsch for the ELiPSe project, will be used. This is a resistive mixer, in which the channel conductance is changed by the LO signal at the input. Just like the previous circuits, it was manufactured using gallium arsenide (GaAs) technology. The mixer consists of four resistive mixer cells connected as shown in Fig. 3.8. On the LO side, the signal is divided into two branches by a Lange coupler, making the mixer a quadrature mixer. Another Lange coupler per branch connects the two mixer cells, each consisting of a $4x10\,\mu m$ transistor in CS configuration, to the respective gate. From the RF point of view, the signal is first split by a Wilkinson divider before it is also fed by a Lange coupler to each of the two mixer cells. They are connected to the drain of the respective transistor. The corresponding quadrature IF port is also located at these. Before the possible configuration variants of the mixer are shown, the most important characteristics of mixers will be discussed briefly.

As with most circuits, one of the main figure of merits is the conversion gain (CG). But compared to amplifiers, this value is not fundamentally positive, which is why there is sometimes talk of conversion loss. For a downconversion mixer, the conversion gain (CG) is the ratio of IF power to RF power assuming constant LO power. Another important parameter is the bandwidth, which is closely related to the matching. Just as with amplifiers, signals should not be distorted, which is why linearity is also considered. As shown in equation 3.10, the last component of a module chain has the greatest influence on the overall linearity of the system. The associated quantities are the 1 dB-compression point considering the CG and the intermodulation products. While in an amplifier the third order intermodulation products are the relevant ones for input signals close to each other, since e.g. $2f_1 - f_2 \approx f_1$ applies for $f_1 \approx f_2$ and thus these cannot simply be filtered out, at least parts of the second order intermodulation products fall within the relevant frequency range in the downconversion mixer. For example, if we consider the input signals $f_{\mathrm{RF},1} = 78.501\,\mathrm{GHz}$ and $f_{\mathrm{RF},2} = 78.502\,\mathrm{GHz}$, which differ by 1 MHz, and the LO signal at $f_{\mathrm{LO}} = 78.5\,\mathrm{GHz}$, then on the IF, on the one hand, the desired signals at $f_{\mathrm{IF},1} = f_{\mathrm{RF},1} - f_{\mathrm{LO}} = 1\,\mathrm{MHz}$ and $f_{\mathrm{IF},2} = f_{\mathrm{RF},2} - f_{\mathrm{LO}} = 2\,\mathrm{MHz}$ occur, but also the mixed product of the two RF signals. This also falls on the IF signal $f_{\mathrm{IF},1} = 1\,\mathrm{MHz}$ for $f_{\mathrm{RF,mix}} = f_{\mathrm{IF},2} - f_{\mathrm{IF},1}$. [42]

Ideally, only the IF signal is visible at the IF port, which conversely means that the RF and LO signal are completely suppressed. This is not the case in practice, which is why isolation between the individual ports is considered. The LO signal is typically the signal with the highest power and therefore the signal of the two, which is more likely to be seen on the third port. Last but not least, power consumption as well as added noise also play a role in many applications.

The noise power of the RF input signal is $N_{\mathrm{RF}} = \mathrm{k_B}TB$, where $\mathrm{k_B}$ is the Boltzmann constant, T the temperature and B the bandwidth of the RF signal. Thus, for the input SNR, $SNR_{\mathrm{RF}} = P_{\mathrm{RF}}/N_{\mathrm{RF}}$ with P_{RF} the power of the RF input signal. For a downconversion mixer, the power of the downconverted signal is $P_{\mathrm{IF}} = G_{\mathrm{C}} \cdot P_{\mathrm{RF}}$, where G_{C} denotes the CG. The noise on the receiver side results from two sidebands: $f_{\mathrm{LO}} - f_{\mathrm{IF}}$ and $f_{\mathrm{LO}} - f_{\mathrm{IF}}$. This results in the output SNR

$$SNR_{\mathrm{IF}} = \frac{GC \cdot P_{\mathrm{RF}}}{(G'_{\mathrm{C}} + G''_{\mathrm{C}})\mathrm{k_B}TB}, \tag{3.11}$$

with the CGs G'_{C} and G''_{C} of the two bands. Thus, the following applies to the noise factor

$$F = \frac{SNR_{\mathrm{RF}}}{SNR_{\mathrm{IF}}} = \frac{P_{\mathrm{RF}}}{\mathrm{k_B}TB} \cdot \frac{(G'_{\mathrm{C}} + G''_{\mathrm{C}})\mathrm{k_B}TB}{G_{\mathrm{C}} \cdot P_{\mathrm{RF}}} = \frac{G'_{\mathrm{C}} + G''_{\mathrm{C}}}{G_{\mathrm{C}}}. \tag{3.12}$$

With an ideal mixer, the CG is equal so that $G_{\mathrm{C}} = G'_{\mathrm{C}} = G''_{\mathrm{C}}$ applies to both bands. For the noise factor this results in

$$F = \frac{G'_{\mathrm{C}} + G''_{\mathrm{C}}}{G_{\mathrm{C}}} = \frac{2G_{\mathrm{C}}}{G_{\mathrm{C}}} = 2 \tag{3.13}$$

and for the logarithmic noise figure $NF = 3\,\mathrm{dB}$ is calculated. In a real mixer, not only the powers from two sidebands fall into the IF frequency range, but from several ranges, further degrading the noise figure. In addition, the mixer itself adds further noise. [49, 3-5]

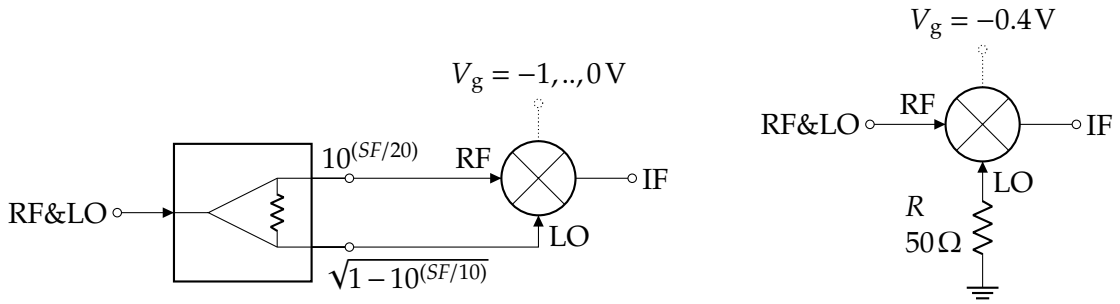

(a) Investigation **(b)** Final Circuit

Figure 3.9: The left circuit shows the mixer in self-mixing configuration including splitter for split factor *SF* determination. The right side shows the final selfmixing configuration.

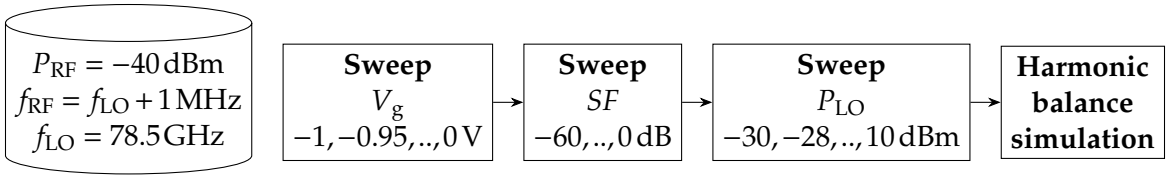

Figure 3.10: The flow chart shows the simulation procedure for determining the mixer's split factor *SF* in self-mixing mode.

3.4.1 Self-mixing configuration

The purpose of this subsection is to clarify the issue of connecting the mixer so that a self-mixing operation is created. It is obvious to find out by a harmonic balance (HB)-simulation in which ratio the combined RF and LO signal has to be applied to the RF and LO port of the mixer. For this purpose, the circuit shown in Fig. 3.9 is examined. The introduced variable *SF* is the abbreviation for the split factor, which describes the attenuation of the combined *RF*&*LO* signal by the splitter in the direction of the RF-port of the mixer. The attenuation in the direction of LO port can be calculated by $\sqrt{1-10^{SF/10}}$. During this, the supply voltage, which is applied to each gate of the transistors, is varied as shown in Fig. 3.10. For the LO signal with a frequency of $f_{LO} = 78.5\,GHz$ a signal power between $P_{LO} = -30\,dBm$ and $10\,dBm$ is applied. The LO input power range is oriented to expected values and at the same time high enough to draw conclusions about the linearity. The values for the RF signal are set to $f_{RF} = f_{LO} + 1\,MHz$ and $P_{RF} = -40\,dBm$ and the gate bias voltage is swept from $-1\,V$ to $0\,V$. The simulation result shown in Fig. 3.11 states that the mixer should be terminated on the LO port and the gate voltage should be chosen to $V_g = -0.4\,V$. This means that both signals are applied to the RF port.

Now the question arises how the output of the mixer must be terminated to achieve the maximum gain. For this purpose, under the same conditions as above and with an input power of $P_{LO} = -10\,dBm$, it was investigated how the now open LO output of the mixer should be terminated. Varying the resistor value in a range from $1\,\Omega$ to $10\,k\Omega$, a change of $1.8\,dB$ can be found for the IF Q output, where for higher resistance values the CG decreases. For the IF I output the behavior is reversed. It can be observed that for a resistance value of $40\,\Omega$, the two quadrature outputs of the

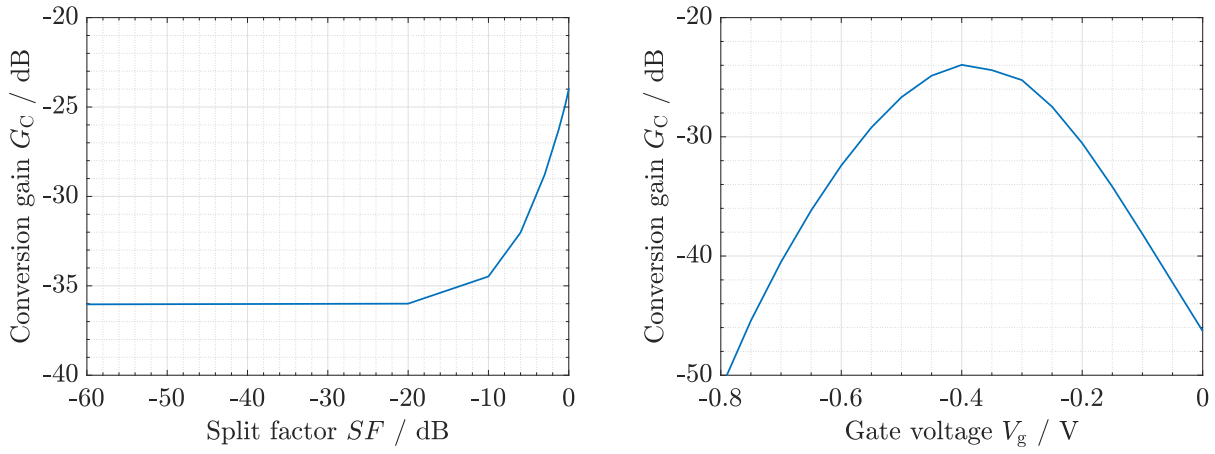

(a) Split factor sweep **(b)** Gate voltage sweep

Figure 3.11: In a) the conversion gain G_C is plotted versus the split factor SF of power splitter. Shown is the course for $V_g = -0.4\,V$ and $P_{LO} = -10\,dBm$. For a constant SF of $0\,dB$ and $P_{LO} = -10\,dBm$, the variation of the G_C over the gate voltage is shown in b).

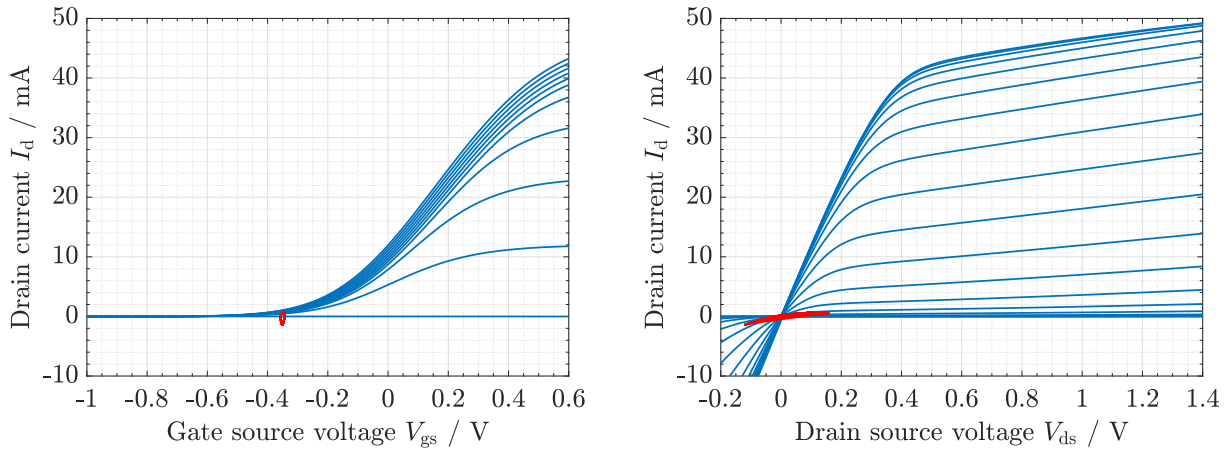

(a) Transfer characteristics **(b)** Output characteristics

Figure 3.12: The dynamic transfer and output characteristic for a self-mixing mixer consisting of one transistor is shown.

mixer have the same CG. Due to the fact that the LO port is normally driven by a high-frequency signal carried over a line with a characteristic impedance of $Z_0 = 50\,\Omega$, the resistance is also chosen to be $50\,\Omega$.

The behavior of this circuit can be explained by taking a look at the output characteristic of a single transistor and keeping in mind that a mixer exploits the non-linear behavior of components and only a constant voltage is applied to the gate. An exemplary course of the drain current over the two voltages V_{gs} and V_{ds} for one single mixer cell is presented in Fig. 3.12. For reference, on the one hand, the transfer characteristic for drain source voltages between $0\,V$ and $1\,V$ and on the other hand the output characteristic for gate source voltages between $-1\,V$ and $1\,V$ is depicted as well.

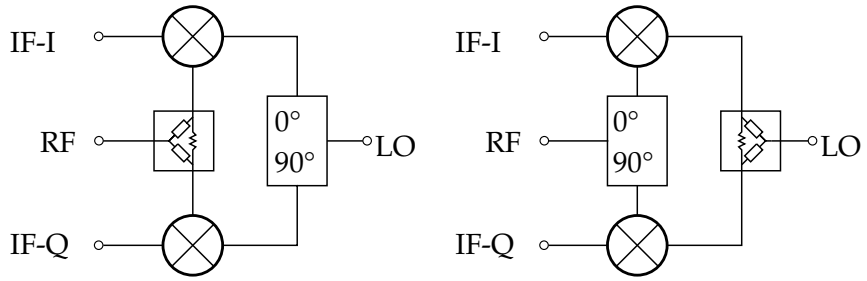

Figure 3.13: IQ structure creation through a Wilkinson and a Lange coupler.

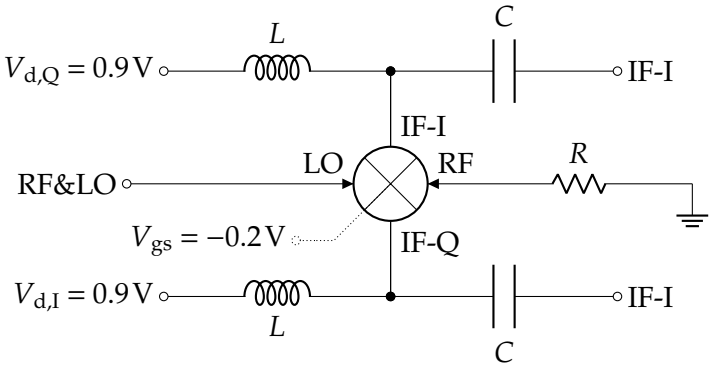

Figure 3.14: The circuit shows the mixer in transconductance configuration.

In this case the mixing is justified in the non-linear drain current / drain source voltage correlation.

As already mentioned, small changes in distance can be detected with the help of the phase difference. In addition, it can also be used to detect the beginning or the end of the chirp signal period. This is necessary for the signal evaluation since the observation window for the evaluation of the received signal by means of fast Fourier transform (FFT) can orient to this. Since the ADC can only capture the real part of a signal, the complex plane must be rotated. Generally, for this purpose, either the LO is mixed down with the RF signal and its duplicate shifted by 90° or the LO signal is shifted in the same way and mixes down the RF signal. Both structures are illustrated in Fig. 3.13. The simulation shows that detection of the phase is no longer possible. This is also evident from looking at the internal circuit of the MMIC. By feeding the two mixer signals to one port, the RF port, there is no phase shift between the IF ports anymore.

For clarity and comparison, the resulting values from various simulations can be found in the Table 3.3, which follows the discussion of the transconductance mixer.

3.4.2 Transconductance mixer

Another mixer topology is the transconductance mixer, shown in Fig. 3.14. As the name indicates, the nonlinear transconductance, i.e. the ratio between the change in output current and the change input voltage of a single transistor, is used for mixing. This configuration cannot be applied to any off the shelf mixer MMIC, but only after considering the internally placed filters, couplers and

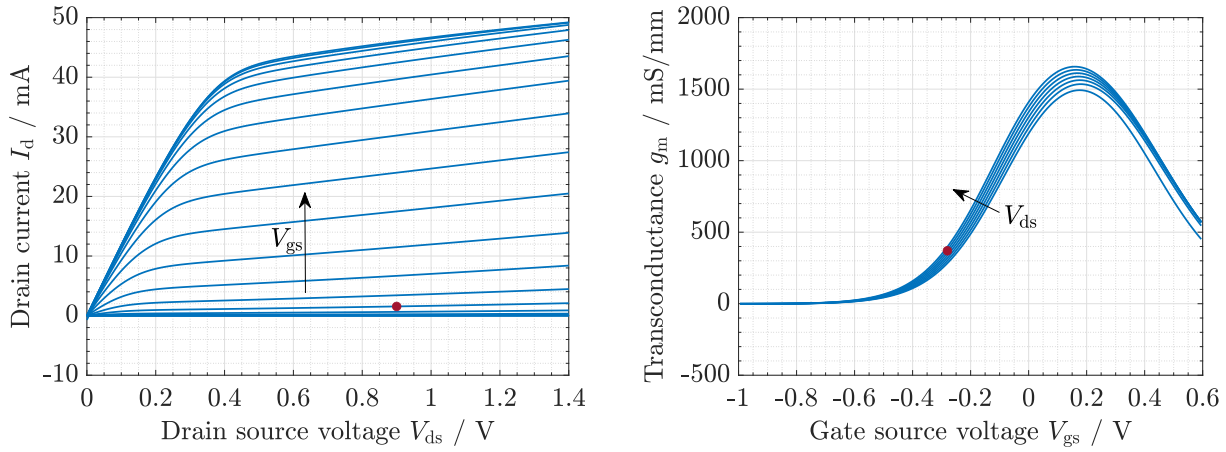

(a) Output characteristics **(b)** Transconductance

Figure 3.15: In a) the output characteristics is plotted. The gate source voltage is swept between −1 V and 1 V with 100 mV steps. The variation of the transconductance across V_{gs} is shown in b), where the drain source voltage ranges from 0.3 V to 1 V. In both diagrams the selected bias point is marked by a red dot.

DC-blocks. Therefore, it is advantageous that the mixer was developed at the same institute.

As can be seen in Fig. 3.8, the IF ports are directly connected to the drain of each transistor. The RF port cannot be used for DC biasing because, first, the Lange couplers do not provide a physical connection between the coupling conductors and, second, the paths are DC decoupled by serial capacitors.

The investigation for the optimum operating point starts from a transistor. Here, the drain source voltage V_{ds} must be greater than the knee voltage so that the transistor is in saturation. When varying the gate source voltage V_{gs}, the transconductance g_m can now be determined by observing the drain current.The corresponding plots are given in Fig. 3.15. While for class A amplifiers the maximum transconductance is used, the biasing of a mixer should be chosen so that for negative amplitude of the strong LO signal the transconductance goes towards 0 and for positive amplitude g_m becomes large. For example, if one chooses the point at which the curvature of the transconductance becomes maximum, then $V_{ds} = 0.9\,V$ and $V_{gs} = -0.28\,V$ must be set. Thereby V_{ds} is restricted to a maximum voltage of $V_{ds} = 0.9\,V$ so that breakdown is prevented. To emphasize the difference to the self-mixing mixer, both the dynamic transfer characteristic and the output characteristic for a transconductance mixer consisting of a transistor are shown in Fig. 3.16. The gate source voltage, especially the strong LO signal, controls the drain current. According to the design, this either goes to zero or the channel conducts, which results in the mixing of the two input signals. The elliptical I-V curve results from parasitic effects.

In the next simulation, with this knowledge, the entire mixer can be simulated. The required bias tee is represented by an ideal DC block and a DC feed and is thus lossless. In contrast to the presented self-mixing mixer, there are now three voltages which can be adjusted in the simulation. Due to the symmetry of the circuit, $V_{d,I}$ and $V_{d,Q}$ are set equal and denoted as V_{ds}. Another value

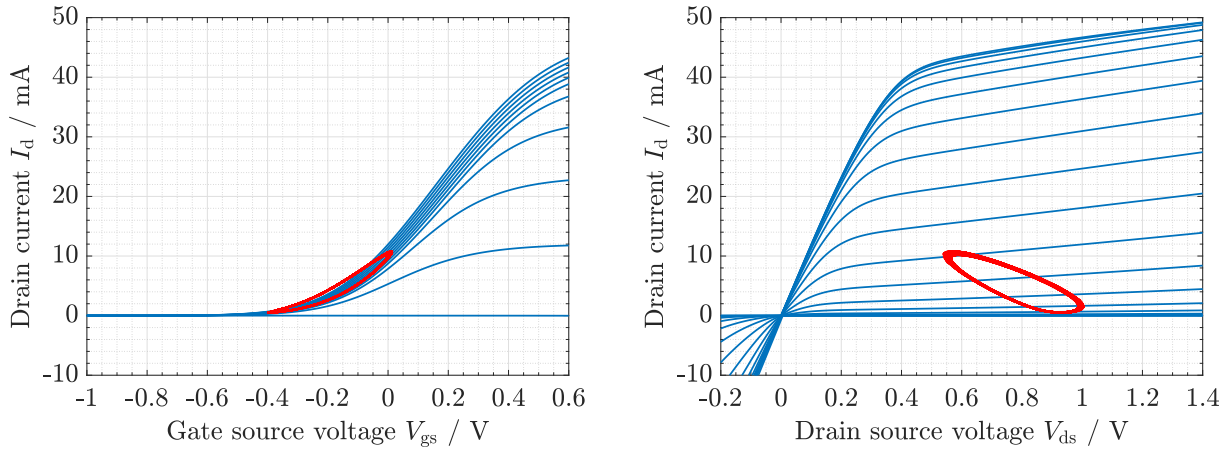

(a) Transfer characteristics **(b)** Output characteristics

Figure 3.16: The transfer and output characteristic for a transconductance mixer consisting of one transistor is shown.

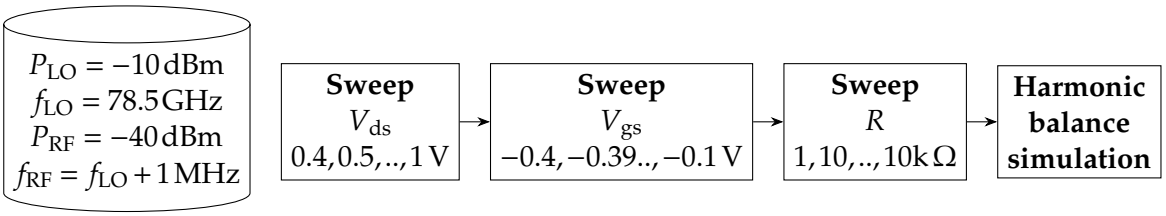

Figure 3.17: The flow chart shows the simulation procedure for determining the mixer's gate source voltage V_{gs}, drain source voltage $V_{ds} = V_{d,I} = V_{d,Q}$ and load resistance R in transconductance mode.

that can be swept is the termination resistor at the RF port. An illustration of the simulation process is given in Fig. 3.17. The values from the individual transistor analysis are also varied again since losses and parasitic effects now occur, which change the characteristic curves. The highest CG results from the highest resistance value, a drain voltage of $V_{ds} = 0.9\,\text{V}$ and a gate voltage of $V_{gs} = -0.2\,\text{V}$. Compared to the self-mixing mixer, the loss decreased from 23.8 dB to 12.73 dB. Since this simulation confirms a significant improvement in the CG due to the intrinsic amplification of this mixer topology, the realization of the bias tee will be now discussed due to additional losses.

3.4.2.1 Bias tee

As mentioned above, a bias network at the drain is necessary. To prevent that the signal is fed to the voltage source, the associated path must be high ohmic for high frequency signals. In practice, this is done by an inductor with its inductance L, for whose impedance $Z_L = j\omega L$ holds, resulting in $Z_L|_{\omega \to 0} \to 0\,\Omega$. Apart from that, the signal path should have a characteristic impedance of $50\,\Omega$ and be as loss-free as possible in the desired frequency range. The blocking of the direct current is done by a capacitor, since, speaking at the capacitor level, the field in the capacitor remains constant when a constant voltage is applied to one side of a series capacitor. The formula for the amount of

charge on the capacitor plates is $Q = C \cdot V$ and a current flow is the time derivative of the charge $i = dQ/dt = C \cdot dV/dt$. With a constant voltage $dV/dt = 0$ applied, the current is also zero. So, a serial capacitor prevents the flow of DC. This capacitor has an impedance of $Z_C = 1/(j\omega C)$ and therefore $Z_C|_{\omega \to 0} \to \infty\,\Omega$.

Important criteria for the evaluation of different bias tees are the RF bandwidth, insertion loss and mismatch at the RF port. The maximum applicable DC is determined by the coil and the maximum voltage is defined by the capacitor. A coil with a high DC-resistance, as can be caused by many turns in achieving a high inductance value, also increases the power dissipation.

The design of a bias tee can be straight forward if only one inductor is used. As mentioned before, the impedance of L is Z_L. To block the RF signal, this value should be significantly smaller than $Z_0 = 50\,\Omega$. Assuming that the IF frequency will be approximately $f_{IF} = 10\,\text{kHz}$, the minimum inductance is at least $L = Z_0/(2\pi 10\,\text{kHz}) \approx 800\,\mu\text{H}$. In order to account for manufacturing variations, inductance decreases with rising current and possible lower IF frequencies, the chosen inductance should be in a range of $L = 1\,\text{mH}$ to $10\,\text{mH}$. Since a parasitic capacitance results from the adjacent turns, a decrease in impedance follows with higher frequencies. The highest impedance results at the self-resonant frequency, which is due to the influence of the parasitic capacitances and the inductance. To prevent this effect, multiple inductors can be connect in series. Additional intermediate resistors are then required to avoid performance degredation due to interactions [56, p.4]. Another way to achieve a larger bandwidth is to use a conical inductor. Using a narrower line in the direction of the DC-path increases Z_0 of the GCPW. If the gap between the signal and ground conductors is also increased, Z_0 rises continuously. According to theory, the signal follows the path with constant $Z_0 = 50\,\Omega$ since there is no mismatch. In the same way the capacitance can be calculated from $Z_C \gg Z_0$ for $f \leq 10\,\text{kHz}$. Likewise, manufacturing deviations, capacitance decrease with rising voltage (DC-bias effect) and possible lower IF frequencies must be accounted. Therefore, the capacitance should be in a range of $C = 0.5\,\mu\text{F}$ to $5\,\mu\text{F}$.

The mentioned DC-bias effect should not be ignored during selection and simulation of capacitors. The combination of high capacitance and small size necessitates the use of materials inside the capacitor with a high dielectric constant. The use of class 2 ceramics is inextricably linked with a voltage-dependent capacitance. According to Murata, barium titanate (BaTiO3) is typically used here. The peculiarity is that the crystal structure changes with temperature. At room temperature, the tetragonal form, unlike the cubic form, has charge centers shifted from the center, leading to spontaneous polarization and thus a dipole moment. Without applied voltage, regions of homogeneous polarization form, which are called domains. Several domains, which lie close together, form a grain. Only when an external DC voltage is applied, an electric field develops and depending on the field strength, some of the dipoles align themselves. This effect is known as ferroelectricity. Since the permittivity expresses how much a material can be polarized by an electric field ($\vec{P} = \epsilon_0(\epsilon_r - 1)\vec{E}$), applying a voltage decreases the relative permittivity. [5] [39, pp.36-37,50]

Based on the above description selected components are the inductor *LPS6225-106* (manufacturer: Coilcraft) with an inductance of $L = 10\,\text{mH}$ and the capacitor *GRM155C71A225KE11* made by

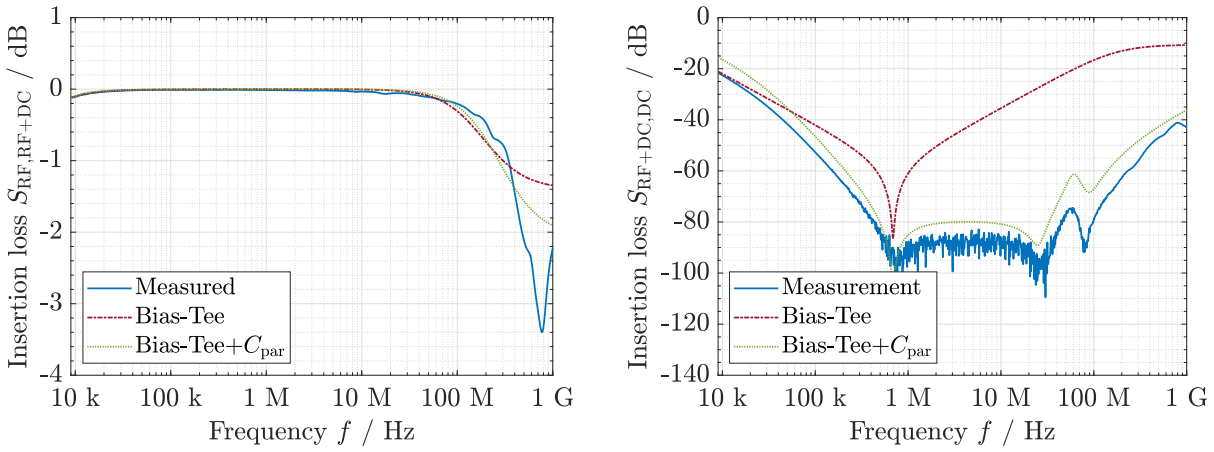

(a) RF path **(b)** DC path

Figure 3.18: Shown in a) is the insertion loss due to the bias tee in the RF path and in b) for the DC path. Compared are the simulated values with and without parallel capacitors for supply voltage attenuation and the measurement results.

Murata. The selected inductor has a high DC resistance of 70 Ω, so the DC voltage to be applied to the bias tee is now 1.4 V to maintain a drain source voltage of 0.9 V. The capacitor has a capacitance of 2.2 µF and a voltage rating of 10 V. The package size is 0402 which has a width of 0.5 ± 0.2 µm, similar to the GCPW used. These components also meet Soc and Nash recommendations, who suggest a 30 % margin to the current and voltage values and select the capacitor so that its frequency response favors the broadband nature of the bias tee [56, p.13]. [23] [6]

The simulation results are compared with the measurements of the bias tee in Fig. 3.18. For this purpose, a circuit board with test structures was designed in addition to the actual frontend PCB, where the bias tee is also placed. The measurements were made in a frequency range from 9 kHz to 1 GHz with the network analyzer. It can be seen that the simulated bias tee shows good agreement with the measurements in the RF path. In the DC path, the suppression of the RF signal is more narrowband than can be seen from the measurement shown in Fig. 3.18b. Adding the models for the parallel capacitors to ground, which are used to filter the supply voltage, these results also converge with the measurements. The bandwidth up to 345 MHz is sufficient since the chirp used has a slope of 7.5 GHz/µs. For example, assuming a relative distance between the two objects of $d = 1$ m and using the equation 2.1, a IF frequency of 50 MHz can be calculated. The special feature of the designed bias tee is the low insertion loss even for low frequencies. Starting from a frequency of 2 kHz this is 1 dB. In the range from 6 kHz to 97.5 MHz, the insertion loss for the RF signal is even below 0.2 dB. A low insertion loss enables almost lossless transmission of the downconverted signal. Coverage of the lower frequency range is necessary because the distance between objects may be much smaller than above or the chirp rate could be much lower. Commercially available surface-mounted device (SMD) bias tees, such as the BTL-0012SMG from Marki Microwave [19], only cover a range from 500 kHz without external inductance. Inserting model for the bias tee into the simulated transconductance mixer only slightly degrades the CG to

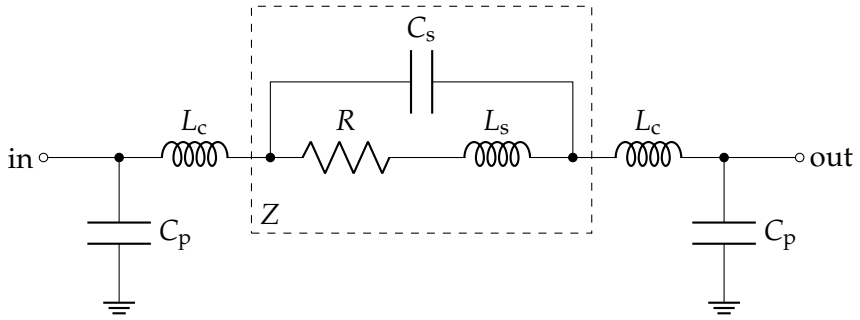

Figure 3.19: The circuit shows the equivalent circuit for a SMD resistor.

−12.76 dB for $P_{RF} = -30\,\text{dBm}$, $P_{LO} = 10\,\text{dBm}$, $f_{LO} = 78.5\,\text{GHz}$, and $f_{RF} = f_{LO} + 1\,\text{MHz}$.

Another way to bias the circuit is to insert a high impedance resistor in the DC-path to replace the inductance. However, this is a compromise, since the resistance is neither as high as in the case of a coil for high-frequency signals, nor as low as in the case of DC signals, resulting in higher DC losses. In addition, the applied voltage must be greater to compensate for the voltage drop across the resistor. This can lead to maximum voltage values, which must be provided by the source, for example by a battery, being exceeded. Simulations have shown that the resistor value should be 330 Ω or more to achieve a high CG. With a drain current of $I_D = 7\,\text{mA}$, the supply voltage is 3.17 V. Compared to the transconductance mixer with inductance in the bias tee and under the associated simulation conditions, the CG decreases to −13.8 dB

3.4.2.2 Resistive load

This subsection is dedicated to the load needed to terminate the RF output of the mixer. The influence of the value on the behavior of the mixer and which value it should optimally assume so that the CG is maximized is examined. Since this output would originally be fed with a high frequency signal, high frequency signals can also propagate through the chip towards the pad. This must be taken into account in the simulation, since the simplest simulation models only give the resistive value independent of the frequency. In reality SMD resistors are used, because shorter leads reduce the inductive parasitic component. As can be seen in Fig. 3.19, there is still an inductive component L_s remaining, which is mainly determined by the trimming. The metallic terminations in interaction with the ceramic dielectrics form the serial capacitor C_s. These two values together with the desired resistance R compose the impedance Z of the unsoldered resistor. If the resistor is soldered, the inductances L_c due to the connection and the two parasitic capacitances C_p formed by the pads of the footprint with the underlying ground plane are added. To account for these effects, but to keep the complexity of the simulation low, only the impedance of the unsoldered resistor is simulated, with parameters chosen larger than would be expected from the unsoldered component. For the parasitic components, the value is changed between $1 \cdot 10^{-4}$ and 10 nH respectively pF. The resistance value is swept between 10 Ω and 1 MΩ. The associated simulation flow can be found in Fig. 3.20. [11, p.1]

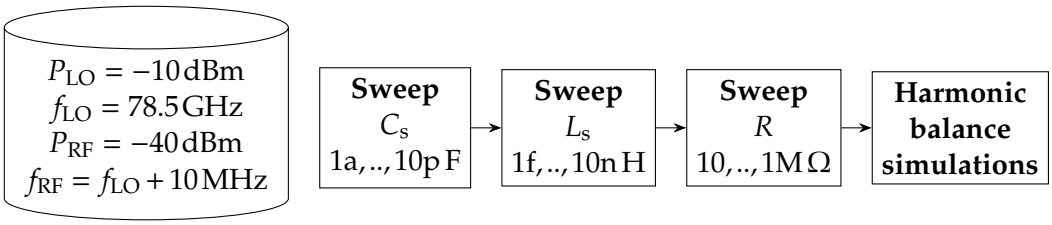

Figure 3.20: The flowchart shows the simulation procedure to consider the effects of the parasitic effects of the load resistance.

The result of the simulation is that with higher resistance value the CG increases as well. For a value of 500 Ω, the improvement is about 0.35 dB compared to a 50 Ω resistor (determined for $C_s = 0.01\,nF$ and $L_s = 0.1\,nH$). No relevant sensitivity to parasitic components was observed. The use of a normal (thick-film) resistor is still not possible because the parasitic components become relevant for higher frequencies and the ratio of $|Z|/R$ deviates strongly from the ideal value $|Z|/R = 1$. In this case, either the capacitive component ($|Z|/R < 1$) or the inductive component ($|Z|/R > 1$) predominates. For this reason, there are special RF resistors which try to counteract occurring effects such as the skin effect by using thin-film technology. From this point on, attention must also be paid to the footprint and the PCB substrate used in order to influence L_c and L_p accordingly. [2] [8] [12]

Nearly all resistors are geometrically too high to bond directly to the RF pad, so the selected resistor is placed at the end of a GCPW. This setup can be explained by the transmission line impedance equation

$$Z_{in} = Z_{line}\frac{Z_{load} + jZ_{line}\tan(\beta l)}{Z_{line} + jZ_{load}\tan(\beta l)} \tag{3.14}$$

under the assumption of a lossless line. The characteristic impedance of the transmission line is denoted as Z_{line}, the impedance of the load by Z_{load} and the wave number by $\beta = 2\pi/\lambda$. For a mismatch, which automatically results from $Z_{line} \neq Z_{load}$, different voltage amplitudes occur on the line. Accordingly, the result of the equation is that the connected impedance Z_{load} is not present at the beginning of the line. Furthermore, the expected bandwidth of the system, from 71 GHz to 86 GHz also results in significantly different wavelengths, which have values from $\lambda = c_0/(\sqrt{\epsilon_{eff}}f) = 2.92\,mm$ to 2.41 mm (values determined for an effective permittivity of $\epsilon_{eff} = 2.1$). [51, pp.56-59]

Due to the described effects and the only minor improvement of the CG, the termination by a resistor is omitted in the first place. In other words, the output termination is an open. Nevertheless, the corresponding option is provided on the printed circuit board.

3.4.3 Pre-measurements

Preliminary measurements are used to verify the simulation results. The measurement setup for characterizing the transconductance mixer is shown in Fig. 3.21. The assembly is done by individual modules, which are connected by means of waveguides.

In the first step, the characteristic curves (output power and bandwidth) of the two frequency

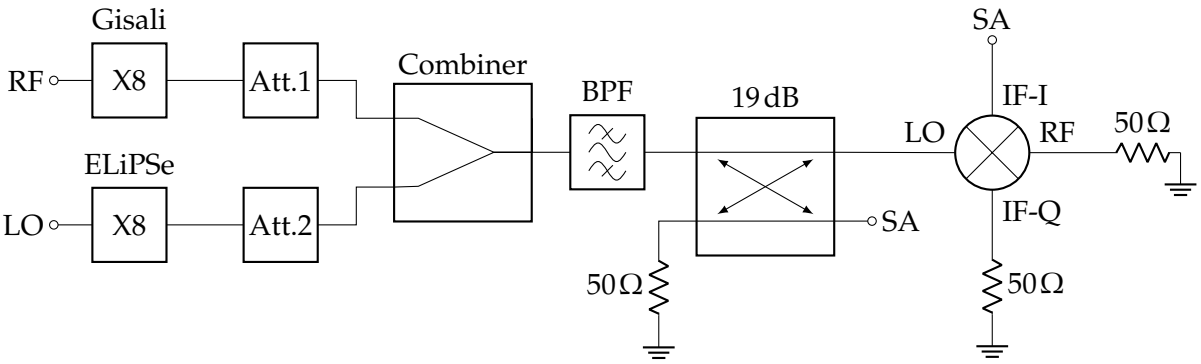

Figure 3.21: The circuit shows the mixer in transconductance configuration. Biasing is not shown and "SA" denotes the spectrum analyzers used.

multipliers are recorded. Since the goal of the preliminary measurement is to characterize the three mixer topologies, the RF input power, which is applied at the mixer, must be known. In order to generate the LO and RF signal, two multipliers are used in the experimental setup, whose output power can be reduced by one attenuator each. In order to determine the output power, on the one hand, the chain consisting of one multiplier, a attenuator, a combiner, a bandpass filter and a coupler (one input port terminated) is measured, and on the other hand, the last component, the coupler, also allows the power to be determined even during the actual measurement since a small part of the power is decoupled. This decoupled power is then fed to the spectrum analyzer extension module from Virginia Diodes, Inc. This module is required because the spectrum analyzer itself cannot measure signals in this frequency range. In addition, the signals to be measured are transmitted through waveguides. The RF power at the input of the mixer can be varied between −50 dBm and −1 dBm by the variable attenuator *Att.1*. The frequency range extends from 74 GHz to 83 GHz and the LO power at the mixer can be adjusted between −25 dBm and −10 dBm.

The next step is to operate the mixer in the resistive mixer configuration as it was actually designed to obtain reference data. In this case, only the RF signal is applied to the RF input of the mixer and the LO signal is connected to the LO port. During the measurements one of the two IF Ports is terminated with 50 Ω to minimize reflections. Similarly, one input of the coupler is terminated. The gate voltage cannot be influenced, because it is generated within the module by the external voltage, which is much higher. The results of the measurements are later compared with the other configurations in Fig. 3.22. The conversion gain is determined at $P_{\mathrm{RF}} = -24.7\,\mathrm{dBm}$, $f_{\mathrm{LO}} = 73.5\,\mathrm{GHz}$ and $f_{\mathrm{RF}} = f_{\mathrm{RF}} + 150\,\mathrm{kHz}$. As expected, this is $G_{\mathrm{C}} = -14.6\,\mathrm{dBm}$ for a LO power of $P_{\mathrm{LO}} = 10\,\mathrm{dBm}$ and $G_{\mathrm{C}} = -19.9\,\mathrm{dBm}$ for $P_{\mathrm{LO}} = -4.1\,\mathrm{dBm}$.

In the next step, both multipliers with their attenuator, the initial RF chain and LO chain, were connected through the combiner and connected together to the RF input of the mixer. The original LO input of the mixer is terminated. This type of configuration corresponds to the self-mixing operation. At the IF output of the mixer, the power of the downmixed signal is now $P_{\mathrm{IF}} = -46.5\,\mathrm{dBm}$, which corresponds to a conversion gain of $G_{\mathrm{C}} = -21.8\,\mathrm{dB}$. This is equivalent to only a small decrease, as was also found in the simulations.

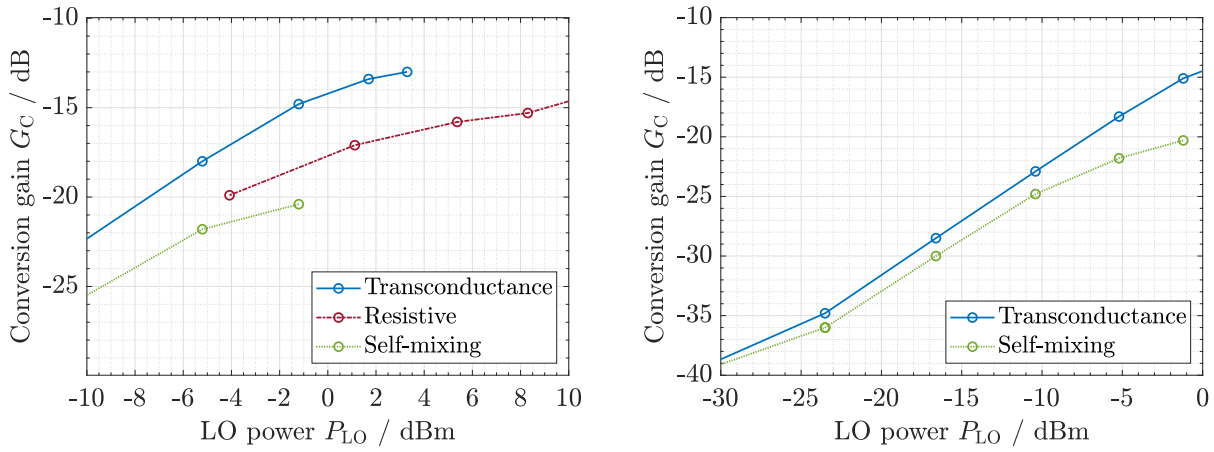

(a) $P_{RF} = -24.7\,\text{dBm}$ **(b)** $P_{RF} = -40\,\text{dBm}$

Figure 3.22: Measurement results are shown for two LO power sweeps where in a) a RF power of $P_{RF} = -24.7\,\text{dBm}$ was applied, which in b) is $P_{RF} = -40\,\text{dBm}$.

The last configuration that was measured is the transconductance mixer. In this configuration both multipliers with their attenuator were connected through the combiner and connected together to the LO input of the mixer. In other words, the LO and RF port have been swapped. The original RF input of the mixer is terminated with 50 Ω. Since biasing is required via the mixer's IF outputs, these were not fed directly to the spectrum analyzer as shown in the block diagram, but each via a bias tee. The latter restricts the IF frequency range to frequencies above 10 MHz. The conversion gain improves to $G_C = -18\,\text{dB}$ in the previous example, but using $f_{IF} = 10\,\text{MHz}$. The reason for the small improvement as in the simulation is the non-variable gate voltage, which would have had to be adjusted to reach the ideal operating point and the non-ideal termination of the RF port with 50 Ω. According to subchapter 3.4.2.2 this should be higher impedance to improve the CG, but such a kind of impedance is unusual in a waveguide system and therefore not present. The symmetrical behavior of the mixer could be confirmed by measuring at the IF-I port instead of the IF-Q port. A positive deviation from the conversion gain of 1.3 dB occurs, which is maintained even during the variation of the LO power.

The preliminary measurements show the expected results. Adjusting the power, frequency and bias voltage values in the simulation gives results that correlate with the measurements. The transconductance mixer has a higher CG than the other two mixer types for the same LO power. From the curve shown in Fig. 3.22b, it can be seen that a certain LO input power is necessary to achieve an improvement in CG over the self-mixing mixer. However, the CG does not fall below that of the self-mixing mixer even at low LO powers.

3.4.4 Comparison

In order to find the mixer that fits the radar system best, the most important characteristics were simulated. The results can be found in Table 3.3 and excerpts thereof in Figs. 3.23a and 3.23b. As

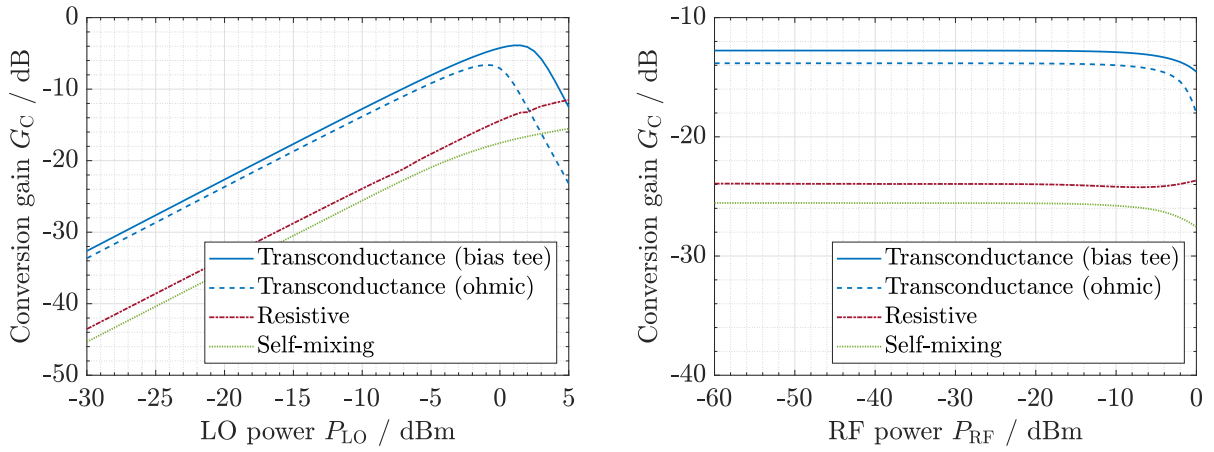

(a) LO power sweep

(b) RF power sweep

Figure 3.23: The simulation results for the resistive mixer, self-mixing mixer and both transconductance mixers are shown for a LO and RF power sweep in a) and b).

Table 3.3: Comparison of the four mixers presented.

Value	Unit	Resistive	Self-mixing	Transconductance	
				Bias tee	Resistive bias
Conversion gain	dB	−23.9	−25.6	−12.8	−13.8
max. IF freq.	GHz	6	4	0.16	3.2
LO bandwidth	GHz	62-85.5	75-82 [*1]	66-76.5	66-76.5
1 dB-CP (RF linearity)	dBm	8.5	−3	−1.5	−14.9
1 dB-CP (LO linearity)	dBm	1.5	−2	−2.5	−3.0
LO to-IF isolation	dB	−29.3	−14.8	−13.2	−11.8
RF return loss	dB	−13.2	−14.9	−18.2	−18.2
IF return loss	dB	−8.4	−10.9	−3.3	−4.6
Max. supply voltage	V	−0.17	−0.35	1.4	3.17
Power consumption	mW	$0.36 \cdot 10^{-3}$	$1.4 \cdot 10^{-3}$	19.3	43.6

[*1] CG decreases from −23.0 dB at 71 GHz to −23.5 dB at 86 GHz

input signal $f_{LO} = 78.5\,\text{GHz}$ with an input power of $P_{LO} = -10\,\text{dBm}$ and $f_{RF} = f_{LO} + 1\,\text{MHz}$ with an input power of $P_{RF} = -40\,\text{dBm}$ were assumed by default. The figures are based on the expected values. In addition, the table list the characteristics of the resistive mixer without self-mixing circuitry as a reference value. The decrease in conversion gain by 1 dB of either the Q or I port is used as the threshold, depending on which decreases faster.

As can be seen, the transconductance mixer with bias tee has the highest CG for the given values. However, for higher IF frequencies, this decreases. This is due to the bias tee, which is effective only up to 345 MHz. However, the frequency range above this is not important for the application because, as already described in equation 2.1, the IF frequency is composed of the steepness of the chirp and the relative distance between the two objects, which were taken into account in the dimensioning of the bias tee. Therefore, the large increase in CG and the halving of power

consumption are more significant. In addition, neither of the two possible types of mixers allows the phase to be evaluated anymore.

3.5 Antennas

The most important components besides the MMICs are the antennas. These are integrated into the PCB and are directly connected to the amplifier chips. The use of a horn antenna is not only suitable for these reasons, but also due to the fact that they have a good directivity, often a gain and a high bandwidth. All of the mentioned points not only belong to the characteristical data of antennas, but are advantageous in a radar system. The directional pattern enables the targeting of objects, the gain allows the detection of more distant objects, and the bandwidth provides higher range resolution.

Two integrated horn antennas designed and simulated by Moritz Vischer are used as antennas. Both transmitting and receiving antennas are identical since the requirements regarding the mentioned points do not differ. They have an additional resonator at the PCB edge to improve the transition into the free space. The antenna is fed via a direct bond from the chip to the feed structure. This is followed by a substrate-integrated waveguide (SIW), which finally merges into a horn antenna. In the following, important structures will be examined based on the provided layout. Since the substrate plays an important role in the design, the most important characteristics should be mentioned first.

The used substrate material is a ceramic-filled polytetrafluoroethylene (PTFE) composite called RO3003, which is manufactured by Rogers Corporation. This material is specifically designed for high frequency applications and offers good electrical and mechanical properties. The thickness is $500\,\mu m$ and the dielectric constant is $\epsilon_r = 3$. The copper thickness used is $35\,\mu m$. [54]

Typically, traces are used to carry signals on a PCB. However, these have higher losses compared to SIWs. The latter have very similar properties to the well-known metal waveguides. These include a high Q-factor (low losses), usability at high powers, and intrinsic shielding from external electro-magnetic fields. In addition, the use of SIWs offers the advantage that without further transition the antenna can be connected, which uses therefore the same substrate. In order not to degrade the efficiency of the antenna, it is important that no unwanted wave propagation (surface wave) penetrates the waveguide or the antenna structure itself. Wave propagation is reduced by constructing the SIW and antenna with continuous copper surfaces above and below, and ideally using metallic sidewalls, which in reality are a via-fences on both sides. The structure of an SIW is shown in Fig. 3.24. [33, p.1585-1589]

In the described waveguide, the wave propagates exclusively as a single mode in quasi-TE10 wave, whose cutoff frequency depends only on the width of the waveguide (distance from via to via), as long as this is greater than the height. A propagation of the transverse magnetic (TM) wave is not possible, because the walls are not continuous and therefore a corresponding current cannot flow.

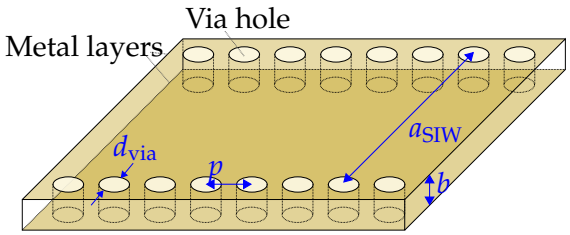

Figure 3.24: Dimensions of the substrate-integrated waveguide.

The equation for the cut-off frequencies of the propagating modes in a waveguide are

$$f_{\text{c,mn}} = \frac{1}{2\pi\sqrt{\mu\epsilon}}\sqrt{\left(\frac{m\pi}{a}\right)^2+\left(\frac{n\pi}{b}\right)^2}. \tag{3.15}$$

Where m and n describe the TM and transverse electric (TE) modes, a and b the long and short edges of the waveguide, μ the permeability and ϵ the permittivity of the material within the waveguide. By assuming $a > b$, the mode with the lowest cut-off frequency is the TE10 mode with $m = 1$ and $n = 0$. Below this frequency, no wave propagation is possible within the waveguide. Assuming that the substrate used has a permeability of $\mu = \mu_0\mu_\text{r} = \mu_0$ and a permittivity of $\epsilon = \epsilon_0\epsilon_\text{r}$, the formula can be simplified to

$$f_{\text{c,TE10}} = \frac{c_0}{2a_{\text{TE10}}\sqrt{\epsilon_\text{r}}} \tag{3.16}$$

using the definition of the speed of light $c_0 = 1/\sqrt{\epsilon_0\mu_0}$. [51, p.113]

The distance between the two fences is not the same as the distance from vertical interconnect access (via) to via, because they do not form an ideal wall. But there are empirically determined equations which compensate for this behavior. For the TE10 mode, if the distance between the nearby vias of a row p is sufficiently small, the following applies

$$a_{\text{TE10}} = a_{\text{SIW}} - \frac{d_{\text{via}}^2}{0.95p}. \tag{3.17}$$

In the case where the ratio between the distance of the two via fences a_{SIW} and the already introduced via-via distance p is $p/a_{\text{SIW}} > 5$ and, moreover, $p/d_{\text{via}} < 3$, i.e., the copper-copper distance between adjacent vias (where d_{via} is the diameter of the vias) is very small, a more accurate approximation can be determined

$$a_{\text{TE10}} = a_{\text{SIW}} - 1.08\frac{d_{\text{via}}^2}{p} + 0.1\frac{d_{\text{via}}^2}{a_{\text{SIW}}} \approx 1.53\,\text{mm}. \tag{3.18}$$

Thus, for the cut-off frequency, we get

$$f_{\text{c,TE10}} \approx 56.7\,\text{GHz} \tag{3.19}$$

This also satisfies the conditions for the design of the subsequent horn antenna, which requires a width such that $\lambda_0/(2\sqrt{\epsilon_\text{r}}) < a < \lambda_0/\sqrt{\epsilon_\text{r}}$ holds and the substrate height does not exceed a_{TE10} [35, p.1924]. [62, p.68]

For the next propagating mode with the designation TE20 we get

$$a_{\mathrm{TE20}} = a_{\mathrm{SIW}} - \frac{d_{\mathrm{via}}^2}{1.1p} - \frac{d_{\mathrm{via}}^3}{6.6p^2} \tag{3.20}$$

and the cut-off frequency

$$f_{\mathrm{c,TE20}} = \frac{c_0}{a_{\mathrm{TE20}}\sqrt{\epsilon_{\mathrm{r}}}} \approx 112.6\,\mathrm{GHz}. \tag{3.21}$$

The possible operating range of the SIW is thus given by $f_{\mathrm{c},10}$ and $f_{\mathrm{c},20}$, each with some margin to account for formula and manufacturing inaccuracies. But, in doing so, a new propagating mode does not necessarily limit single mode operation, instead, dielectric losses, losses in the conductor, or due to insufficiently tight placement of the limiting vias can also become so high before the next possible mode is reached that wave propagation is subject to severe losses. In order to reduce return and leakage losses, vias should be placed such that $d_{\mathrm{via}} < \lambda_{\mathrm{g}}/5$ and $p \leq 2d_{\mathrm{via}}$ are satisfied. Here λ_{g} denotes the guided wavelength in the substrate. [28, p.334]

This can be calculated by

$$\lambda_{\mathrm{g}} = \frac{2\pi}{\sqrt{\left(\frac{\epsilon_{\mathrm{r}}\omega^2}{c_0^2}\right) - \left(\frac{\pi}{a_{\mathrm{TE10}}}\right)^2}} = \frac{2\pi}{\sqrt{\left(\frac{\epsilon_{\mathrm{r}}(2\pi f)^2}{c_0^2}\right) - \left(\frac{\pi}{a_{\mathrm{TE10}}}\right)^2}} \tag{3.22}$$

given in [53]. For a frequency of $f = 86\,\mathrm{GHz}$ one gets $\lambda_{\mathrm{g}} = 2.68\,\mathrm{mm}$.

Furthermore, the characteristic impedance (power-voltage-definition) of the SIW

$$Z_{\mathrm{SIW}} = \frac{VV^*}{2P_{\mathrm{t}}} = \frac{2h}{a_{\mathrm{TE10}}} Z_{\mathrm{TE}} = \frac{2h}{a_{\mathrm{TE10}}} \frac{Z_0}{\sqrt{\epsilon_{\mathrm{r}}}} \left[1 - \left(\frac{f_{\mathrm{c,TE10}}}{f}\right)^2\right]^{-\frac{1}{2}}. \tag{3.23}$$

can be determined from the known and determined parameters. The SIW used here has a characteristic impedance of $Z_{\mathrm{SIW}} \approx 205.7\,\Omega$ at a frequency of 78.5 GHz. The antenna serves as a link between free space impedance and Z_{SIW}. [31, p.1597][38, <B.22>]

In order to keep losses caused by the impedance change from chip or bonding wire to the SIW structure as low as possible and to excite the wave in the waveguide, an appropriate transition is necessary. In each case, impedance matching should be available and the field distribution must match the subsequent structure. A coplanar waveguide (CPW) is used as feed structure and shown in Fig. 3.25a. This has a length of 700 µm, a width of 400 µm. A substrate with a thickness of 500 µm, a of $\epsilon_{\mathrm{r}} = 3$ at a frequency of about 76 GHz and thus acts as a $\lambda/4$ transformer. The impedance of this CPW with ground plane is calculated by

$$Z_0 = \frac{60\pi}{\sqrt{\epsilon_{\mathrm{eff}}}} \frac{1}{\frac{K(k)}{K(k')} + \frac{K(k_1)}{K(k_1')}} \approx 65\,\Omega \tag{3.24}$$

where $K(.)$ is the complete elliptic integral of the first kind with variables k, k_1, k', k_1', which involve geometrically relations. Since the field propagates not only in the substrate, the dielectric constant

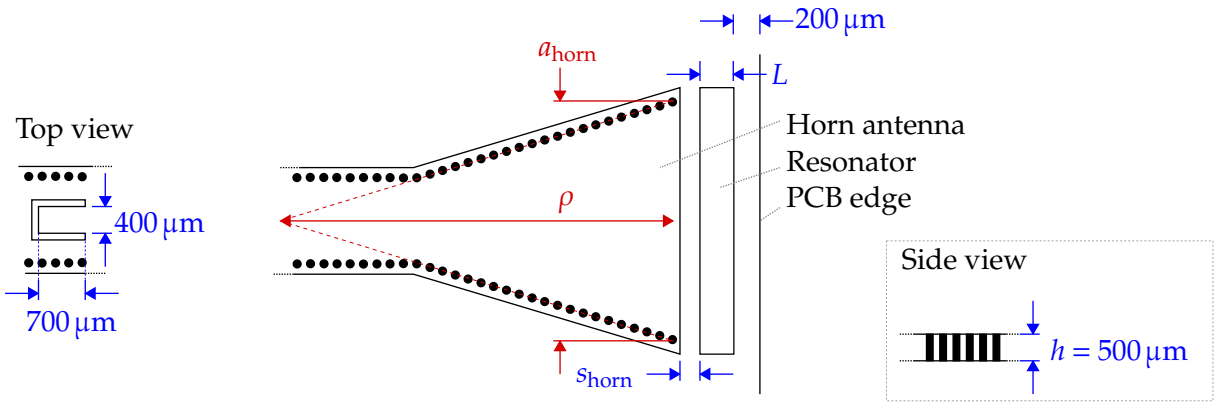

(a) Feed structure **(b)** Horn antenna and resonator

Figure 3.25: Dimensions of the horn antenna and feed structure.

of the substrate cannot be used, but an effective relative permittivity of $\epsilon_{eff} \approx 2.06$. This type of structure is also known as a U-slot patch antenna [47]. Where the antenna feed corresponds to the bond wire. [57, p.79-80]

The antennas used are horn antennas, which emerge directly from the SIWs, as can be seen in Fig. 3.25b, while the height remains constant. Moreover, the designed H-plane SIW horn antenna has the main beam direction in the direction of the z-axis (PCB edge). The equations for dimensioning are the same as for a normal horn antenna. The long edge of the antenna aperture is chosen so that $a_{horn} = 8.7\,mm = 4\lambda_g$ for a frequency of $f \approx 80\,GHz$, which corresponds approximately to center frequency. For good directivity, the length of the antenna is $\rho \approx {a_{horn}}^2/(3\lambda_g)$ [37, <10.16>]. The designed antenna has a length of $\rho \approx 11.4\,mm$, thus satisfying the equation. The structure was also optimized in the CST Studio Suite 3D EM simulation and analysis software.

The thinner the substrate used, the lower the radiation of the antenna. If the substrate thickness is much smaller than the wavelength, the mismatch between the antenna and the surrounding air becomes larger and larger, resulting in low bandwidth. The substrate thickness used is $h = 500\,\mu m$ and the largest wavelength is $\lambda_0 = 4.23\,mm$, so consideration of the transition is necessary. There are several ways to improve the performance of the antenna. On the one hand, a lens can be mounted in front of the aperture, which has the same dielectric constant as the substrate used in the antenna. The lens reduces the mainlobe width and thus increases the front-to-back ratio. The use of lenses is only possible for thick substrates, the focusing effect decreases with thinner substrates, so according to Chen $h > \lambda_0/6$ should apply. On the other hand, placing copper structures on the side of the antenna aperture can improve the reflection coefficient. The radiation of a horn antenna can be seen as a radiating slot in infinite ground plane. Therefore, the front-to-back-ratio would be close to unity. Due to the transition, it is no longer the horn itself that radiates, but the open-ended termination of the two parallel plates after the antenna, which is why diffraction effects change the radiation characteristics of the antenna. [31, p.1601-1607]

While the use of a lens requires additional space and also needs to be aligned and mounted after

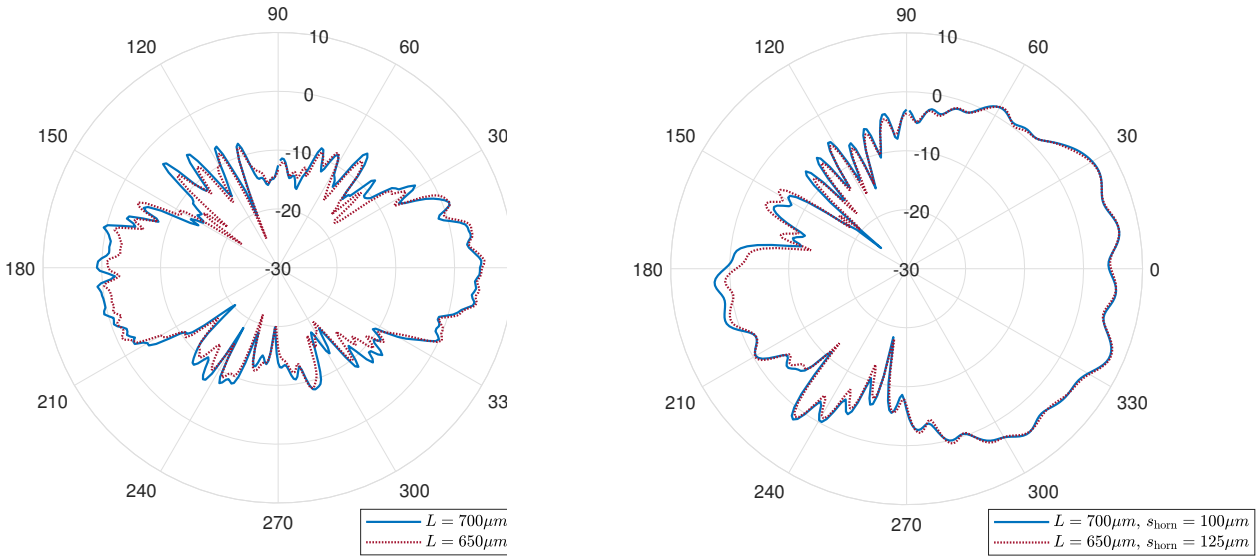

(a) Horiontal **(b)** Vertical

Figure 3.26: Representation of the gain in radiation patterns of the antenna for a frequency of 75 GHz and with mainlobe orientation in 0° direction .

production, the use of etched copper structures can play its advantages. In addition, with the substrate used, the thickness is too small to expect positive results from a lens. The use of two rectangular copper surfaces, one on the top layer and one on the second layer, on which the bottom of the antenna is also located, mitigates the transition into the air (with a $\epsilon_r \approx 1$). The structure resonates at a frequency of

$$f_{\mathrm{res}} = \frac{c_0}{2L_{\mathrm{eq}}\sqrt{\epsilon_r}} = \frac{c_0}{2L(1+0.7h/L)\sqrt{\epsilon_r}} \tag{3.25}$$

where L_{eq} is the equivalent length obtained considering the fringing fields. Whereas L is the geometric length, which in the case of the designed antenna is $L = 700\,\mu\mathrm{m}$, corresponding to a resonant frequency of $f_{\mathrm{res}} \approx 82.5\,\mathrm{GHz}$. In addition to the structure used, there is also the possibility of placing several of these resonators in series, which not only shifts the resonant frequency downward, but also introduces another resonant frequency that appears to be shifted upward despite having the same geometric structure. The frequency shifts result from an occurring capacitance, which can be explained by the nearby plates and their charges on them. However, the electromagnetic simulations of Moritz Vischer showed only a small effect in this case, so multiple structures were omitted. In addition, the radiation losses also increase with rising structure number. [35]

The final results are shown as a field pattern for the elevation and the azimuth angle in Fig. 3.26. The described resonator structure with $L = 700\,\mu\mathrm{m}$ and $s =_{\mathrm{horn}}= 100\,\mu\mathrm{m}$ was used. The antenna gain is at least 3.8 dBi and the half-power beamwidth in horizontal direction is 28° and in vertical direction 25.6° for 75 GHz. However, the antenna pattern also shows that the region of high gain for the vertical direction extends over a much wider range, about 90°. Further values can be found in subchapter 4.3.1, in which the influences of manufacturing are examined.

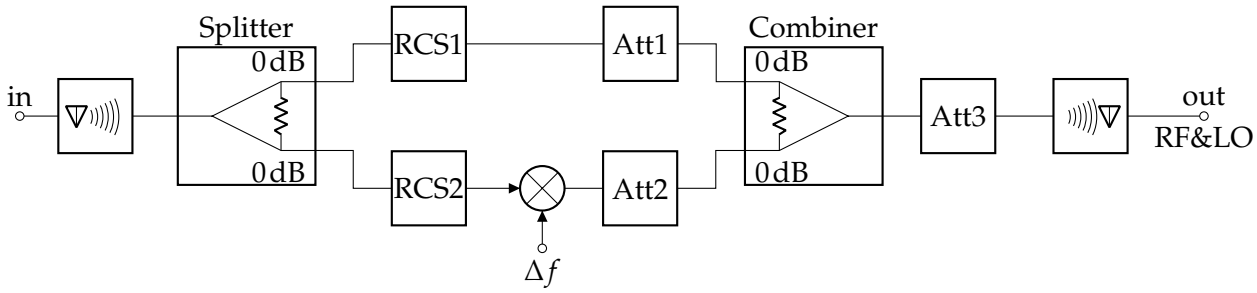

Figure 3.27: The circuit shows the designed propagation model.

3.6 Target modeling

One essential part of the radar system is the propagation in the medium and the occuring reflection. Especially with a self-mixing radar, the received power must be within a certain range for the system to work. For this reason, the implementation in ADS will now be described.

3.6.1 Propagation modeling

If you deal with the propagation of the signal, you have to consider different points as shown in the basics (2.2 and 2.4). In order not to make the system too complex, further reflections are not modeled. Likewise, modeling in the time domain will not be discussed here since the focus is on the design of the system, which takes place in the power domain. The goal is to create a circuit block in which the RCS of the LO, the RF signal and the distance to the first reflection object must be given. Another parameter is the frequency shift, which results from the further reflection and thus a difference in propagation time. This can be calculated either by the slope of the chirp pulse and the distance between the objects (see equation 2.1) or it can be given directly as frequency. The latter option was preferred for reasons of consistency among the simulation data. The circuit block additionally includes the antenna models, which are included as S-parameter files.

To create the model, the radar equation 2.3 was decomposed into its individual parts and considered with logarithmic values. The equation now is

$$P_\mathrm{r}|_\mathrm{dBm} = P_\mathrm{t}|_\mathrm{dBm} + G_\mathrm{t}|_\mathrm{dBi} + G_\mathrm{r}|_\mathrm{dBi} + 20\log(\lambda|_\mathrm{m}) + \sigma|_{\mathrm{dB(m^2)}} - 30\log(4\pi) - 40\log R|_\mathrm{m} \tag{3.26}$$

and thus shows more clearly what influence the individual parameters have. Especially, it is found that the RCS contributes in the same way as the gain of an antenna or the transmitting power. For this reason, the reflectivity of objects will be simulated in more detail in the next subchapter.

If one goes step by step through the process of wave propagation, the model in Fig. 3.27 is obtained. The Tx antenna is followed by a power splitter which, however, unlike the real passive power divider, does not attenuate the signal (marked by 0 dB). This is necessary to generate the LO and RF path. The LO path contains on the one hand the attenuation or amplification by the reflecting

object in the form of an S-parameter block (RCS1) and on the other hand an attenuator (Att1) which represents the free space attenuation for both propagation directions. In addition to the objects of the LO path, the RF path also contains a mixer that leads to the frequency shift Δf. After both signals are combined again by an ideal power combiner, a further common attenuation (expressed by Att3) takes place, which is due to the necessary conversion within the radar equation from above. Finally, the model of the receiving antenna follows. In case of the LO path, the equations associated with the RCS scattering parameter (S-parameter) block is $S(2,1) = 10^{RCS1/20}$ and for the attenuator the equation is $\text{Att1} = 2 \cdot 10\log(\lambda_{\text{LO}}) = 20\log(c_0/f_{\text{LO}})$. While the calculation of the RCS for the RF path is identical, the equation of the attenuation must be adjusted because the frequency changes between outward and return: $\text{Att2} = 10\log(\lambda_{\text{LO}}) + 10\log(\lambda_{\text{RF}}) = 10\log(c_0/f_{\text{LO}}) + 10\log(c_0/f_{\text{RF}})$. As mentioned a third attenuation block is required with $\text{Att3} = 40\log(R) + 30\log(4\pi)$ to correct the value transformation and to include the distance R.

3.6.2 Radar cross section simulation

As can be seen from the radar equation or directly from the propagation model shown previously, the RCS has a direct influence on the reflected signal. While mainly in military applications the RCS should be as small as possible to avoid detection by an enemy radar system, there are applications like calibration of antennas or marking of relevant objects, where an angular reflector is used to obtain the highest possible RCS. However, in most cases, such as automotive use, but also in level determination, the reflective object is not designed to have the highest possible RCS. But this practice-oriented RCS σ of an object is more difficult to determine, unlike most other parameters in equation 2.3. This is because the RCS depends on the size of the object, location, transmission frequency, material and electrical properties of the surface of the object. Only the power that arrives at the reflecting object can be reflected (in many directions). The corresponding power balance equation is

$$\frac{\sigma S_{\text{Tx}}}{4\pi} = S_{\text{Rx}} r^2 \tag{3.27}$$

with the power density S_{Tx} of the transmitter at the radar target in W/m^2 and the scattered power density S_{Rx} at distance $r = R$ to the receiver, for example. The power in watts received and re-radiated by the radar target can be calculated by σS_{Tx}. If the equation 3.27 is transformed the RCS

$$\sigma = 4\pi R^2 \frac{S_{\text{Rx}}}{S_{\text{Tx}}} \tag{3.28}$$

can be calculated. This equation gives the retro-reflective area that captures the incoming wave and radiates it isotropically into space. According to this, however, this power density cannot be received in total by the receiver antenna, but only within a solid angle Ω which decreases with distance squared: $\Omega = A_{\text{Rx}}/r^2$. The power density at the Rx antenna is than $S_{\text{Rx}} A_{\text{Rx}}/\Omega = S_{\text{Rx}} r^2$.

For simple objects, the formulas given in Table 3.4 for calculating the RCS can be found in the literature [60]. However, these are only valid for objects which do not have a frequency-dependent reflection, are much further away than the wavelength ($\lambda = c_0/f = 3 \cdot 10^8\,\text{m/s}/71\,\text{GHz} = 3.5\,\text{mm}$)

and are also much larger than it.

Table 3.4: Listed are formulas for the calculation of the RCS for simple objects made out of perfect electric conductor (PEC).

Shape	RCS σ / m^2
Sphere	$\sigma_{max} = \pi R^2$
Cylinder	$\sigma_{max} = 2\pi r h^2/\lambda$
Plate (orthogonal)	$\sigma_{max} = 4\pi b^2 h^2/\lambda^2$
Plate (tilted)	$\sigma_{max} = 0$
Corner reflector	$\sigma_{max} = 12\pi L^4/\lambda^2$

Often the effective reflective area is given in a logarithmic measure. Here, reference is made to a ideally conducting sphere with a cross-section of $1\,m^2$. It should be noted that in the case of a sphere, only a small part of the incident wave is also directly reflected back to the source, so that the calculated RCS is often numerically larger than the geometric area of the object under investigation. For example, a small piece of flat metal is sufficient to produce the same reflection as the sphere used for comparison. The advantage of a sphere, however, is that the reflection is independent of the angle of incidence, as shown by the comparison with the two flat metal plates in Table 3.4.

While equations are given for bodies with simple geometries from PEC, field calculations become necessary for modified shapes and especially for different materials. For more complex objects, not only different sub-areas contribute to the effective reflective surface, but constructive and destructive interference may also occur. Further dependencies are the wavelength and the angle of incidence as well as the angle of reflection of the radiation.

The asymptotic solver is intended for very large objects (e.g. $> 1000\lambda$) and uses ray tracing to determine the solution. It is based on the Shooting Bouncing Ray (SBR) method, which is an extension of pyhsical optics and thus includes multiple reflections and edge diffraction. However, the calculation is limited to PEC and vacuum only. [7, pp.4,11]

Similarly, the integral equation solver can be used in the simulation of electrically large structures. The three-dimensional full-wave solver uses the method of moments with a multilevel fast multipole method. A major advantage is that by using the surface integral technique, objects with a large distance between them can be solved efficiently. This is the case for the investigated radar system, since two spatially separated reflection objects are simulated simultaneously. [7, p.4,9-10]

While the first reflection by an object can thus be determined, the transmission, reflection and refraction must be considered for the second object behind it, as described in the fundamentals in subsection 2.4. Therefore, the idea is to calculate the RCS for the first reflection object by the simulation software CST Studio Suite (CST) and than adding a second reflective surface. Through this simulation it is possible to determine what power is present at the input of the receiver. Since the power of the first object is also known, the difference can be used to determine the RCS of the second reflective object.

Expressed in formulas, the first power is obtained by rearranging the radar equation 2.3:

$$P_{\mathrm{r},1} = \frac{P_{\mathrm{t}} G_{\mathrm{t}} G_{\mathrm{r}} \lambda^2 \sigma_1}{(4\pi)^3 R^4}. \tag{3.29}$$

For both objects the power

$$P'_{\mathrm{r},2} = P_{\mathrm{r},1} + P_{\mathrm{r},2} = \frac{P_{\mathrm{t}} G_{\mathrm{t}} G_{\mathrm{r}} \lambda^2 \sigma'_2}{(4\pi)^3 R^4} \tag{3.30}$$

can be determined in the same way. If the equation 3.29 is now substituted into equation 3.30

$$P_{\mathrm{r},2} = P'_{\mathrm{r},2} + P_{\mathrm{r},1} = \frac{P_{\mathrm{t}} G_{\mathrm{t}} G_{\mathrm{r}} \lambda^2 \sigma'_2}{(4\pi)^3 R^4} - \frac{P_{\mathrm{t}} G_{\mathrm{t}} G_{\mathrm{r}} \lambda^2 \sigma_1}{(4\pi)^3 R^4} = \frac{P_{\mathrm{t}} G_{\mathrm{t}} G_{\mathrm{r}} \lambda^2}{(4\pi)^3 R^4} \cdot (\sigma'_2 - \sigma_1) \tag{3.31}$$

the RCS of the second object $\sigma_2 = \sigma'_2 - \sigma_1$ can be obtained.

The simulation of different object configurations was done at 77 GHz, since for this, due to its automotive application, the relative permittivity and permeability values can be found in literature. However, it turns out that the calculation for two reflection objects is very computationally intensive and thus cannot be determined for practical cases. A scaling of the RCS starting from a small object to a larger one of the same kind is not possible, because the reflection of the wave behaves differently. One possibility is therefore, as already described, to use two objects which do not shade each other. This allows both objects to be analyzed separately to a first approximation.

3.7 Simulation of the entire frontend

The individual components presented are put together to check the functioning in the entire chain. For example, the output power, the power of harmonics and mixed products can be investigated. Relevant here is the transmit power, the receive power, the powers at the mixer and of course the IF output power. Likewise, the bandwidth of the system can be investigated by varying the input frequency. Moreover, a corner analysis can be done, where the process parameters, the supply voltages and the temperature are varied. Since the MMICs are already manufactured and, measured values are available for the individual cells and the temperature is not modeled for all components, the corner analysis is limited at this point to the variation of the supply voltages. In the first instance, it can be postulated that all voltages increase or decrease simultaneously since all MMICs are supplied by the same power supply. Typically one assumes 90 %, 100 % and 110 % of the voltage values.

In the following, the described corner analysis over different input frequencies f_{in} is considered. As can be seen from the first diagram in Fig. 3.28a, not the whole power is transferred into the transmitter, or more precisely the multiplier, because there is a mismatch between the power source and the input of the MMIC. However, if we consider the output power of the Tx before the antennas, since these are covered by the propagation model, from 8.5 GHz to 11.2 GHz, which corresponds to a range of 68 GHz to 89.6 GHz, an almost constant power of 19 dBm can be seen.

Also the increase of the supply voltage has its first visible effect. For the entire system, it can be noted that the power values for lower voltages (solid line, 90 %) are also lower than for normal voltage (dashed line) or for increased supply voltage (dotted line, 110 %). In the next figure the power is plotted after the receiver antenna. Here the signal has traveled a distance of 30 cm to the first reflection object. This has a RCS of $\sigma = 0\,\mathrm{dB(m^2)}$ and the second one of $\sigma = -20\,\mathrm{dB(m^2)}$, which is achieved, for example, by a 10 by 10 mm metal plate. Due to the distance of both objects a shift of 10 MHz occurs. Thus, the two received signals differ by 20 dB. The stronger signal in Fig. 3.28c is therefore called LO signal. Since these are very weak, the AMP101 amplifies both of them again to increase the conversion gain and thus produce a stronger mixer output signal, as can be seen in Fig. 3.28e.Due to the larger voltage amplitude it is now acuh evaluable by a ADC. The conversion gain plotted in Fig. 3.28f can be calculated from the RF input power and the IF output power. The influence of voltage fluctuations also cannot be neglected at this point, since the conversion gain changes by more than ±2 dB.

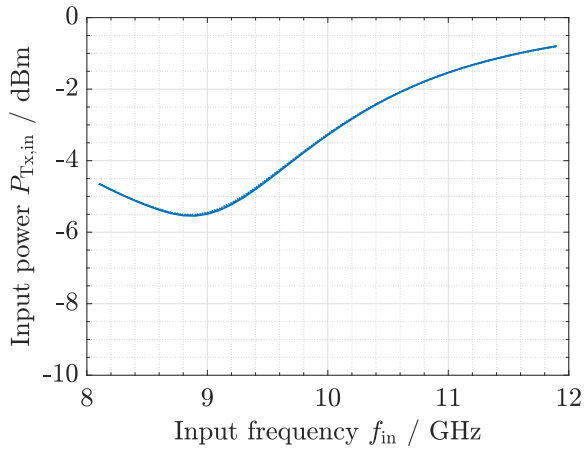

(a) Transmitted power into Tx

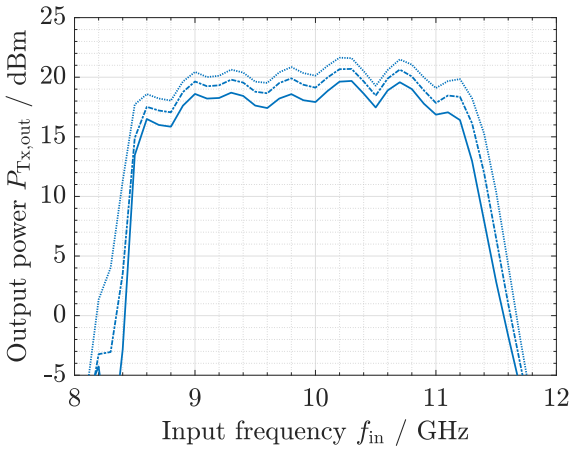

(b) Transmitted power into Tx antenna

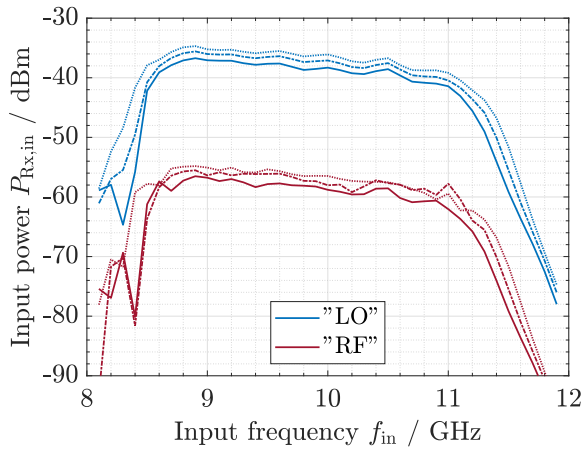

(c) Received power after Rx antenna

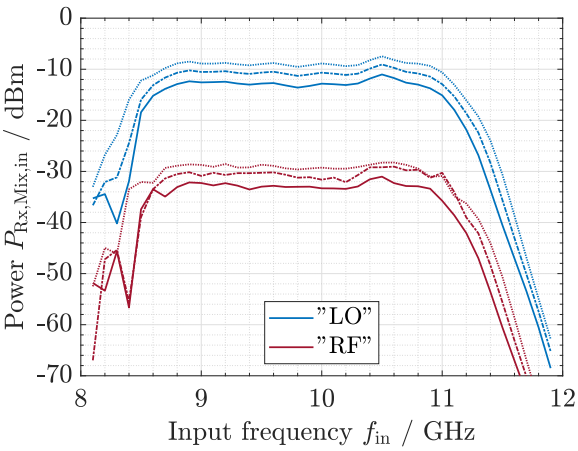

(d) Received signals after Rx antenna

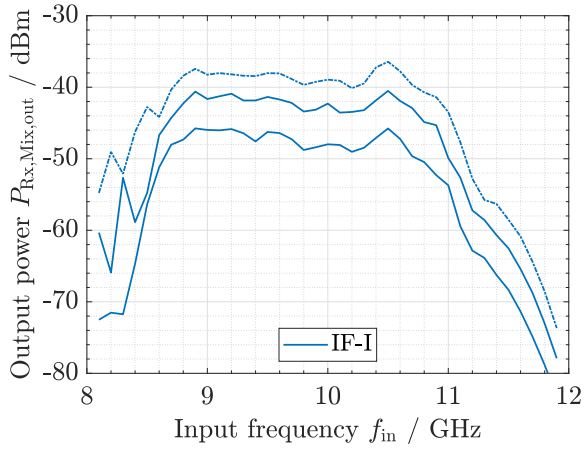

(e) Input powers at the mixer

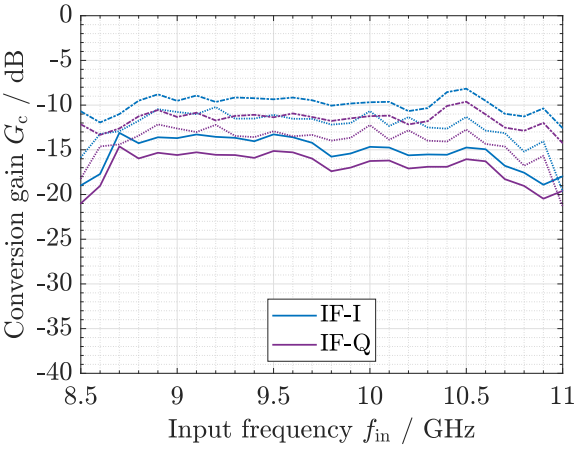

(f) Mixer conversion gain

Figure 3.28: Individual performance values of the entire system are presented in figures a) to e). The conversion gain of the mixer for a variation of the input voltage (solid = 90%, dashed = 100% and dotted = 110% of the nominal voltage) is plotted in f).

4 Practical implementation

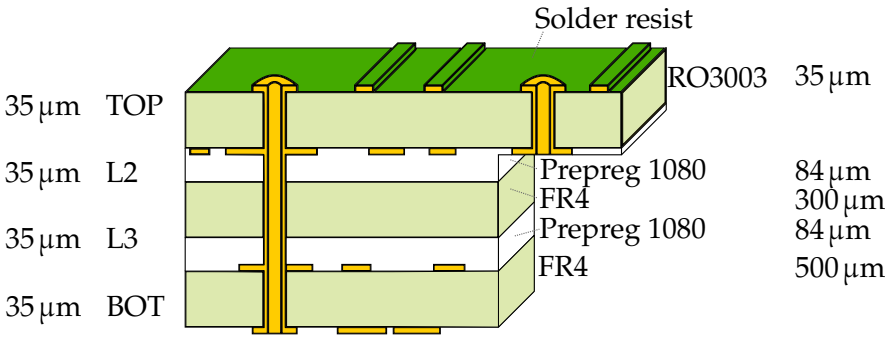

Figure 4.1: Layer stack of the frontend PCB with dimensions.

This chapter describes the process and important factors that must be considered when the circuit simulation becomes reality. Among other things, observed design rules are explained and the selection of components is justified.

4.1 Layer stackup

As mentioned in the previous chapter, the antenna is placed between the copper layer on the top layer and layer 2. Therefore, RO3003, a high-frequency core material from Rogers is used. A symmetrical four-layer structure is chosen to simplify an EMC-compliant design and, above all, to counteract deformations. The according layer stack is illustrated in Fig. 4.1. To maintain symmetry even for the antenna, the lower layers are milled off (Z-axis milling) until the second metal layer is revealed. This is indicated on the right side of the layer stack. If the metal layer is no part of the RF-structures, it is covered with solder resist to simplify soldering and to protect the underlying tracks from environmental influences.

4.2 Design rules and component selection

The design of the printed circuit board has a great influence on the performance of the circuit. In order to obtain results that are as identical as possible to the simulation results, the following points were taken into account.

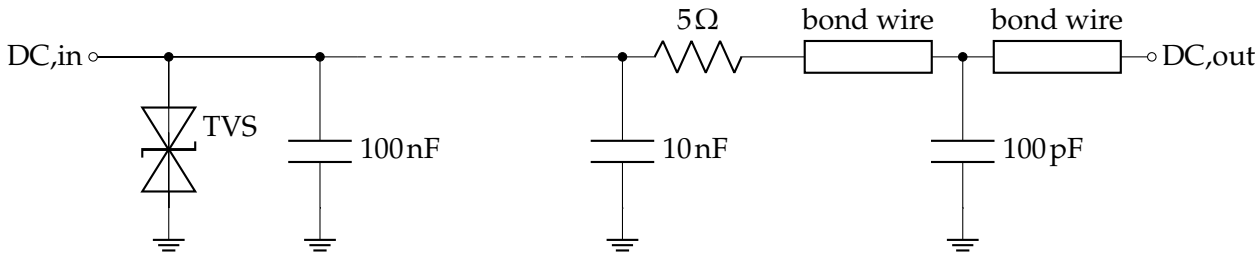

Figure 4.2: The circuit shows the TVS diode, the capacitors, the resistors and the bond wires, that are placed in a DC supply line.

The first point is the stabilization and smoothing of the DC supply voltage by capacitors. For example, in simple switching controllers, the switching frequency is visible in the output signal due to the operating principle. To smooth this supply noise, a 100 nF ceramic capacitor is installed near the connection terminals, which shunts high-frequency signals to ground. Ceramic capacitors are preferred based on their low equivalent series resistance. Since the voltages inside the MMICs must be as constant as possible, because for example the gate is biased and thus the operating point would be shifted in the event of fluctuations, additional capacitors must be used, which filter especially higher frequency signal components on the supply voltages. However, the required smaller capacitance values also mean that the effective radius is reduced, which is why these are placed as close as possible to the chip. For this purpose, 10 nF capacitors are used on the one hand and bondable capacitors on the other, whereby the latter are glued directly to the exposed grounded metal near the chip edge. Wider traces can also be beneficial as they result in higher capacitance loading due to the near and underlying ground planes. To protect the inputs from electrostatic discharge (ESD) of the ICs, for example, bidirectional transient voltage suppressor (TVS) diodes are used. The breakdown voltage of these is selected so that they are close to the expected supply voltages, but do not break down directly in the event of small changes and component variations. They are placed directly after the terminals to protect all other components from overvoltages, as shown in Fig. 4.2. [9, pp.22-23,45]

For all the components mentioned so far and also for all other components, a low-impedance ground connection is mendatory. For this purpose, the used vias must be placed as close as possible to the pads of the individual components. At best two vias are used simultaneously to reduce inductance and resistance. It is also important to keep the impedance of the ground low and to reduce the current return paths. To this end, the signal return plane is connected to the polygons on the top layer via a via stiching. Unbonded copper surfaces should be avoided as they may start to oscillate. Likewise, there should be no copper bars without a via at the end, as these could otherwise act as a dipole. [9, pp.26-28][4] [46, p.234-235]

The supply lines are almost completely surrounded by a grounded copper surface and thus also have a sufficiently large distance to neighboring traces. In addition, a via fence, i.e. a series of densely placed vias (in relation to the suppressing wavelength), prevents the coupling of electromagnetic waves into and out of the substrate. The important signal carrying conductors are

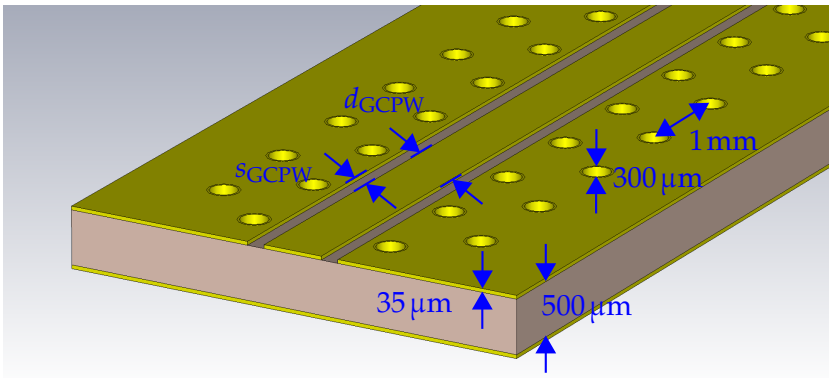

Figure 4.3: Dimensions of the GCPW.

designed as GCPW with a characteristic impedance of $Z_0 = 50\,\Omega$, as shown in Fig. 4.3. The latter is primarily determined by the ground to signal distance s_{GCPW} on the top layer. The simulation in CST confirms a distance of $s_{GCPW} = 125\,\mu m$, a signal conductor width of $d_{GCPW} = 600\,\mu m$, a via diameter of 300 µm and a via spacing of 1 mm from center to center. In order to keep the characteristic impedance as constant as possible, soft bends are used instead of the frequently used 45° angled traces. Due to the fact that the electromagnetic field does not propagate mainly in the substrate towards the ground plane below, as would be the case for a microstrip line, the material above also plays an important role. Therefore, solder resist should not be used on top of the GCPWs because they are calaculated and simulated under the assumption that air is one part of the propagation medium. In contrast to the solder resist layer, that has on the one hand large tolerances in thickness and on the other hand a higher dissipation factor and moisture absorbance, the propagation in air is much more predictable. Especially due to the ground-signal-ground gap of the GCPWs, which would be filled by solder resist, special attention must be paid. However, it should not be ignored that now the metal surface is unprotected from external influences. [32]

But not only the field conducting materials have to be considered, but also the current conducting material. The skin depth for a plane wave can be calculated by $\delta_s = \sqrt{2/(\omega\mu\sigma)} = \sqrt{1/(\pi f\mu\sigma)}$, with the angular frequency $\omega = 2\pi f$, the permeability μ and the electrical conductivity σ of the conducting material. After travelling a distance of one skin depth, the amplitude of the fields in the conductor will decay by $1/e$. For copper, which is used as the conductor material on PCBs, a frequency of 10 GHz results in a skin depth of $\delta_s = 0.66\,\mu m$. In conclusion, the surface finish on the top layer copper without solder resist is relevant for these frequencies. Due to relative high nickel (Ni)-thicknesses of about 7 µm (compared to the skin depth) Ni-containing finishes like the common-known ENIG (electroless nickel/immersion gold) are avoided. In addition, the conductivity is lower compared to copper, which would result in a high insertion loss. The use of electroless palladium/immersion gold (EPIG) as a surface material, which consists of a thin palladium layer with a maximum thickness of 0.2 µm and an overlying gold layer with a maximum thickness of 0.1 µm, is more suitable for high frequency applications. Compared to the use of electroless palladium alone, gold wire bonding is possible and finer structures can be produced. Omitting the Ni-layer also has the advantage of preventing oxidation, which can otherwise only

be avoided by adding an additional barrier layer. [51, p.19][20][50][10]

By using bond wires, which have a serial inductance in the equivalent circuit and the above mentioned 10 nF shunt capacitors, a serial resonant circuit is formed. Ideally, a 5 Ω resistor R_{ser} is used for damping. However, the disadvantage of R_{ser} is that a voltage also drops across it, which is why the supply voltages must be adjusted. In addition, increased power dissipation occurs in resistors placed in traces with higher current flow, which normal resistors in a 0402 package cannot withstand. For this reason, as shown in table 4.1, special resistors are used which either have a higher power dissipation of 200 mW (instead of 63 mW) or, if not otherwise possible, have a lower resistance value. Placing DC blocks between the MMICs to prevent current flow between the chips, which could shift the quiescent point, is not necessary since all chips already have internal series capacitors on the corresponding signal lines. Finally, it should also be noted that the antenna was placed at a distance of 0.2 mm from the board's outer edge according to the simulation, leaving a distance of 6.25 mm from the edge of the board to the casing.

Table 4.1: Supply voltages of each component, and resulting TVS-diode and series resistor R_{ser} selection.

Component	Voltage type	Voltage w/o R_{ser}	Voltage w/ R_{ser}	TVS-diode	R_{ser}
X08004	Gate voltage V_{GG1}	−0.3 V	−0.3 V	2 V	5 Ω
	Gate voltage V_{GG2}	−0.25 V	−0.25 V	2 V	5 Ω
	Drain voltage V_{DD}	1.1 V	1.51 V	2 V	5 Ω
	Gate voltage V_{GG3}	−0.3 V	−0.3 V	2 V	5 Ω
	Gate voltage $V_{AMP,VG}$	0.15 V	0.15 V	2 V	5 Ω
	Drain voltage $V_{AMP,VDS}$	1.4 V	1.82 V	2.5 V	5 Ω
AMP002	Gate voltage V_G	0.1 V	0.1 V	2 V	5 Ω
	Gate voltage V_{G2}	0.9 V	0.9 V	2 V	5 Ω
	Drain voltage $V_{D,CASC}$	2.4 V	2.96 V	3.3 V	5 Ω*
	Gate voltage $V_{G,CS}$	0.15 V	0.15 V	2 V	5 Ω
	Drain voltage $V_{D,CS}$	1.398 V	1.79 V	2.5 V	1 Ω*
AMP101	Gate voltage V_{G2}	1.2 V	1.2 V	2 V	5 Ω
	Drain voltage $V_{D,CASC}$	2 V	2.71 V	3.3 V	5 Ω*
	Gate voltage $V_{G,tune1}$	0.2 V	0.2 V	2 V	5 Ω
	Gate voltage $V_{G,tune2}$	0.2 V	0.2 V	2 V	5 Ω
	Gate voltage $V_{G,CS}$	0.1 V	0.1 V	2 V	5 Ω
	Drain voltage $V_{D,CS}$	1 V	1.7 V	2.5 V	5 Ω*
MFM005	Gate voltage $V_{G,I}$	−0.19 V	−0.19 V	2 V	5 Ω
	Gate voltage $V_{G,Q}$	−0.19 V	−0.19 V	2 V	5 Ω
	Drain voltage $V_{D,I}$	0.94 V	–	2 V	–
	Drain voltage $V_{D,Q}$	0.94 V	–	2 V	–

* Instead of a standard 0201 50 mW-type a high power type with 200 mW (0402) is required.

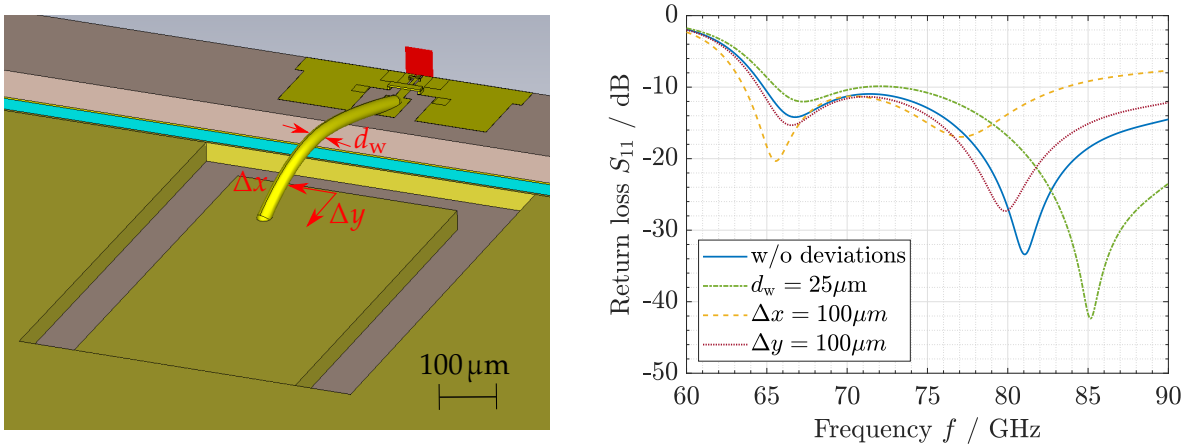

(a) Simulation model **(b)** Simulation results

Figure 4.4: Simulation model for determining the influence of the bond connection. The varied parameters are plotted in a). An extract of the results is shown in b).

4.3 Assembly

The MMICs are bonded to the grounded metal surface using conductive adhesive. This not only eliminates the need for ground connections through bonding wires, but also ensures heat dissipation. The most relevant connections are those to the antennas since that is where the frequency is highest. For this reason, the edges of the amplifier MMICs are aligned along the underlying copper edges. Simulation of this bond, as shown in Fig. 4.4a investigates the dependence of the positioning of the bond on the PCB and the wire diameter d_w versus frequency. The return loss between the signal conductor on the MMIC and SIW is used as a parameter. A central positioning at the edge of the feed structure and the use of a 17.5 µm bonding wire are chosen as starting quantities. The location of the bonding junction is shifted stepwise in x- and y-direction, as shown in the figure. Similarly, the use of the next larger bond wire diameter with 25 µm is considered. Based on the results given in Fig. 4.4b, the best match can be achieved with a centered placement directly at the copper edge and a bond wire diameter of 17.5 µm. Especially a shift in x-direction should be avoided, because this increases the return loss.

As shown above, the symmetrical layer stack contains RO3003 as a core material between top layer and layer 2 as well as a FR4 core between layer 3 and the bottom layer. These materials have different associated thermal expansion coefficients and therefore care must be taken when curing the adhesive in the oven to ensure that the PCB does not bend too much. A consequence of this may be not only damage to the existing structures on the PCB, but also to components and their solder connections. An equally important value to consider is the glass transition temperature for each material used, which indicates the temperature at which the aggregate state of the resin matrix changes from solid to soft. For example, for FR4 this is 150 °C [24, p.1]. [25]

Bonding takes place with ultrasound. A bonding wire with a diameter of 17.5 µm is used for both the RF and DC bonds. The diameter results not only from the simulation, but also from the

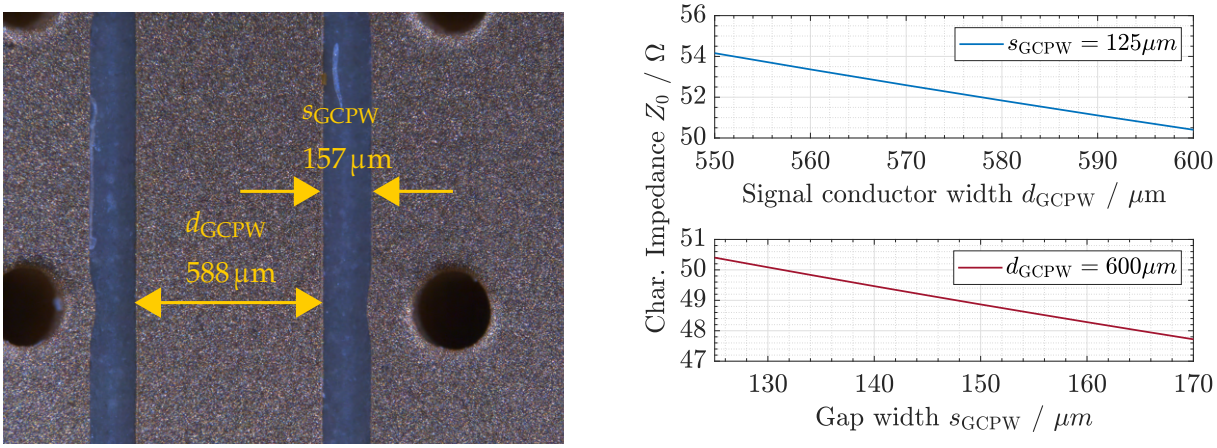

(a) Microscope image

(b) Simulation results

Figure 4.5: Simulation model for determining the influence of the bond connection. The varied parameters are plotted in a). An extract of the results is shown in b).

larger of the pads on the MMICs. The wedge bonding used is advantageous compared to ball bonding due to flatter connections with finer pitch. A low-profile connection is necessary for the IC-to-IC connection. Also, the simulation of the bond connection towards the antenna has shown a significant degradation in the increase of the bond height. A larger arc is associated with a greater inductance and thus degrades the performance. Nevertheless, the wires should not be under tension, because the connection can break when the temperature drops. In addition, the majority of the capillary tool is applied to the surface during ball bonding so that this top metal layer in the bond area can be destroyed. [26] [46, p.234]

4.3.1 Manufacturing tolerances

In order to assess the quality of PCB manufacturing, the most important dimensions were examined under the microscope. This includes the antenna, with its feed and resonator structure, and the GCPW. In both cases, the structures have their characteristic properties due to the copper-copper spacing and the geometric dimensions.

The coplanar waveguide shows a larger distance between signal and ground copper at all locations examined and a narrower signal line in some cases. The measured gap distances are between 169 µm and 121 µm and the minimum diameter of the signal conductor is 566 µm. An example of a measurement is shown in Figure 4.5a. In order to assess the influence of these deviations, a piece of the GCPW was simulated again in CST. The width of the signal conductor d_{CPWG} was varied from 550 µm to 600 µm and the gap width s_{CPWG} from 125 µm to 170 µm. Related results can be found in Fig. 4.5b. The deviation to the desired structure with 600 µm width of signal conductor and 125 µm distance seems to be large at first moment, but the simulation shows almost no difference.

As mentioned at the beginning, a dependence of the antenna performance due to the deviations is expected. For this reason, the resonator structure and its spacing s_{horn} were simulated again, with

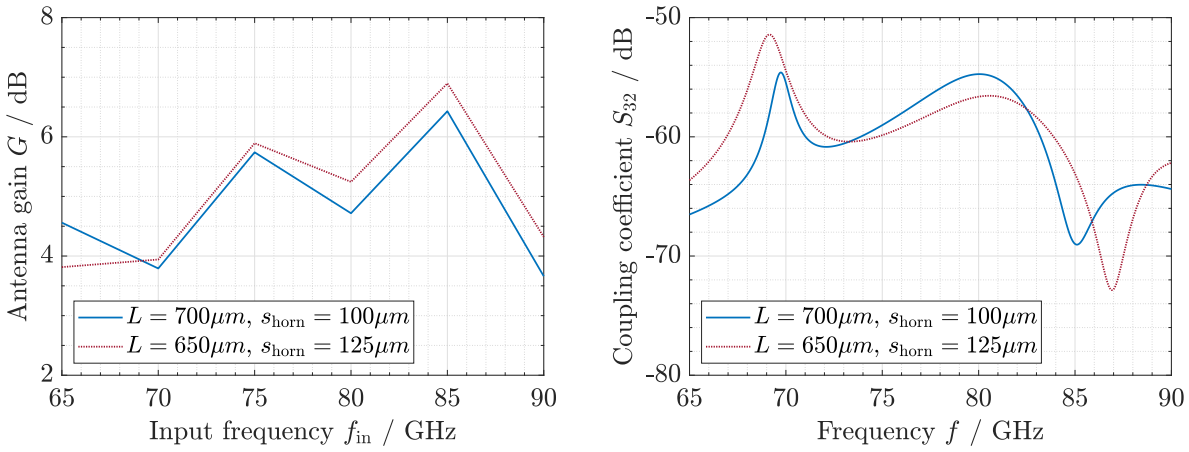

(a) Antenna gain **(b)** Coupling coefficient

Figure 4.6: The simulation results for the gain of the antenna and the coupling between the two are shown in a) and b). Likewise, the curve for originally simulated antenna is plotted.

the measured values. As mentioned at the beginning, a dependence of the antenna performance due to the deviations is expected. For this reason, the resonator structure and its spacing were simulated again, with the measured values. The smallest determinable dimensions here are $L = 656\,\mu\text{m}$ and $s_{\text{horn}} = 124\,\mu\text{m}$, so $L = 650\,\mu\text{m}$ and $s_{\text{horn}} = 125\,\mu\text{m}$ were chosen. The corresponding antenna diagrams can be found in Fig. 3.26. In addition, the maximum antenna gain versus frequency and the coupling between the two antennas were simulated and shown in Figs. 4.6a and 4.6b. In summary, it can be stated that the performance of the antenna has not changed insignificantly due to the tolerances during production. Even if this applies to the coupling coefficient, an attempt should still be made to lower it. The reason for this is that for a transmit power of 20 dBm at the receive antenna −35 dBm are directly coupled in, which either appear as ghost target or act as LO signal after amplification, if this is not produced by a clearly stronger reflection. For this purpose, for example, absorbers can be inserted between the two antennas in the PCB.

Finally, it should be mentioned that the manufacturing tolerances must at least meet the criteria of the IPC. In practice, these are typically exceeded because the manufacturers are interested in performing as well as possible compared to their competitors. Also in the case of the produced PCB, the deviation is only 7 %, although according to the IPC 20 % is allowed. [41, p.11]

4.4 DC supply

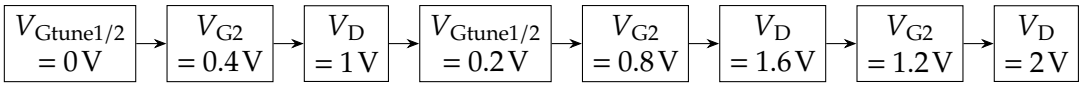

Figure 4.7: The flowchart shows the bias sequence to turn on the casodes of the AMP101.

The power supply is provided via pin headers on the edge of the frontend PCB, thus enabling

simple and reliable connection of a DC power supply PCB. By means of an adapter PCB, the frontend can also be supplied via source measure units (SMUs). Both PCBs can be found in the appendix (Fig. A.1 and A.2) During the design of this, attention was paid to the different voltage ranges and measurement accuracies of the various SMUs [21][22][18]. The use of this type of power supply allows the frontend to be operated with constant control of the voltage and current values. This is necessary to set the operating points of the individual MMICs. For example, the drain current density in the cascodes of the amplifiers should be about 400 mA/mm to achieve the maximum transconductance. The developed adapter PCB also provides for the possibility of connecting individual voltages. This is advantageous for the design of a voltage supply PCB as it reduces the number of voltages to be controlled. However, care must be taken to ensure that the bias startup sequence and also the shutdown sequence are observed. This is necessary to prevent unfavorable voltage and current values. Basically, all voltages should be set to 0 V when switching on so that defined potentials are present at all pins. This is followed by powering up the AMP101, first applying the gate voltage of the cascodes and then applying a low voltage, for example 0.4 V, to the drain. This results in a small drain current. Turning on the cascodes requires observing the maximum drain source voltage $V_{DS} = 1\,V$, the maximum drain current density with 600 mA/mm and the maximum gate current with 1 mA/finger. The sequence shown in Fig. 4.7 is suggested as the power-on sequence. This was determined from a simulation and respects the above points by considering the *I-V* characteristics of the common source and common gate transistors. The voltage V_{VG2} at the gate of the common gate transistor is always higher than that of the common source transistor $V_{Gtune1/2}$ and is increased cycle by cycle together with the drain voltage. After reaching the final voltages and increasing the drain voltage V_D, the mixer is switched on. Here, too, the gate voltage is increased and then the drain voltage. In the same way, the multiplier can be switched on first and then the AMP002 in the transmitter. The voltages applied and associated drain currents can be found in the appendix in Table A.1.

4.5 Commissioning

After the DC voltages have been successfully applied, the two circuit parts, transmitter and receiver, can be put into operation independently of each other. This allows a specific check of the functionality and the determination of intermediate variables, since, for example, the necessary reflections from two objects add two more unknowns in addition to the transmitted power and the bandwidth of the transmitted signal.

The use of a synthesizer as a signal source for the frequency multiplier of the transmitter allows the generation of signals with defined frequency and output power. A portion of the transmitted power is received by a conical horn antenna mounted on the spectrum analyzer extension module. After power was measured directly from the antenna, the distance between the horn antenna and the on-PCB transmitting antenna was increased to be in the far field with both antennas on the one hand and to get measurement results for a possible real application distance on the other hand. The measurement in the far field is necessary because there the field components are perpendicular

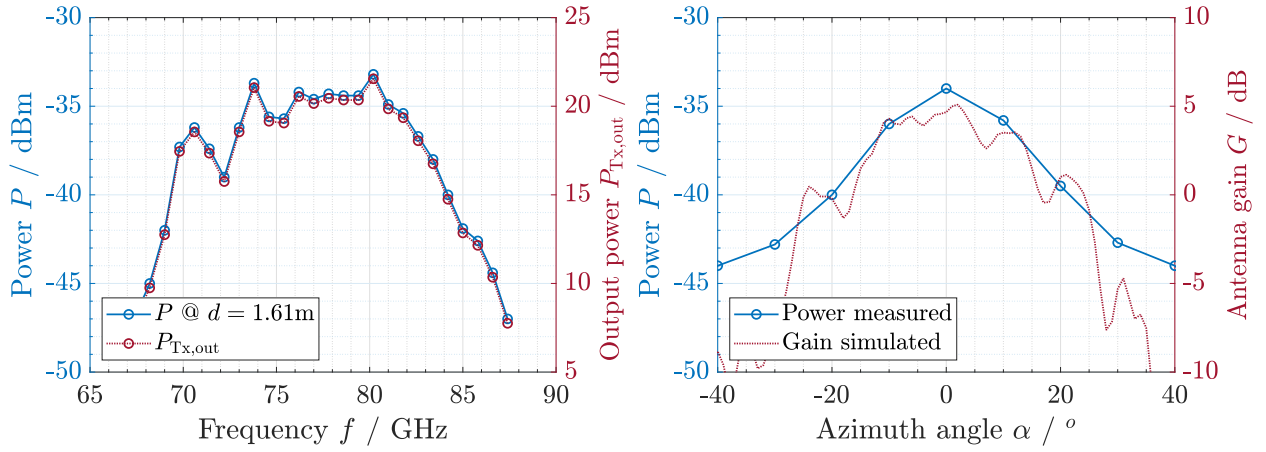

(a) Output power **(b)** Beamwidth determination

Figure 4.8: The measurement results for the variation of the input frequency at constant input power of −5 dBm are shown in a). Figure b) compares the determined main lobe width with the simulation result.

to the beam direction and the entire power flow is directed radially outward. For this reason, the shape of the field distribution in the far field is also independent of the distance. The transition from the near field to the far field is assumed to be $d_{\mathrm{FF}} = 2D^2/\lambda = 2D^2 f/c_0$, where D represents the largest geometrical dimension of the antenna [27, p.32]. Since the resonator of the on-PCB antenna has a width of 8.49 mm and the substrate thickness is 500 µm, a transmit signal with f = 86 GHz results in a distance of approximately 41.5 mm. Due to the slightly increased dimensions of the transmitting antenna, the boundary to the far field for this is at a greater distance.

In the measurement setup, a distance of 1.61 m is used, so d_{FF} does not need to be considered further. If the free space attenuation is calculated using formula 2.22 and including the antenna gain of the receiving horn antenna ($G_{\mathrm{Rx,horn}}$ = 20 dBi), the received power of −34.9 dBm results in a transmitted power of 19.85 dBm. The synthesizer is set to a frequency of 10.125 GHz and an output power of −5 dBm to compensate for losses due to cable attenuation. Both quantities are plotted for this and other frequencies in Fig. 4.8a. The transmitted power back-calculated from the received power corresponds to the expected value at a saturation power of the amplifier of $P_{\mathrm{sat,AMP002}}$ = 20 dBm. However, it also implies that the on-PCB antenna has a gain of 0 dB. However, according to the simulation, the expected gain was higher by about 4 dB. This difference in the power budget consideration may have several causes. On the one hand, the output power of the frequency multiplier may be lower than expected so that the amplifier does not yet go into saturation. Likewise, it is possible that the placed amplifier has a smaller gain than simulated or is not quite at its operating point yet. Similarly, the deviation of the fabrication dimensions compared to the designed and simulated dimensions may affect the gain of the on-PCB horn antenna. There is also some sensitivity of the antenna to its orientation with respect to the receiving antenna. The bandwidth can also be read from Fig.4.8a, which is 13.6 GHz if the narrow dip at 72 GHz is left out.

An increase in input power shows that the output power of the transmitter saturates for an input

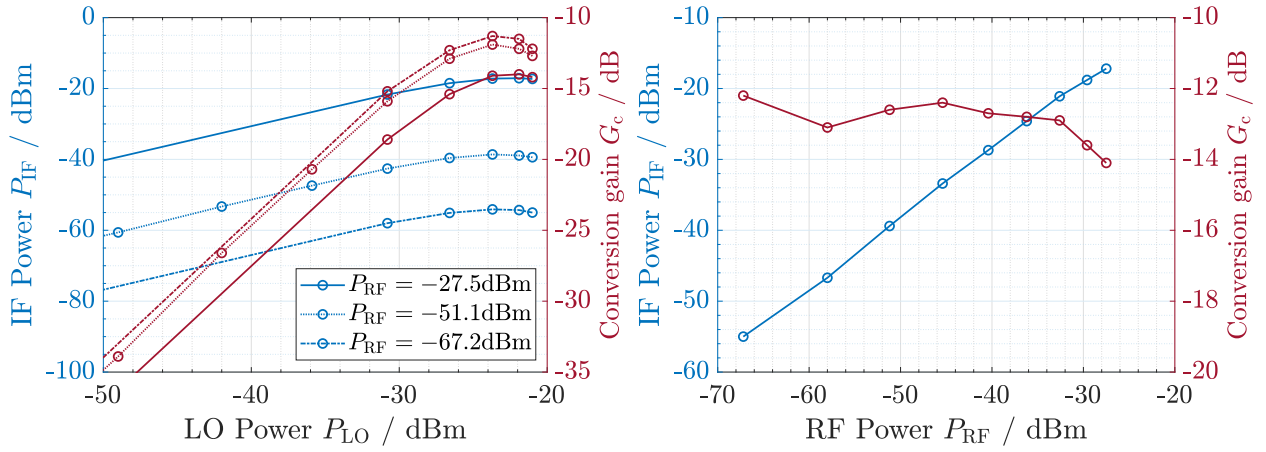

(a) Variation of LO power

(b) Variation of RF power

Figure 4.9: Results of the IF power measurement with variation of a) LO and b) RF power. In addition, the calculated conversion gain is plotted over the same quantities.

power of $P_{Tx,in} = -6$ dBm. If the receiver is rotated stepwise, the mainlobe width can be estimated from the received power. This decreases by 3 dB for an azimuth angle of about ±15°, corresponding to a half-power beamwidth of 30°. The good agreement of these simplified measurements compared to the course of the simulated antenna gain can be seen in Fig. 4.8b. The angle thus represents a tradeoff between selectivity and insensitivity to slight variations in target detection. The vertical angle is significantly larger and should therefore be constrained by absorbers in the housing, as planned. Closing the case including the front cover results in degradation of the received power by 1 dB with still holding values of $P_{Tx,in} = -6$ dBm, $f_{Tx,in} = 10.125$ GHz and $R = 1.61$ m. All in all, however, it can be stated that transmitter works as desired.

Verification of the receiver can be done in a similar way. Here, the received signal was not generated by the transmitter and two reflection objects, but by two horn antennas transmitting with different power. The LO input signal is again provided by a synthesizer. In order to be able to perform a power sweep, a variable attenuator is used in the chain, therefore the setup is similar to that of the pre-measurement (see subchapter 3.4.3). The RF signal is also generated by a chain consisting of the multiplier, the attenuator and the horn antenna. The input signal for this frequency multiplier is provided by a dielectric resonator oscillator with constant frequency. The transmit frequency is thus 73.4366 GHz.

This structure results in three control variables. On the one hand, the LO frequency can be varied, thus determining the broadband characteristics of the output, and on the other hand, the two powers can be attenuated. The former measurement results in a maximum IF frequency of 200 MHz at which the output power still shows no significant deviations at constant input powers. This also agrees with the measurement results. More interesting is the measurement of the LO power variation in particular. This provides information about how high the power of the strong signal must be in order to achieve a desired conversion gain and thus a certain output power. The conversion gain can be approximated by the measured IF power at the output and the calculated

RF power at the input of the mixer. As for the transmitter, the free space path loss, the two antenna gains for the transmitting horn and the receiving on-PCB antenna, can be used to calculate the power before the AMP101 amplifier. The distance between the transmitting and receiving antennas of the test setup is 25 cm. For a frequency of 73.4 GHz, the free space path loss including the antenna gains adds up to 33.71 dB. The maximum power of the RF frequency multiplier in the test setup is 6.2 dBm. Subtracting the attenuation just calculated results in a power of −27.5 dBm at the input of the amplifier. Since this is not yet in saturation at least for the RF signal, its gain can be used to determine the output power and thus the RF input power of the mixer. Applying the same equations to the LO, the graphs in Fig. 4.9a can be computed. It can be seen that the conversion gain compresses much earlier than in the simulation. This can have various reasons. One of them is the uncertain power at the input of the mixer, since this cannot be determined more precisely, seen from the formulas. Likewise, the mixer may not yet be at its correct operating point. For the variation of the RF power, an almost constant conversion gain for a LO input power of −21 dBm before the amplifier is obtained. This expresses the linearity of the mixer with respect to the RF signal. Thus, it can again be stated that the receiver also functions according to expectations.

5 Conclusion and outlook

In this work a frontend for a radar system was designed. It is part of the MIRADOR project, whose goal is to demonstrate the applicability of a self-mixing radar principle. The frequency range for the designed system extends from approximately 70 GHz to 83 GHz and with its bandwidth of more than 13 GHz thus provides a range resolution of less than 11.5 mm. The individual components of the radar system, which originate from the ELiPSe project, were examined simulatively for their characteristic values.

To design a self-mixing receiver, the mixer has to form the intermediate frequency from two signals. They are both received by the on-PCB antenna, originate from two reflection objects and represent the LO and RF signal. To design a self-mixing receiver, the mixer has to form the intermediate frequency from two signals. They are both received by the on-PCB antenna, originate from two reflection objects and represent the LO and RF signal. For this purpose a self-mixing configuration was investigated, which, by applying both received signals to the RF port of the mixer, exploits the nonlinear I_D/V_{DS} relationship for mixing. To minimize conversion losses, a transconductance mixer was formed by biasing the transistor drains. This improves the conversion gain by more than 12 dB, which allows both the detection of weaker signals and the exploitation of a lower reflectance as the LO signal.

The implementation and validation of the simulative considered overall system was performed on a RF-PCB, which allows the implementation of two horn antennas, one for transmission and one for receiving, by using a thicker high frequency laminate. The associated layout was designed and then assembled. The MMIC, which were attached with conductive adhesive, were connected to each other using wedge bonds. The connection to the DC and RF traces was done in the same way. Individual structures were subsequently simulated or measured again in order to better assess the influence of deviations caused by PCB production. The subsequent commissioning confirmed that these existing deviations only play a minor role.

In the future, the systems designed by other students for signal evaluation and chirp generation should be combined with the frontend. In addition, a controlled power supply should be placed in the housing, which supplies all circuit boards and, above all, carries out the ramp up and down of the individual MMIC supply voltages in a controlled manner. Since only the commissioning of the frontend has been carried out so far, it is necessary to determine the exact characteristics and further compare them with the simulation. This can also include a measurement of the two identical antennas in order to derive possible measures for limiting the elevation angle from the antenna diagram, for example by means of absorbers in the housing. Likewise, efforts should be made to reduce their coupling, as these led to impairments during commissioning.

Bibliography

[1] *71 GHz to 86 GHz, E-Band Low Noise Amplifier: HMC8325: data sheet*. https://www.analog.com/media/en/technical-documentation/data-sheets/HMC8325.pdf

[2] Vishay Intertechnology, Inc. (Hrsg.): *AEC-Q200 Qualified High Frequency 70 GHz Thin Film Chip Resistor: CH: data sheet*. https://www.vishay.com/docs/53014/ch.pdf

[3] *AWR1843AOP Single-chip 77- and 79-GHz FMCW radar sensor: Data sheet*. https://www.ti.com/lit/ds/symlink/awr1843aop.pdf?ts=1633256147652&ref_url=https%253A%252F%252Fwww.ti.com%252Fproduct%252FAWR1843AOP. Version: A

[4] *Board Design Guidelines Solution Center: Chapter: Minimization Parasitic Inductances*. https://www.intel.com/content/www/us/en/programmable/support/support-resources/support-centers/board-design-guidelines.html, Abruf: 12.09.2021

[5] *Ceramic Capacitors FAQ*. https://www.murata.com/en-eu/support/faqs/capacitor/ceramiccapacitor/char/0005, Abruf: 12.09.2021

[6] *Chip Multilayer Ceramic Capacitors for General Purpose: GRM155C71A225KE11#: data sheet*. https://www.murata.com/en-eu/products/productdetail?partno=GRM155C71A225KE11%23, Abruf: 26.09.2021

[7] *CST Microwave Studio: Workflow & Solver Overview*

[8] *Did you know? The effects of mounting in high frequency applications: Assesing the performance of CH resistors*. https://www.vishay.com/docs/48566/_ms10541367-2102-did_you_know-ch.pdf

[9] *EMC and System-ESD Design Guidelines for Board Layout: AP24026*. https://www.infineon.com/dgdl/Infineon-AP2402635_General_PCB-AN-v03_05-EN.pdf?fileId=5546d46261ff5777016229f8523036f1. Version: V3.5

[10] Umicore Galvanotechnik GmbH (Hrsg.): *EPIG-PROZESS: ELECTROLESS PALLADIUM AND IMMERSION GOLD PLATING*. https://ep.umicore.com/storage/ep/produktblatt-umicore-epig-de-screen-20190417.pdf

[11] *Frequency Response of Thin Film Chip Resistors: Technical Note*. https://www.vishay.com/docs/60107/freqresp.pdf

[12] *The HF Resistor Application Guide*. https://www.ieee.li/pdf/essay/hf_resistor_application_guide.pdf

[13] *HMC-ALH508: GaAs HEMT low noise amplifier, 71 - 86 GHz: data sheet*. https://www.analog.com/media/en/technical-documentation/data-sheets/hmc-alh508.pdf. Version: v02.0209

[14] *HMC-ALH509: GaAs HEMT low noise amplifier, 71 - 86 GHz: data sheet*. https://www.analog.com/media/en/technical-documentation/data-sheets/hmc-alh509.pdf. Version: v05.0713

[15] *HMC-AUH320: GaAs HEMT MMIC medium power amplifier, 71 - 86 GHz: data sheet*. https://www.analog.com/media/en/technical-documentation/data-sheets/hmc-auh320.pdf. Version: v04.0412

[16] *HMC1110: GaAs MMIC X6 ACTIVE FREQUENCY MULTIPLIER, 71 - 86 GHz: data sheet*. https://www.analog.com/media/en/technical-documentation/data-sheets/HMC1110.pdf. Version: v00.0615

[17] *IWR1443 Single-Chip 76- to 81-GHz mmWave Sensor: Data sheet*. https://www.ti.com/lit/ds/symlink/iwr1443.pdf?ts=1633207575686&ref_url=https%253A%252F%252Fwww.ti.com%252Fproduct%252FIWR1443. Version: C

[18] *M9614A and M9615A PXIe 5-Channel Precision Source/Measure Units: data sheet*. https://www.keysight.com/de/de/assets/3120-1310/data-sheets/M9614-and-M9615A-PXIe-5-Channel-Precision-Source-Measure-Units.pdf

[19] *Miniature surface-mount bias-tee: BTL-0012SMG: data sheet*. https://www.markimicrowave.com/Assets/datasheets/BTL-0012SMG.pdf#v=051021

[20] *Oberflächenübersicht*. http://contag.de/uploads/pi_ti/oberflaechen_g.pdf

[21] *PXI-4130 specifications: data sheet*. https://www.ni.com/pdf/manuals/374746e.pdf

[22] *PXIe-4144 specifications: data sheet*. https://www.ni.com/pdf/manuals/373887e.pdf

[23] *Shielded Power Inductors – LPS6225: Document 554-1: data sheet*. https://www.coilcraft.com/getmedia/987bc36f-43aa-4b8a-bd65-45af615705fa/lps6225.pdf

[24] CONTAG AG (Hrsg.): *Technologie-Info*. http://www.contag.de/uploads/techniks/contag_materialien.pdf

[25] *High-Tg circuit boards (HTg)*. https://www.multi-circuit-boards.eu/en/products/printed-circuit-boards/high-tg-pcb.html. Version: 18.09.2021

[26] Beck, Donald J. ; Perez, Albert C.: Wire Bond Technology: The Great Debate: Ball vs. Wedge. In: *Advanced Packaging* 16 (2007), Nr. 2, S. 28–30

[27] Belous, Anatoly: *Handbook of Microwave and Radar Engineering*. 6330 Cham, Switzerland : Springer Nature Switzerland AG, 2021. – ISBN 978–3–030–58698–0

[28] Cassivi, Y. ; Perregrini, L. ; Arcioni, P. ; Bressan, M. ; Wu, K. ; Conciauro, G.: Dispersion Characteristics of Substrate Integrated Rectangular Waveguide. In: *IEEE Microwave and Wireless Components Letters* 12 (2002), Nr. 9, S. 333–335. http://dx.doi.org/10.1109/LMWC.2002.803188. – DOI 10.1109/LMWC.2002.803188. – ISSN 1531–1309

[29] Chartier, Sébastien: *Microwave Analog Front-End Design II: FMCW Radar: Lecture notes*

[30] Chaturvedi, Prakash K.: *Microwave, radar & RF engineering: With laboratory manual*. Singapore : Springer, 2018. – ISBN 978–981–10–7965–8

[31] Chen, Zhi N. (Hrsg.) ; Liu, Duixian (Hrsg.) ; Nakano, Hisamatsu (Hrsg.) ; Qing, Xianming (Hrsg.) ; Zwick, Thomas (Hrsg.): *Handbook of Antenna Technologies*. Singapore : Springer Nature, 2016. http://dx.doi.org/10.1007/978-981-4560-44-3. http://dx.doi.org/10.1007/978-981-4560-44-3. – ISBN 978–981–4560–44–3

[32] Coonrod, John: The Dilemma: Soldermask for High-Frequency PCBs. In: *The PCB Design Magazine* 6 (2016), Nr. 5, 68–70. http://iconnect007.uberflip.com/i/691539-pcbd-june2016/67?

[33] Djerafi, Tarek ; Doghri, Ali ; Wu, Ke: Substrate Integrated Waveguide Antennas. In: Chen, Zhi N. (Hrsg.) ; Liu, Duixian (Hrsg.) ; Nakano, Hisamatsu (Hrsg.) ; Qing, Xianming (Hrsg.) ; Zwick, Thomas (Hrsg.): *Handbook of Antenna Technologies*. Singapore : Springer Nature, 2016. – ISBN 978–981–4560–44–3, S. 1585–1655

[34] Emilsson, Erik P.: *Radar Transparency and Paint Compatibility: A Study of Automobile Bumper and Bumper-Skin Complex Permittivities for 77GHz Microwaves*. Gothenburg, Sweden, Chalmers University of Technology, Diplomarbeit, 2017. https://publications.lib.chalmers.se/records/fulltext/254360/254360.pdf

[35] Esquius-Morote, Marc ; Fuchs, Benjamin ; Zurcher, Jean-Francois ; Mosig, Juan R.: A Printed Transition for Matching Improvement of SIW Horn Antennas. In: *IEEE Transactions on Antennas and Propagation* 61 (2013), Nr. 4, S. 1923–1930. http://dx.doi.org/10.1109/TAP.2012.2231923. – DOI 10.1109/TAP.2012.2231923. – ISSN 0018–926X

[36] Gerhardes, F. ; Leuchs, Sven ; Arpe, Oliver: *E-Band Based Car Radar Emblem Measurements: Application note*. https://dl.cdn-anritsu.com/en-us/test-measurement/files/Application-Notes/Application-Note/11410-01152A.pdf

[37] Hesselbarth, Jan: *Antennas - Hochfrequenztechnik II: Lecture notes*

[38] Hesselbarth, Jan: *Radio Frequency Technology: (Hochfrequenztechnik 3): Skript zur Vorlesung*

[39] Hoffmann-Eifert, Susanne ; Richter, Dieter ; Trolier-Mc Kinstry, Susan: Dielectric, Ferroelectric, and Optical Properties. Version: 2012. https://application.wiley-vch.de/books/sample/3527409270_c01.pdf. In: Waser, Rainer (Hrsg.): *Nanoelectronics and information technology*. Weinheim : Wiley-VCH, 2012. – ISBN 9783527409273, 33–62

[40] Hülsmeyer, Christian: *Verfahren, um entfernte metallische Gegenstände mittels elektrischer Wellen einem Beobachter zu melden*. https://www.dpma.de/docs/postergalerieneu/patentschriften/013radar-christianhuelsmeyer.pdf. Version: 1905

[41] IPC International, Inc.: *IPC-6012: Qualification and Performance Specification for Rigid Printed Boards*. B. 2004

[42] Jorgesen, Doug: *What is the deal with IP2 in mixers?* https://www.markimicrowave.com/blog/what-is-the-deal-with-ip2-in-mixers/. Version: 2014, Abruf: 26.09.2021

[43] Kallfass, Ingmar: *Microwave Analog Frontend Design: Lecture notes*

[44] Kallfass, Ingmar: *Microwave Engineering: Lecture notes*

[45] Kallfass, Ingmar ; Grötsch, Christopher ; Schoch, Benjamin: *Method of ascertaining at least one physical parameter of a system by exploiting the reflection from a reference object*. 2021

[46] Kingsley, Nickolas ; Guerci, J. R.: *Radar RF Circuit Design*. Norwood, MA 02062 : Artech House, 2016. – ISBN 978–1–60807–970–4

[47] Lee, Kai F. ; Yang, Shing Lung S. ; Kishk, Ahmed: The versatile U-slot patch antenna. In: *3rd European Conference on Antennas and Propagation* (2009), 3312–3314. https://ieeexplore.ieee.org/document/5068307

[48] Liebl, Detlev: *Measuring with Modern Spectrum Analyzers: Educational Note*. https://cdn.rohde-schwarz.com/pws/dl_downloads/dl_application/application_notes/1ma201_1/1MA201_9e_spectrum_analyzers_meas.pdf

[49] Niknejad, Ali M.: *Mixer Noise: Advanced IC's for Comm*. http://rfic.eecs.berkeley.edu/ee242/pdf/Module_5_2_MixerNoise.pdf

[50] Perry, Chris: *ENEPIG BENEFITS FOR GOLD WIRE BONDING*. https://blog.epectec.com/enepig-benefits-for-gold-wire-bonding. Version: 2018, Abruf: 12.09.2021

[51] Pozar, David M.: *Microwave engineering*. 4. ed. Hoboken, NJ : Wiley, 2012. – ISBN 9780470631553

[52] Rao, Sandeep: *Introduction to mmwave Sensing: FMCW Radars*. https://training.ti.com/sites/default/files/docs/mmwaveSensing-FMCW-offlineviewing_4.pdf

[53] Rayas-Sanchez, Jose E. ; Gutierrez-Ayala, Vladimir: A general EM-based design procedure for single-layer substrate integrated waveguide interconnects with microstrip transitions. http://dx.doi.org/10.1109/MWSYM.2008.4632999. In: *2008 IEEE MTT-S International Microwave Symposium Digest 2008*. – DOI 10.1109/MWSYM.2008.4632999, S. 983–986

[54] Rogers Corporation ; Advanced Connectivity Solutions (Hrsg.): *RO3000® Series Circuit Materials: RO3003™, RO3006™, RO3010™ and RO3035™ High Frequency Laminates*. https://rogerscorp.com/-/media/project/rogerscorp/documents/advanced-electronics-solutions/english/data-sheets/ro3000-laminate-data-sheet-ro3003----ro3006----ro3010----ro3035.pdf. Version: 2019, Abruf: 05.09.2021

[55] Schoch, Benjamin ; Tessmann, Axel ; Wagner, Sandrine ; Kallfass, Ingmar: E-band Balanced Broadband Driver Amplifier MMIC with 1.8THz Gain-Bandwidth Product. Version: 2020. https://ieeexplore.ieee.org/document/9080222. In: *Proceedings of the 2020 German Microwave Conference*. 2020. – ISBN 978–3–9820397–1–8, 9–12

[56] Soc, Ivan ; Nash, Eamon ; Analog Devices Inc. (Hrsg.): *Wideband Bias Tee Design Using 0402, SMD Components: AN-2061: Application Note*. https://www.analog.com/media/en/technical-documentation/app-notes/an-2061.pdf

[57] Wadell, Brian C.: *Transmission Line Design Handbook*. Boston : Artech House, 1991. – ISBN 0890064369

[58] Welp, Benedikt ; Hansen, Steffen ; Briese, Gunnar ; Küppers, Simon ; Thomas, Sven ;

Bredendiek, Christian ; Pohl, Nils: Versatile Dual-Receiver 94-GHz FMCW Radar System With High Output Power and 26-GHz Tuning Range for High Distance Applications. In: *IEEE Transactions on Microwave Theory and Techniques* 68 (2020), Nr. 3, 1195–1211. http://dx.doi.org/10.1109/TMTT.2019.2955127. – DOI 10.1109/TMTT.2019.2955127. – ISSN 0018–9480

[59] Winner, Hermann ; Hakuli, Stephan ; Lotz, Felix ; Singer, Christina: *Handbuch Fahrerassistenzsysteme: Grundlagen, Komponenten und Systeme für aktive Sicherheit und Komfort*. 3. Wiesbaden : Springer Fachmedien Wiesbaden, 2015. http://dx.doi.org/10.1007/978-3-658-05734-3. http://dx.doi.org/10.1007/978-3-658-05734-3. – ISBN 978–3–658–05733–6

[60] Wolff, Christian: *radartutorial.eu: Grundlagen der Radartechnik*. radartutorial.eu, Abruf: 05.10.2021

[61] Xiao, Yang ; Norouzian, Fatemeh ; Marchetti, Emidio ; Cassidy, Scott ; Hoare, Edward ; Cherniakov, Mikhail ; Gashinova, Marina: Transmissivity Through Automotive Bumpers at mm-wave and Low-THz Frequencies. In: *2019 20th International Radar Symposium (IRS)*, IEEE, 26.06.2019 - 28.06.2019. – ISBN 978–3–7369–9860–5

[62] Xu, Feng ; Wu, Ke: Guided-wave and leakage characteristics of substrate integrated waveguide. In: *IEEE Transactions on Microwave Theory and Techniques* 53 (2005), Nr. 1, S. 66–73. http://dx.doi.org/10.1109/TMTT.2004.839303. – DOI 10.1109/TMTT.2004.839303. – ISSN 0018–9480

[63] Zech, C. ; Hülsmann, A. ; Schlechtweg, M. ; Reinold, Steffen ; Giers, Christof ; Kleiner, Bernhard ; Georgi, L. ; Kahle, R. ; Becker, K.-F. ; Ambacher, O.: A compact W-band LFMCW radar module with high accuracy and integrated signal processing. In: *45th European Microwave Conference, EuMC 2015. Proceedings : 7-10 September 2015, Paris, France* (2015), 554–557. http://publica.fraunhofer.de/dokumente/N-366330.html

Appendix

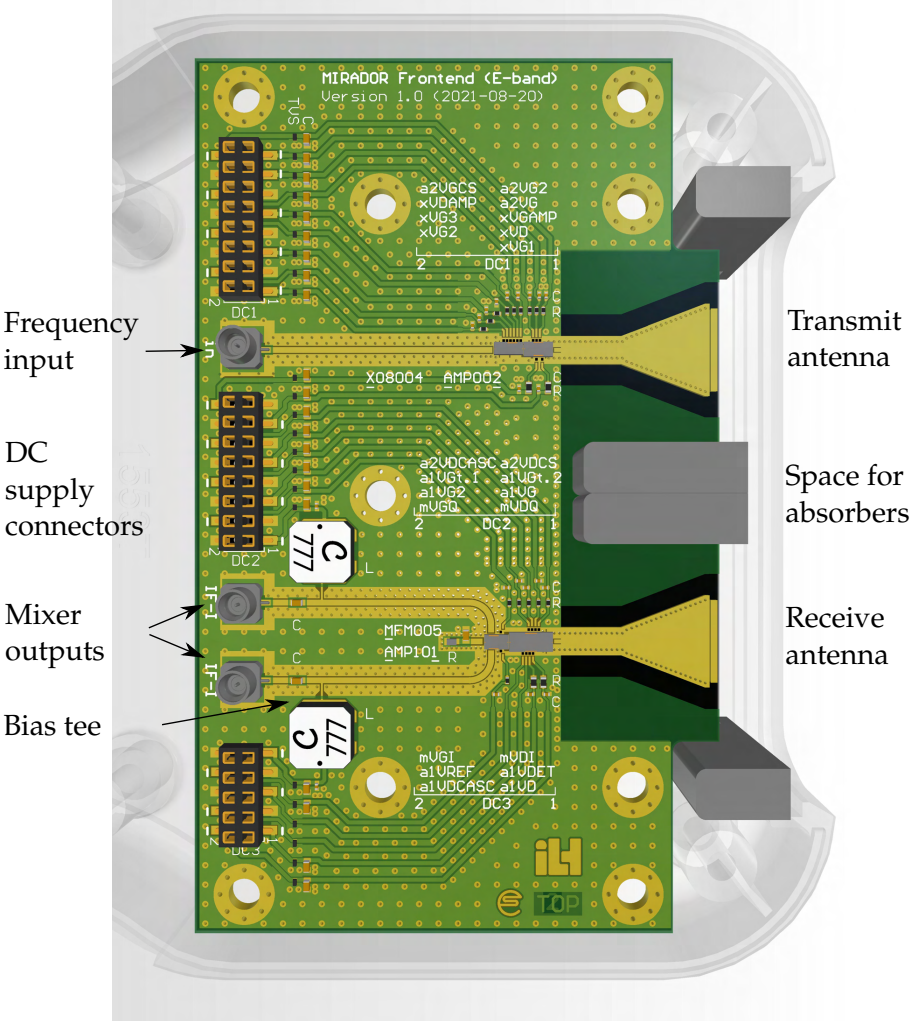

Figure A.1: Visualization of the designed frontend in its case.

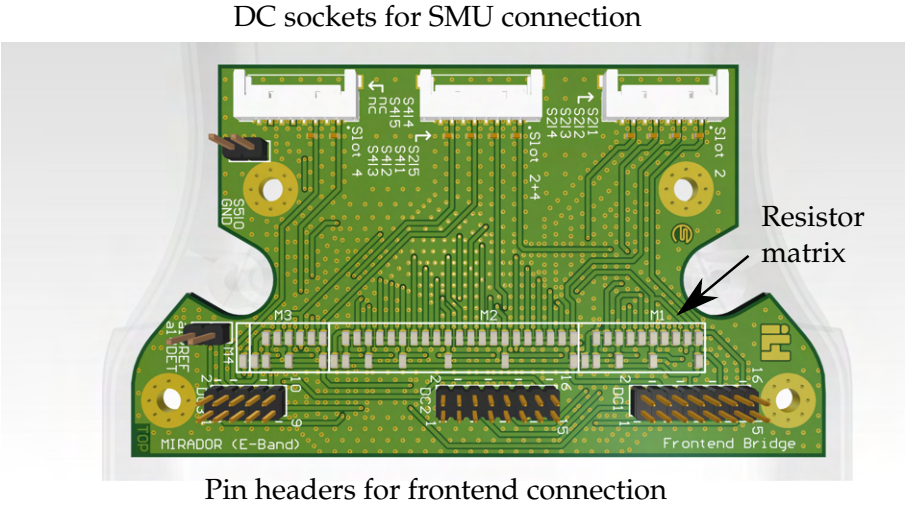

Figure A.2: Visualization of the designed bridge PCB, which allows the connection of individual DC voltages through the resistor matrix.

Table A.1: Set supply voltages during commissioning compared to expected values. In addition, the current and the drain current density are listed.

Component	Voltage	Exp. voltage V	Appl. Voltage V	Current / mA	C. density / mA/mm
X08004	V_{GG1}	−0.3	−0.2	−0.02	
	V_{GG2}	−0.25	−0.2	−0.01	
	V_{DD}	1.51	1.1	3.5	
	V_{GG3}	−0.3	−0.2	−0.006	
	$V_{AMP,VG}$	0.15	0.15	−0.02	
	$V_{AMP,VDS}$	1.82	1.25	56.5	314
AMP002	V_G	0.1	0.15	−0.08	
	V_{G2}	0.9	1.15	0.004	
	$V_{D,CASC}$	2.96	2.4	133.4	370
	$V_{G,CS}$	0.15	0.1	−0.24	
	$V_{D,CS}$	1.79	1.6	245.4	279
AMP101	V_{G2}	1.2	1	−0.07	
	$V_{D,CASC}$	2.71	2.6	138.5	289
	$V_{G,tune1}$	0.2	0.24	−0.009	
	$V_{G,tune2}$	0.2	0.21	−0.015	
	$V_{G,CS}$	0.1	0.1	0.001	
	$V_{D,CS}$	1.7	1.5	192.3	267
MFM005	$V_{G,I}$	−0.19 V	−0.01	−0.001	
	$V_{G,Q}$	−0.19	0*	–	
	$V_{D,I}$	0.94	0.95	3.8	47.5
	$V_{D,Q}$	0.94	0*	–	

* After second DC ramp up the gate current is too high. Therefore voltages set to 0 V.